University of California, Merced

Ph.D. Dissertation

Simulations of flow in partially porous domains with focus on settling and erosion applications

A dissertation submitted in partial fulfillment of the requirements for the degree

Doctor of Philosophy in Mechanical Engineering

by

Mac Panah

August 8, 2017

University of California, Merced

Graduate Division

This is to certify that I have examined a copy of a dissertation by

Mac Panah

and found it satisfactory in all respects, and that any and all revisions required by the examining committee have been made.

Faculty Advisor: _____

François Blanchette

Committee Members: _____

Gerardo C. Diaz

_____

Venkattraman Ayyaswamy

Mechanical Engineering Graduate Studies Chair: _____

Ashlie Martini

_____

Date Signed

Abstract

We simulate flows involving porous media and homogenous fluid using a single-domain finite-difference numerical method. We study numerically the settling of a porous sphere in a density-stratified ambient fluid. Simulations are validated against prior laboratory experiments and compared to two mathematical models. Two main effects cause the particle to slow down as it enters a density gradient: lighter fluid within the particle and entrainment of the density-stratified ambient fluid. The numerical simulations accurately capture the particle retention time. We quantify the delay in settling due to ambient fluid entrainment and lighter internal fluid becoming denser through diffusion as a function of the Reynolds, Péclet, and Darcy numbers, as well as the thickness of the transition layer and the ratio of the density difference between the lower and upper fluid layer to the density difference between the particle and the upper layer. A simple fitting formula is presented to describe the settling time delay as a function of each of those five non-dimensional parameters.

We introduce a new numerical method specially designed for fluid-porous simulations. The porous medium and unimpeded fluid are separated by a sharp interface where a stress jump boundary condition is implemented using a forcing term. The interface is constructed by connecting Lagrangian markers with cubic splines, allowing for any possible porous media geometry. This model is particularly flexible as it can easily account for a mobile interface. We apply our method to simulate erosion and suspension of particles from a fixed particulate deposit. The flux of particles separated from porous media ascribable to a moving fluid is obtained from the computed velocity across the interface, in contrast to more common approaches that assume a flux proportional to the viscous stress at the interface.

CURRICULUM VITAE

Education

Master of Science in **Engineering Physics**, Royal Institute of Technology (Sweden), 2000.

Masters in **Mechanical Engineering**, California State University Northridge (USA), 2010.

Publications

Mac Panah, François Blanchette, Shilpa Khatri (2017) "Simulations of a porous particle settling in a density-stratified ambient fluid". Submitted to the Journal of Physical Review Fluids.

Mac Panah, François Blanchette (2016) "Simulating flow over and through porous media with application to erosion of particulate deposits". Submitted to the Journal of Computers & Fluids.

Mac Panah, François Blanchette (2014) "Simulations of flow focused at the interface of free flowing fluid and porous media". *Proceedings of the 67th Annual Meeting of the APS Division of Fluid Dynamics San Francisco, CA - November 23, 2014 - November 25, 2014.*

Acknowledgements

As I reflect on this amazing journey, I would like to express the highest gratitude, to my advisor, Professor Francois Blanchette for his continuous support and guidance. He has been a great source of inspiration throughout these years providing valuable insight into the field of fluid mechanics and numerical methods.

My special thanks goes to the extended committee members Professor Gerardo Diaz and Professor Venkatt Ayyaswamy for being supportive and helpful beyond expectations. I had the privilege to attend their class in advanced heat transfer and fluid mechanics. I would also like to thank Professor Jian-Qiao Sun and Professor Roummel Marcia for being wonderful instructors in control and numerical methods. This coursework has been an important foundation toward my main objective to become an independent researcher.

My son Abtin, my parents Houshang and Sara and my siblings Babak and Farzaneh have been my greatest source of energy. I will always be grateful for their boundless support and encouragement. Now, I am beaming with pride as I review this great accomplishment, and I would not be in this place without their unprecedented consolation.

I have forged new friendships while residing in Merced. Lora, David and Matthew have been wonderful conversation and adventure partners. Hikes in Yosemite, trips to San Fransisco, playing tennis and white water rafting will be some of the good memories I will always carry with me.

Also important to me, is the hope that this research has contributed to the greater good of all humanity, to the environment, and to the growth of progression in general. This process, I view as a privilege, to be one minor participant in such important work. This has been a very humbling experience for me. It is my hope that this research will inspire the future generation to be more alert and mindful of our beautiful planet and its resources.

Contents

List of Figures

List of Tables

Chapter 1

Introduction

In fluid dynamics, we study the science of fluid motion. A fluid is a substance that undergoes continuous deformation under applied shear stress. Liquids, gases and plasmas are considered to be different categories of fluid [2]. In contrast to a solid, a fluid conforms to the shape of its container. Fluid dynamics is an active field of research with a wide range of applications in geophysics, meteorology, astrophysics, biology and many aspects of engineering [3]. The study of fluid mechanics dates back to ancient Greece, where the famous Archimedes' principle was discovered. Scientific development accelerated in the 19th century with the introduction of governing equations describing different type of flows. The Navier-Stokes equations describe the motion of viscous fluid where the pressure, density, temperature and velocity are related through the laws of conservation of mass, momentum and energy. In their derivation, the fluid is treated as a continuous medium where macroscopic properties are continuous and well defined at infinitesimal volume elements. The fluid element is assumed to be small with respect to the length scale of the system but many times larger than the size of the molecules [4].

Fluid flow through porous medium is another branch of fluid mechanics that is commonly studied. Many substances in our environment, man-made or natural, are considered porous. Sand, aquifers, zeolites, biological tissues and industrial filters are a few examples of common porous material. A porous medium is a solid matrix structure with interconnected pores. The main characteristics of porous media are porosity and permeability, both important parameters in geological applications. Porosity is defined as the volume fraction of void space in a material that may contain any fluid [5]. The pore geometry and its interconnectedness has a profound effect on permeability, a measure of how well fluid flows through the porous material. In most situations, the solid matrix of the porous media is rigid but the frame can be deformed if the flow is strong. In recent years, scientific interest in porous solids has grown because they can interact with other substances not only at the surface but within the porous domain of the material providing a much larger surface exposure. This quality is highly desired for materials used in microelectronics and medical diagnosis because of their superior catalysts or aborbent abilities [6].

Fluid interaction with porous media is a common phenomena in geosciences, petroleum engineering, bio-remediation, construction engineering, biology, biophysics and material sciences. More specifically, porous flow can be found in inkjet printing technologies, nuclear waste disposal, ground water flows, settling of porous marine organisms and erosion of sandy deposits [7]. Developing the technologies associated with these fields, requires a deeper study of fluid motion in porous media. Early investigations revealed that the flow rate through porous media is proportional to the pressure gradient in the flow direction and intrinsic permeability of the medium. This model (Darcy's law) is

a linear differential equation and is derived under the assumption of a continuum approach considering volume elements that are large compared with the average pore volume [5]. The linear nature of Darcy's law is valid only when the fluid velocity is sufficiently small. For higher fluid velocities, Darcy's law is extended with a Laplacian including a fluid-to-fluid drag and a quadratic term to compensate for the increasing form drag [8].

One example of a system where fluid flow in and around a porous region is determinant, is that of marine snow. Marine organisms settling into the deep ocean are often highly porous and play an important role in the carbon cycle. The carbon cycle along with water and nitrogen are key factors in sustaining life on earth. Carbon can be found in biological organisms, plants, minerals, etc and is continuously recycled between biosphere, geosphere, pedosphere, atmosphere and hydrosphere [9]. Oceans contain the greatest quantity of actively cycled carbon on earth. Organic matter settling in the ocean, eventually breaks down into its simplest inorganic forms such as carbon dioxide and water; a process called remineralization [10]. The depth at which this process occurs is referred to as remineralization depth and it is dependent on the settling speed and decay rate of the particles. Factors such as temperature, oxygen concentration, stratification and particle composition can all affect this balance. Models show that a modest change in the remineralization depth can have substantial impact on atmospheric carbon dioxide concentrations [10].

In coastal waters, micro organisms such as phytoplankton aggregate in thin layers in the twilight zone [11]. The thin layer formation can be triggered by biological mechanisms such as enhanced localized growth, directed swimming or interaction between swimming and shear [12, 13]. Physical parameters like density stratification in the ocean can also lead to aggregation in a thin layer. Theoretical and experimental studies validate diminished settling velocities at sharp density gradients due to entrainment and particle porosity. The drag associated with the settling object entrains lighter fluid from upper layers resulting in a temporary slow down [14, 15]. This mechanism is referred to as entrainment induced retention. In addition, if the particle is porous, it is saturated with lighter fluid from the upper layer with lower salt concentration. The particle remains buoyant until the stratifying agent (heat or salt) diffuses inside [1,16]. The diffusion induced retention is in most cases the dominant cause of settling delay. In chapter 3, we study the settling of a porous particle in density stratified ambient and quantify the retention due to entrainment and diffusion for various parameters.

In recent years, numerical methods have been employed to solve complex mathematical problems. Scientist and engineers can study systems that can not be solved analytically. Numerical algorithms are developed to obtain approximate solutions to well posed partial differential equations. The major problem with numerical solutions is the accumulation of error when the problem is advanced in time. Discretization and roundoff errors are the major components of the numerical error. Discretization is equivalent with transferring continuous variables and equations into discrete grid points. If the numerical method is stable, the error converges to zero with reduced mesh size. A necessary stability criteria for certain partial differential equations is the CFL condition (Courant-Friedrichs-Lewy), restricting the temporal time step to be a function of spatial resolution [17].

In fluid applications, the Navier-Stokes equations are often solved numerically on fixed (Eulerian) grid. The most common numerical methods are finite differences (FD), finite volume method (FVM) and finite element method (FEM). In the finite volume method, the divergence theorem is used to convert the volume integrals into surface integrals. The surface integrals are evaluated as a flux at surfaces of each finite volume cell. The conservation laws ensure that the flux in and out from each cell is conserved [18]. In finite element methods, a large problem is partitioned into smaller and simpler elements. The equations that model these finite elements are put together into a large system of algebraic equations and solved using variational methods [17]. In finite differences, we approximate the derivatives with ratios of discrete differences. Finite differences have the advantage

of being simple and efficient but they can not handle irregular computational domains. Finite volume and element methods are more complicated to implement but can be employed for any arbitrary geometry.

Simulation of flows including fluid and solid or different phases of the same substance is sometimes necessary. In oil and gas applications, water, oil and gas flow together as a mixture. Mud slides and gravity currents contain both water and sand. Other applications are sediment transportation in a river or blood flow in an injured vessel. A common numerical approach for these type of problems is to separate the phases through a mobile interface. The interface is constructed using Lagrangian markers connected with cubic splines. The subdomains on each side of the interface is simulated with different governing equations or parameters on a Eulerian grid. The fluid velocity can be coupled to a moving interface through different methods. The volume of fluid (VOF) method computes the concentration of different phases of fluid in a grid cell and accommodates for the evolving shape of the interface. In chapter 4, we present a novel method to allow for accurate description of the flow near a fluid-porous medium interface [19]. This method is used to quantify erosion in flow over sandy deposits.

Water flowing over sandy deposits and soil is another example of fluid and porous media interaction. The sediment can be transported by water as bed load or as suspended particles are advected by the flow [20]. Sediment transportation is important in many fields such as environmental engineering, civil engineering, geology and geomorphology. Environmental scientists use sediment transport models to determine rate of erosion or deposition and the time and distance over which sediments travel. Although erosion is a natural phenomena, excessive erosion induced by human activities is considered one of the most significant environmental problems worldwide [21]. The loss of nutrient rich upper soil decreases the agricultural productivity leading in extreme cases to desertification. Sedimentation of waterways and damages to roads and houses are other examples of costly incidents caused by erosion.

Many different empirical models have been developed to quantify entrainment from a river bed. Einstein (son of the famous physicist) was one of the pioneers in this field. He introduced a model where the dimensionless bed-load transport rate is related to the dimensionless bed shear stress. The shear stress is associated with the skin friction between fluid and sand. This model is only applicable to uniform non-cohesive material [22]. The Garcia-Parker model is a more generalized empirical model yielding reasonable estimates of sediment entrainment for beds covered with non-uniform material. In this model, the sediment entrainment rate is proportional to the dimensionless shear velocity. For true suspension, the dimensionless entrainment rate is not supposed to exceed 0.3 for the mixture of sand and water [23]. In chapter 5, we present a non-empirical erosion model for estimation of sediment entrainment into suspension at the fluid-sand interface. Our model is applicable to both uniform and non-uniform non-cohesive porous material.

This dissertation is organized as follows. In chapter 2, we introduce the governing equations for fluid, porous media and concentration transport in dimensional form. Chapter 3 describes the settling of a porous sphere in a density stratified ambient. The delay in settling due to entrainment and diffusion is modeled with fitted parameters. In chapter 4, we present a new numerical method for porous-fluid applications where the fluid and porous subdomains are separated by a Lagrangian interface. We solve the Navier-Stokes and Brinkman equations on a staggered MAC grid and apply the stress jump boundary condition between fluid and porous media through a forcing term at the interface. In chapter 5, we apply our numerical method on two erosion applications; jet flow and hill flow. We determine the erosion rate using the velocity at the interface and compare our results with traditional empirical methods. Lastly, we conclude this dissertation in chapter 7.

Chapter 2

Governing equations for fluid flow and flow through a porous medium

2.1 Equations of fluid motion

In scientific applications, fluid motion is broadly described by the Navier-Stokes equations, named after the mathematicians Claude-Louis Navier and George Gabriel Stokes. These equations are expressed in dimensional form as

$$\nabla \cdot \vec{u} = 0 \tag{2.1}$$

$$\rho\Big(\frac{\partial \vec{u}}{\partial t} + \vec{u} \cdot \nabla \vec{u}\Big) = \nabla \cdot \bar{\bar{T}}_f + \vec{f}, \tag{2.2}$$

where $\bar{\bar{T}}_f = -p\bar{\bar{I}} + \mu(\nabla \vec{u} + (\nabla \vec{u})^T)$ is the Cauchy stress tensor, $\vec{u}$ is the fluid velocity vector, ρ is the fluid density, p is the pressure field, μ is the fluid viscosity, and $\vec{f}$ is a generic body force. The Cauchy stress tensor assumes the stress to be a Galilean invariant (depending only on the velocity gradient) and that the fluid is isotropic [24].

Equation 2.1 reflects conversation of mass for an incompressible fluid and equation 2.2 originates from conservation of momentum. The momentum balance equation is derived from applying Newton's second law to a volume fluid element. The two terms in the left hand side describe the local and convective acceleration of the fluid and the right hand side contains the pressure, viscous and body forces applied to the fluid.

The Navier-Stokes equations are nonlinear partial differential equations and can not be solved analytically in most applications. In cases where the fluid is highly viscous, the left hand side of equation 2.2 can be omitted and the Navier-Stokes equations are simplified to Stokes flow. The Stokes equations are linear and can be solved analytically by the stream function method or the Stokeslet (Green's function) method. A useful result is the flow around a solid sphere settling in a homogenous fluid. Stokes discovered the steady state speed by equating the drag force with gravity and obtained the expression

$$U_s = \frac{2ga^2(\rho_s - \rho_f)}{9\mu}, \tag{2.3}$$

where U_s is the settling speed, g is the gravitational acceleration, a is the sphere radius, μ is the viscosity of the fluid, ρ_s is the density of the sphere and ρ_f is the density of the fluid [4]. In the absence of viscosity, the viscous term can be omitted yielding the Euler equation. In our applications, we consider the Navier-Stokes equations in the fluid domain with variable density and constant viscosity.

2.2 Equations for flow through a porous medium

Porous medium is by definition a material consisting of a rigid solid structure with interconnected void. The interconnectedness of the void allows the fluid to flow through the material in the presence of a pressure gradient. Henry Darcy discovered that the flow rate through porous media is directly proportional to the applied pressure difference. Darcy's law is denoted as

$$\mu\bar{\bar{\kappa}}^{-1} \cdot \vec{u} \quad = \quad \nabla p + \vec{f}, \tag{2.4}$$

where $\bar{\bar{\kappa}}$ is the permeability tensor of the porous medium, μ is the fluid viscosity, $\vec{u}$ is the fluid velocity, $\vec{f}$ is a body force and ∇p is the applied pressure gradient. For isotropic material $\bar{\bar{\kappa}}$ becomes a scalar. The velocity $\vec{u}$ so-called Darcy is the average velocity over a volume element incorporating both solid and fluid material [5].

A more general extension to Darcy's law is the Brinkman-Forchheimer equation, valid in a broad range of porosities, higher Reynolds numbers and applicable in the vicinity of interfaces [25]. While it is more general, it is also significantly more complex than Darcy's law. It includes an inertial term, a diffusive term and a quadratic drag. The Brinkman-Forchheimer equation is written as

$$\mu\bar{\bar{\kappa}}^{-1} \cdot \vec{u} = \nabla \cdot \bar{\bar{T}}_p - c_F\bar{\bar{\kappa}}^{-1/2}\rho_f|\vec{u}|\vec{u} + \vec{f}, \tag{2.5}$$

where $\bar{\bar{T}}_p = -p\bar{\bar{I}}+\mu_e(\nabla\vec{u}+(\nabla\vec{u})^T)$ is the stress tensor in the porous domain and c_f is a dimensionless form-drag constant. When the Reynolds number of the flow within the porous media is less than unity, it is sufficient to consider the Brinkman equation [26]. The Brinkman equation supplements Darcy's law with a diffusive term and is denoted as

$$\mu\bar{\bar{\kappa}}^{-1} \cdot \vec{u} \quad = \quad \nabla \cdot \bar{\bar{T}}_p + \vec{f}. \tag{2.6}$$

2.3 Equation of particle concentration transport

The density of a fluid may depend on a stratifying agent such as salt concentration or temperature, denoted by c. The stratifying agent is subject to the advection-diffusion equation, given by

$$\frac{\partial c}{\partial t} + \vec{u} \cdot \nabla c = D\nabla^2 c, \tag{2.7}$$

where D is the diffusion coefficient. Equation 3.10 is valid if the concentration field is source and sink free, the diffusion coefficient is constant and the velocity field is divergence free [27]. In our settling application (Chapter 3), we consider the advection and diffusion of heat or salt in water. The incompressibility of water implies that the divergence of the flow velocity is zero. There are no sources or sinks present and the diffusion coefficient variations are marginal so equation 3.10 is therefore applicable.

Chapter 3

Settling of a porous particle in density stratified fluid

3.1 Introduction

The settling of particles in fluids has long been an active area of research. Solid particles were studied first, beginning with the derivation of the Stokes drag law for spheres [28] in the absence of inertia. The effects of inertia were later considered theoretically [29] and experimentally [30], resulting in increasingly sophisticated empirical expressions for the drag coefficient of a settling solid particle. Settling or rising drops in the absence of inertia were studied simultaneously, resulting in a more general result, the Hadamard-Rybczinski drag, with applications ranging from rising bubbles to nearly solid drops [31]. In addition to inertial effects, the deformation of drops and bubbles, captured by the Weber and capillary numbers also influence the drag experienced by the drop [32]. More recently, the influence surfactants was also quantified [33].

When studying particles settling in the ocean or atmosphere, one must further account for the variable density of the surrounding fluid due to temperature and/or compositional variations. Such height-dependent density profiles, or stratifications, have a direct impact on the settling speed of particles through a reduction of the particle's buoyancy. In addition, the settling particles entrain lighter fluid downward, into the denser ambient fluid. The entrained fluid is then buoyant, and its upward motion then opposes the downward motion of the particle, enhancing its drag. We refer to this delay in settling as entrainment-induced retention. In recent years, the settling process in a stratified ambient has been studied extensively for solid particles [14, 15, 34–37]. Settling drops are also slowed by entrainment of lighter fluid, though to a lesser extent because they allow slip along their boundary and thus entrain less fluid [38,39]. The surface tension between the ambient and the drop may also change as drops settle, either leading to a sudden acceleration or effectively rendering the drop stationary [40].

More recently, porous particles settling in stratified ambients have been investigated [1,16,41–43] to describe the dynamics of marine snow. Marine snow is predominantly comprised of organic matter, including phytoplankton, protists, detritus, or fecal matter and contains small portions of inorganic material like sand and dust [44]. It plays an important role in the carbon transport into the deep ocean and contributes to remineralization [45–47]. These compounds aggregate in clumps that range between 100 μm and a few cm in size and are often over 99% porous [48, 49]. They accumulate in

thin layers where sharp density gradients are present [50, 51]. These layers are often positioned in the twilight zone, a hotspot for bacterial degradation [48, 49]. The main objective of these recent settling studies was to understand the interaction of density stratification with the settling of these porous particles, and how this interplay is affected by parameters such as the particle size, porosity, and density.

Porous particles are unique in that their average density is very close to that of the ambient fluid, owing to their small solid fraction. As they settle, porous particles transport their internal fluid downward. In a stratified ambient, the porous particle may then temporarily reach a level of neutral buoyancy, where the increased ambient density matches the combination of lighter internal fluid and small solid fraction of the particle. The permeability of these particles is often very small and the transport of heat or salt into the particle hence takes place mostly via diffusion. Once the density of the internal fluid has been increased through diffusive transport, the porous particle will resume its downward progress. We refer to this delay as a diffusion-induced retention. In theory, such a delay may also occur as heat diffuses into or out of solid particles, but this is rarely significant.

Recently, experimental studies have sought to quantify diffusion and entrainment-induced delays. Experiments with porous particles verified a quadratic dependence of retention time on particle size, similar to a diffusive exchange time [16]. Other experiments found that the settling speed was further reduced when the aggregates are less dense and found that sharper density gradients are characterized by a lower vertical velocity minimum [42, 43]. A mathematical model was proposed to capture the diffusion of a solute into the porous particle, and compared to experiments [1]. This model focused on low Reynolds number flows, assumed the size of the particle small compared to the length scale of the density gradient, and considered the ambient fluid density to be unperturbed by the settling particle. When comparing to experiments, it was found that entrainment was significant, and that the model could describe the settling dynamics of a porous particle provided an empirical parameter to quantify entrainment was included. However, this study did not systematically describe how this empirical parameter varied with parameters beyond the Reynolds number.

We present here numerical simulations of the settling of a porous sphere in a density-stratified ambient fluid and focus on quantifying both the entrainment and diffusion-induced retention times. We study the effects of varying the Reynolds, Péclet, and Darcy numbers, as well as the initial density profile and the ratio of the density difference between the lower and upper fluid layer to the density difference between the particle and the upper layer. In section 2, we present the governing equations. We describe and validate our numerical method in section 3 and compare our results with experimental data from [1]. We study the settling behavior of a porous sphere for different parameters and present the results in section 4. We discuss the physical mechanisms at play in section 5, and we present our conclusions in section 6.

3.2 Governing equations

We study numerically porous spherical particles settling under the influence of gravity in a homogenous or density-stratified ambient fluid. The particle is assumed to settle in a cylindrical domain, as depicted in Figure 3.1 (left). We take advantage of the symmetry of the system and simulate an axisymmetric vertical cut from the center to the edge of the cylinder.

We consider a stable stratification, where the density $\tilde{\rho}$ increases with depth. Throughout this paper, we use the tilde notation to represent dimensional variables. The fluid density undergoes a smooth transition from $\tilde{\rho} = \rho_u$ in the upper layer to $\tilde{\rho} = \rho_l$ in the lower layer. We assume that density variations are due to a linear dependence of the fluid density on a varying salt concentration

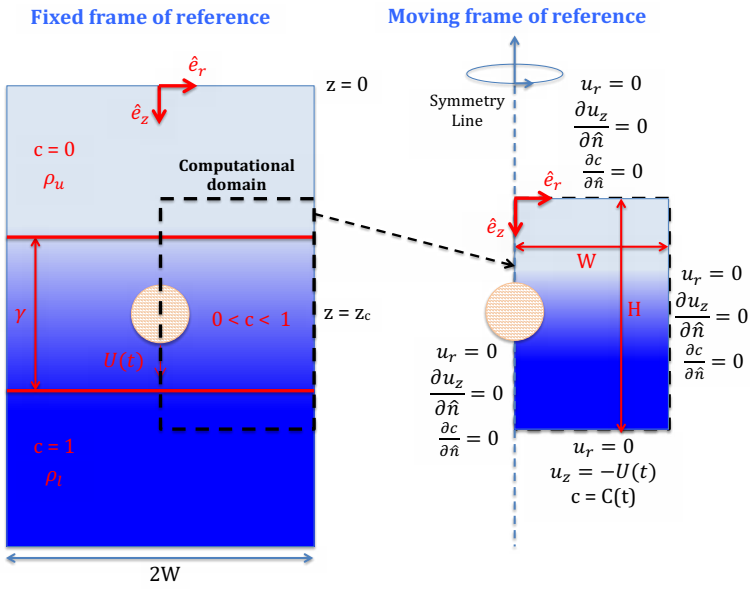

Figure 3.1: Schematics of the domain under consideration. A porous particle settles in a cylindrical container filled with density-stratified fluid. Left: Fixed frame of reference where the salt concentration c changes smoothly from zero in the upper layer to one in the lower layer with a transition layer thickness γ. Right: Moving frame of reference with the boundary conditions used in the simulations. Here $\vec{u} =< u_r, u_z >= u_r\hat{e}_r + u_z\hat{e}_z$.

$\tilde{c}$ with maximum concentration c_0

$$\tilde{\rho} = \rho_l \frac{\tilde{c}}{c_0} + \rho_u(1 - \frac{\tilde{c}}{c_0}). \tag{3.1}$$

Figure 3.1 shows the non-dimensional concentration of salt $c = \tilde{c}/c_0$ as the color intensity. The initial salt concentration $\tilde{c}_i$ approaches zero in the upper layer and c_0 in the lower layer, and varies with height $\tilde{z}$ as

$$\tilde{c}_i = \frac{1 - \mathrm{erf}(\frac{4(\tilde{z}-\tilde{z}_c)}{\tilde{\gamma}})}{2} c_0, \tag{3.2}$$

where $\tilde{\gamma}$ captures the depth over which the concentration, and therefore the density, varies. The corresponding initial density profile is $\tilde{\rho}_i$. The salt concentration is evolved in time using the advection-diffusion equation,

$$\frac{\partial \tilde{c}}{\partial \tilde{t}} + \tilde{\vec{v}} \cdot \tilde{\nabla}\tilde{c} = D\tilde{\nabla}^2\tilde{c}, \tag{3.3}$$

where $\tilde{\vec{v}}$ is the fluid velocity, $\tilde{t}$ is time and D the diffusivity constant for salt. Importantly, the concentration $\tilde{c}$ may diffuse and advect inside the porous particle, affecting the settling dynamics. We note that $\tilde{c}$ could also represent heat, another miscible fluid concentration, or any soluble agent.

The incompressible Navier-Stokes equations are used to describe the fluid flow, with the addition of a penalty term to describe the flow inside the porous sphere [52]

$$\tilde{\rho}\Big(\frac{\partial \tilde{\vec{v}}}{\partial \tilde{t}} + \tilde{\vec{v}} \cdot \tilde{\nabla}\tilde{\vec{v}}\Big) = -\tilde{\nabla}\tilde{P}_d + \mu\tilde{\nabla}^2\tilde{\vec{v}} + (\tilde{\rho} - \tilde{\rho}_i)g\hat{k} - M\frac{\mu}{\kappa}(\tilde{\vec{v}} - \tilde{U}(\tilde{t})\hat{k}) \tag{3.4}$$

$$\tilde{\nabla} \cdot \tilde{\vec{v}} = 0. \tag{3.5}$$

where μ is the fluid viscosity and $\tilde{P}_d$ is the dynamic pressure which is related to the pressure $\tilde{P}$ through $\tilde{P} = \tilde{P}_d + g\int_0^{\tilde{z}} \tilde{\rho}_i d\tilde{z}$, with g the gravitational acceleration. In the penalty term, we denote by κ the porous medium permeability. An indicator function M is used to denote the location of the porous medium, with $M = 1$ inside the porous particle and $M = 0$ in the unimpeded fluid. Details of how we solve for the vertical velocity of the porous particle $\tilde{U}(\tilde{t})$, taken as positive downward, are given below. The penalty term $M\frac{\mu}{\kappa}$ represents a porous drag proportional to the fluid velocity relative to the porous particle, and is similar to that used in derivations of Darcy's law [53]. We assume that μ is constant and focus on density variations, which have a dominant effect on the settling of particles.

To facilitate the analysis of our results, we non-dimensionalize our governing equations, and denote corresponding variables without a tilde. We use the radius of the particle a as a reference length. The reference speed is the Stoke's settling speed in the upper layer, $U_s = \frac{2ga^2}{9\mu}(\rho_s - \rho_u)(1-\phi)$ where ϕ is the porosity of the settling particle and ρ_s the density of its solid material. The reference density is the upper layer fluid density, ρ_u, and the reference concentration is the lower layer salt concentration c_0. In addition to the porosity ϕ, important non-dimensional numbers for our setup are the Reynolds number $\mathrm{Re} = \frac{\rho_u U_s a}{\mu}$, the ratio of inertial to the viscous forces, the Péclet number $\mathrm{Pe} = \frac{U_s a}{D}$, the ratio of inertial to diffusive effects, the Darcy number $\mathrm{Da} = \frac{\kappa}{a^2}$ a measure of the permeability of the porous particle, an ambient density ratio $\eta = \frac{\rho_l - \rho_u}{\rho_u}$, the dimensionless thickness over which density varies $\gamma = \frac{\tilde{\gamma}}{a}$, and a density difference ratio $\xi = \frac{\rho_l - \rho_u}{(\rho_s - \rho_u)(1-\phi)}$, which compares the ambient density variations to the density difference between the particle and the upper layer fluid. When $\xi > 1$, the settling dynamics are dominated by diffusion of salt into the particle. When $\xi < 1$, the particle is always heavier than its surrounding, and so is not significantly delayed as it settles. Noting that the non-dimensional gravitational term may be written as $\frac{ga}{U_s^2} = \frac{9\xi}{2\mathrm{Re}\eta}$ and $\frac{\tilde{\rho} - \tilde{\rho}_i}{\rho_u} = \eta(c - c_i)$, the governing equations become, in non-dimensional form

$$\frac{\partial c}{\partial t} + \vec{v}\cdot\nabla c = \frac{1}{\mathrm{Pe}}\nabla^2 c \tag{3.6}$$

$$\rho\Big(\frac{\partial \vec{v}}{\partial t} + \vec{v}\cdot\nabla\vec{v}\Big) = -\nabla P_d + \frac{1}{\mathrm{Re}}\nabla^2\vec{v} + \frac{9\xi}{2\mathrm{Re}}\,(c - c_i)\hat{k} - \frac{M}{\mathrm{Da\ Re}}(\vec{v} - U\hat{k}) \tag{3.7}$$

$$\nabla\cdot\vec{v} = 0 \tag{3.8}$$

Here, the third term in equation (3.7) captures the local buoyancy of the fluid. To allow more efficient numerical simulations, we introduce a frame of reference moving downward with vertical velocity $U(t)$, chosen such that the porous particle remains in the center of the domain. Figure 3.1 (right) shows the domain in a moving frame of reference that is used in numerical simulations. We calculate the vertical velocity $U(t)$ by balancing the buoyancy and drag forces on the particle. In dimensionless form, the mass of the displaced fluid is $\frac{4\pi}{3}(1 + \eta\bar{c}_i)$ and we obtain

$$m\frac{dU}{dt} = (m - \frac{4\pi}{3}(1 + \eta\bar{c}_i))\ \frac{9\xi}{2\mathrm{Re}\ \eta}\ + \iint_S \bar{\bar{T}}\cdot d\vec{S}$$

where $\frac{4\pi}{3}$ is the dimensionless volume of our sphere, $\bar{c}_i$ is the average value of c_i within the sphere, $\bar{\bar{T}} = -P_d\bar{\bar{I}} + \frac{1}{\mathrm{Re}}(\nabla\vec{u} + (\nabla\vec{u})^T)$ is the stress tensor, and S is the surface of the particle. Here $m(t)$ is the dimensionless mass of the particle including the fluid within the sphere,

$$m(t) = \frac{4\pi}{3}\left((1-\phi)\frac{\rho_s}{\rho_u} + \phi\bar{\rho}\right) = \frac{4\pi}{3}\left((1-\phi)\frac{\rho_s}{\rho_u} + \phi(1 + \eta\bar{c})\right) = \frac{4\pi}{3}\left(1 + \frac{\eta}{\xi} + \phi\eta\bar{c}\right) \tag{3.9}$$

where $\bar{\rho}$ is the average fluid density within the spherical particle, and $\bar{c}$ the corresponding average concentration. We rewrite our governing equations in a moving frame of reference,

$$\frac{\partial c}{\partial t} + \vec{u}\cdot\nabla c = \frac{1}{\mathrm{Pe}}\nabla^2 c \tag{3.10}$$

$$\nabla\cdot\vec{u} = 0 \tag{3.11}$$

$$\rho\Big(\frac{\partial \vec{u}}{\partial t} + \vec{u}\cdot\nabla\vec{u}\Big) = -\nabla P_d + \frac{1}{\mathrm{Re}}\nabla^2\vec{u} + \frac{9\xi}{2\mathrm{Re}}(c-c_i)\hat{k} + (1+\eta c)\frac{dU}{dt}\hat{k} - \frac{M}{\mathrm{Da\ Re}}\vec{u} \tag{3.12}$$

$$m\frac{dU}{dt} = 6\pi(1-\xi(\bar{c}_i-\phi\bar{c}))\left(\frac{1}{\mathrm{Re}} - \frac{2}{9}\frac{\eta}{\xi}\frac{dU}{dt}\right) + \iint_S \bar{\bar{T}}\cdot d\vec{S} \tag{3.13}$$

$$\frac{dZ_s}{dt} = U, \tag{3.14}$$

where $\vec{u} = \vec{v} - U\hat{k}$ is the relative velocity and $Z_s(t)$ the height of the particle at time t, taken as increasing downward.

Our moving frame of reference has radius W and height H (denoted $W \times H$), as shown in Figure 3.1 (right). We apply Neumann boundary condition for c at the symmetry axis and at the upper and right wall ($\frac{\partial c}{\partial \hat{n}} = 0$, where $\hat{n}$ is the unit normal at the boundaries). We use time-dependent Dirichlet boundary conditions $c = C(t)$ at the lower boundary, where $C(t) = c_i(Z_s(t) + H/2)$. For velocities in the vertical direction, we apply Neumann boundary conditions ($\frac{\partial u_z}{\partial \hat{n}} = 0$) on all boundaries except the bottom boundary where we apply time-dependent Dirichlet boundary conditions ($u_z = U(t)$). We assume that the radial velocity component is zero at all boundaries ($u_r = 0$). The imposed boundary conditions are depicted in Figure 3.1 (right).

3.3 Numerical method and validation

We solve the governing equations described in section 2 numerically using finite differences on a uniform staggered grid. We employ second order central differences for our spatial derivatives and explicit Euler (first order) for our time integration. We find the pressure using a projection method [54], which forces the velocity to remain divergence free. The porous sphere is separated from the homogenous fluid by an interface constructed using Lagrangian markers connected with cubic splines. In general, the method allows markers to move with the particle, but in our moving frame of reference, the porous sphere is fixed in the center of the domain. We capture the transition from porous medium to pure fluid by employing the Volume-of-Fluid approach commonly used in multiphase flow applications [55–57]. We assume that the velocity, pressure, concentration, and stresses are continuous across the interface. In our moving frame of reference, the vertical velocity of the particle $U(t)$ is calculated by integrating equation (3.13). The surface integral is computed using a composite trapezoidal method to sum the surface stresses. This operation is the least numerically accurate, as it requires estimating velocity derivatives near the interface. We also integrate $U(t)$ in time to obtain the position $Z_s(t)$ of the particle, equation (3.14), which is then used in equation (3.2) to retrieve the bottom concentration $C(t) = c_i(Z_s + H/2)$. The obtained velocity and concentration are then used as conditions on the lower boundary, and are updated at every time step.

The initial concentration is given by the dimensionless version of equation (3.2). We initiate simulations with the velocity and pressure fields corresponding to 0.8 times the Stokes flow around a solid sphere settling in a fluid of density $\rho_u = 1$. We let the system evolve to steady-state in a homogeneous ambient. We note that the Stokes settling speed, U_s, used as a reference velocity is derived by assuming an infinitely large domain and neglecting inertial effects ($\mathrm{Re} = 0$). Hence, we expect in the simulations that non-dimensional velocities will be smaller unity due to both inertial

and wall effects. For this same reason, we initiate the simulations at a fraction of the Stokes flow around a solid sphere.

To verify the numerical convergence of the simulations, we first simulate the settling of a sphere with Re = 3.4 in a homogenous fluid ($c = 0$). Figure 3.2 (left) shows the terminal vertical velocity of the sphere in a domain of size (2×4) for resolutions varied between $\Delta z = 2^{-8}$ and $\Delta z = 2^{-5}$. We considered three different values of the Darcy number, and report the settling vertical velocity for each. In the vicinity of the sphere's surface, the velocity gradients become larger for small values of Da and hence a higher resolution is required to obtain a similar numerical accuracy. If we extrapolate toward higher resolution, the vertical velocity is seen to decrease as Da $\to 0$, which is consistent with literature results [58] [59].

In Figure 3.2 (right), we keep the resolution fixed at $\Delta z = 2^{-6}$ and vary the domain size between 2×4 and 16×32. We find that the vertical velocity appears to approach domain size independence when the boundaries are approximately 16 radii away from the sphere. We conclude that the simulations accurately recover the settling of a solid sphere for sufficiently fine resolution and sufficiently large domain size.

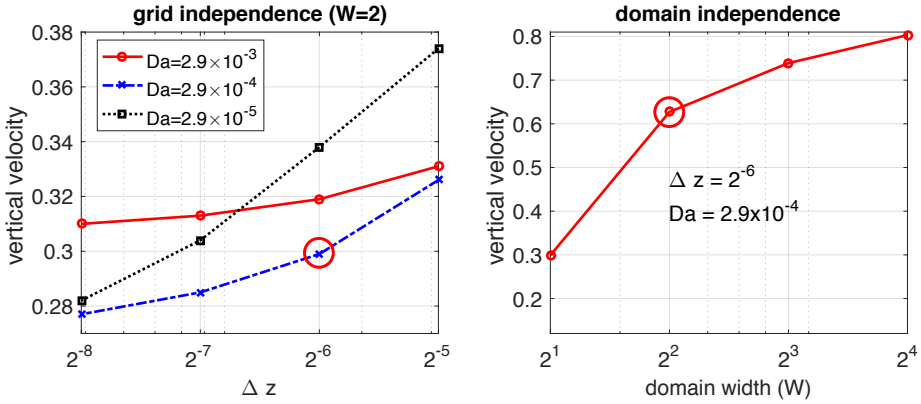

Figure 3.2: Left: Dependence of the vertical velocity on the resolution for different values of Da. Right: Dependence of the vertical velocity on domain size for $dz = 2^{-6}$ and Da $= 2.9 \times 10^{-4}$. The red circles indicate the values used in later simulations, unless otherwise specified.

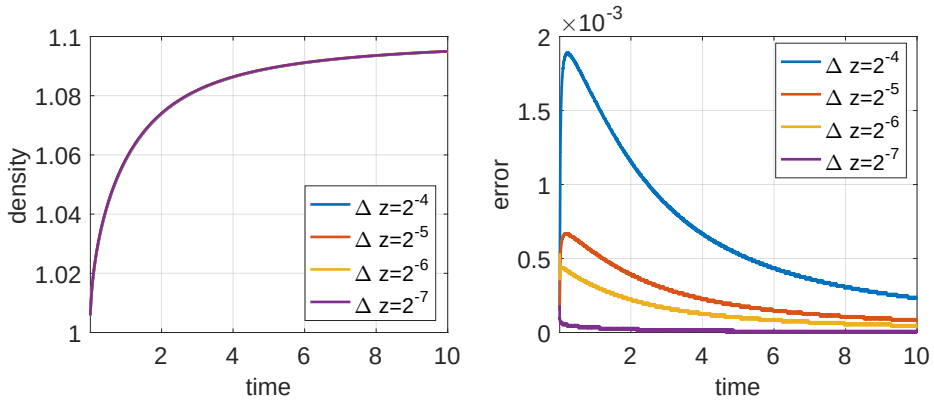

Figure 3.3: Left: Time evolution of the average density for a sphere with porosity $\phi = 0.992$, and density $\rho_s = 1$ filled with fluid of density $\rho_u = 1$ that is instantly submerged in a fluid of density $\rho_l = 1.1$ for Pe $= 6.67$. Right: Error of the density calculation, which is computed based on the results obtained with $\Delta z = 2^{-9}$.

Because diffusion effects are dominant in this system, we next present the convergence of our diffusion solver. In the absence of gravity, and with Pe $= 6.67$, we allow heavier fluid $\rho_l = 1.1$ to diffuse into a porous sphere with porosity $\phi = 0.992$ and solid density $\rho_s = 1$ initially filled with lighter fluid, $\rho_u = 1$. We track the average density of the sphere over time, as shown in Figure 3.3 (left). We show in Figure 3.3 (right) the error as calculated based on our highest resolution of $\Delta z = 2^{-9}$. We find that diffusive effects are well captured with our chosen resolution of $\Delta z = 2^{-6}$, with error below 0.1%.

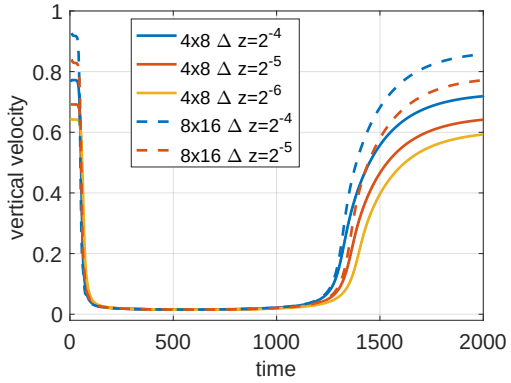

Figure 3.4: Comparison of vertical velocity versus time simulated for different resolutions and domain sizes as a porous sphere settles through a two-layer density stratification. Here Re $= 2.22$, Pe $= 1746$, $\eta = 0.023$, $\gamma = 46.4$, and $\xi = 5.5$.

Next, we present a porous sphere settling in a stratified ambient fluid and explore the effects of resolution and domain size on the vertical velocity over time. Figure 3.4 shows the vertical velocity of a porous particle as a function of time as it settles from a layer of lighter fluid into a layer of heavier fluid. Due to its lighter inner fluid, the particle slows down and stays nearly stationary while its density increases via diffusive effects and it eventually resumes settling. We first note that wall effects remain present in an 4×8 domain, resulting in a slower vertical velocity away from the transition region compared to a 8×16 domain. However, the domain size only has a minimal impact on the

duration of the period when the particle has a vertical velocity close to zero, presumably because the amount of entrained fluid does not change appreciably with domain size. Similarly, increased resolution results in slower settling velocities in uniform ambients, but only slightly increase retention time, as diffusive effects are well captured even at relatively low resolutions.

In the rest of this paper, the resolution and size of our domain are chosen as a trade-off between minimizing wall effects and computational efficiency. Unless otherwise specified, we use an 4×8 domain with $\Delta z = 2^{-6}$, values shown as red circles in Figure 3.2. Wall effects, resulting in an increased drag and so a reduced velocity, are thus present but not dominant. We also expect the resolution used to result in an overestimate of the vertical velocity, while remaining within 15% of a fully resolved simulations. With these choices, we obtain in a fluid of uniform density $\rho = \rho_u = 1$ a non-dimensional vertical velocity of 0.63, compared to a vertical velocity of $U_s \approx 0.69$ obtained using the empirical drag law by White [4], where the drag coefficient is

$$C_D = \frac{12}{\mathrm{Re}} + \frac{6}{1 + \sqrt{2}\mathrm{Re}^{0.5}} + 0.4. \tag{3.15}$$

Note that this formula has been adapted to a Reynolds number based on particle radius. The reduced computational effort resulting of these choices of domain size and resolution allow the exploration of a broader range of parameters.

We conclude our validation by comparing simulations to a laboratory experiment where a porous spherical particle settles in a two-layer density-stratified ambient [1]. The permeability of the sphere is not explicitly given, but it is said to be extremely small. For simplicity, we therefore use the smallest value of Da we can accurately resolve, $\mathrm{Da} = 3 \times 10^{-4}$. In addition, we prevent advective transport of the concentration c within the sphere by modifying equation (3.10) for this experimental validation and for results labeled $\mathrm{Da} = 0$. We thus use

$$\frac{\partial c}{\partial t} + (1 - M)\vec{u} \cdot \nabla c = \frac{1}{\mathrm{Pe}} \nabla^2 c, \tag{3.16}$$

where the $(1 - M)$ factor blocks the advection of the soluble agent inside the porous sphere. While the fluid parameters (density, viscosity, and diffusivity) were precisely measured in experiments and were matched exactly in the simulations, the density and porosity of the particle were not measured directly. Using the published values of $\rho_s = 1.4$ g/cm^3 and $\phi = 0.992$, we obtained fairly good agreement in retention time, as shown by the yellow curve in Figure 3.5 (left). We present these plots dimensionally for easier comparison to published experimental results. However, we note that, as explained in [1], the porosity was obtained by matching the experimental settling velocity in a uniform ambient, approximately $U_s = 0.2635$ cm/s, to the Stokes settling speed of a porous sphere of solid density $\rho_s = 1.4$ g/cm^3. Accounting for inertial effects through equation (3.15), we recalculated the porosity to account for inertial effects and found $\phi = 0.9896$. Although the difference in porosity is small, retention times are very sensitive to $\xi = \frac{\rho_l - \rho_u}{(\rho_s - \rho_u)(1-\phi)}$, and this small difference in ϕ has a large overall effect, as can be seen in Figure 3.5 (right). For this recalculated value of the porosity, the governing parameters of this system are $\mathrm{Re} = 2.22$, $\mathrm{Pe} = 1746$, $\eta = 0.023$, $\gamma = 46.4$, and $\xi = 5.5$.

The simulations are seen to yield a shorter retention time than experimental measurements for the recalculated porosity. However, given the sensitivity of the retention time to the exact value of the porosity and the error associated to the calculation of the porosity, we conclude that the retention time in the simulations are an acceptable approximation of the retention time in the experiments.

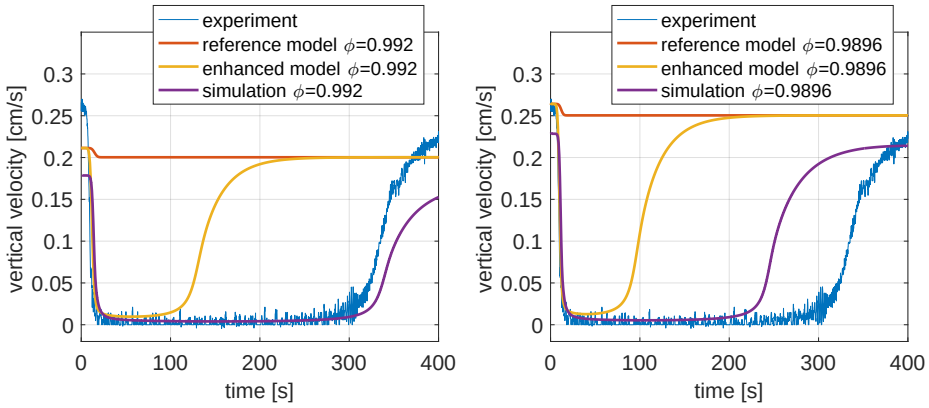

Figure 3.5: Vertical velocity versus time for experimental data [1] in blue, reference model (equation (3.17)) in red, enhanced model (equation (3.19)) in yellow, and simulations in purple. Left: The porosity is $\phi = 0.992$, the value given in [1]. Right: The porosity is $\phi = 0.9896$, a value derived by accounting for inertial effects in a uniform ambient. Other parameter values are Re $= 2.22$, Pe $= 1746$, $\eta = 0.023$, $\gamma = 46.4$, and $\xi = 5.5$.

For future comparison, we present two models that describe the settling of a porous sphere. The first, shown in red in Figure 3.5, is a simple reference model where the density of the fluid inside the particle is always assumed to be that of the ambient fluid at that level. This is equivalent to assuming that diffusion is immediate (Pe $= 0$). In non-dimensional terms, the mass of the particle is then $m_r(t) = \frac{4\pi}{3}(1 + \frac{\eta}{\xi} + \eta\phi c_i)$. Balancing drag and buoyancy, our reference model is then

$$\begin{aligned} m_r \frac{dU_r}{dt} &= -\text{sgn}(U_r)\frac{\pi\ C_D}{2}(1+\eta c_i(Z_r))\ U_r^2 + \frac{6\pi}{\text{Re}}\left(1-(1-\phi)\xi c_i(Z_r)\right) \\ \frac{dZ_r}{dt} &= U_r \end{aligned} \tag{3.17}$$

where U_r is the vertical velocity of the particle, Z_r its vertical position, and $(1 + \eta c_i(Z_r))$ is the initial density at the level Z_r. Unsurprisingly, the simple reference model does not capture the near-stagnant period, since in this model the particle always maintains its excess density.

We also consider an enhanced model first introduced in [1] that includes diffusive effects in the limit of low Reynolds number, but neglects fluid entrainment effects. The concentration within the particle, c_p, when at level Z_e, is then corrected to

$$c_p(Z_e) = c_i(Z_e) - \sum_{n=1}^{\infty} \frac{6}{\pi^2 n^2} \int_0^t e^{\frac{n^2\pi^2(\tau - t)}{\text{Pe}}} \frac{dc_i(Z_e(\tau))}{d\tau} d\tau \tag{3.18}$$

where the summation term comes from solving the heat equation assuming an outer concentration profile unperturbed by fluid motion. We extend this enhanced model to account for non-zero Reynolds numbers via equation (3.15) and obtain a model of the particle's vertical velocity, U_e, and position, Z_e, given by

$$\begin{aligned} m_e \frac{dU_e}{dt} &= -\text{sgn}(U_e)\frac{\pi\ C_D}{2}(1+\eta c_i(Z_e))\ U_d^2 + \frac{6\pi}{\text{Re}}\Big(1-(1-\phi)\xi c_i(Z_e) + \xi\phi(c_i(Z_e) - c_p)\Big) \\ \frac{dZ_e}{dt} &= U_e. \end{aligned} \tag{3.19}$$

The vertical velocity over time predicted by this enhanced model is shown in Figure 3.5 as yellow curves. Including diffusive effects shows a significant slowing of the particle. However, this model

also underestimates the retention time, as explained in [1] because it neglects the fluid displacement around the particle. In reality, salt must diffuse through both the particle itself and the entrained fluid before settling may resume.

Because the effects of diffusion through the particle on retention time are well understood through the enhanced model and experiments presented in [1], we will focus primarily on how fluid entrainment influences the settling time. In section 5, we compare simulation results with the reference model given by equation (3.17) and the enhanced model outlined in equation (3.19).

3.4 Simulation Results

We report in this section the numerically computed vertical velocity and position of the particle versus time of a porous particle settling through a two-layer stratification with a transition of thickness γ. We aim to describe and quantify the underlying dynamics causing delays in settling. We vary the governing non-dimensional parameters over a range approximately corresponding to previously reported experiments. The values we consider are bounded by $1 \leq \mathrm{Re} \leq 64$, $109 \leq \mathrm{Pe} \leq 6984$, $0 \leq \mathrm{Da} \leq 0.01$, $0.5 \leq \xi \leq 2.2$, and $1 \leq \gamma \leq 64$. We keep $\eta = 0.00576$ and $\phi = 0.992$ fixed.

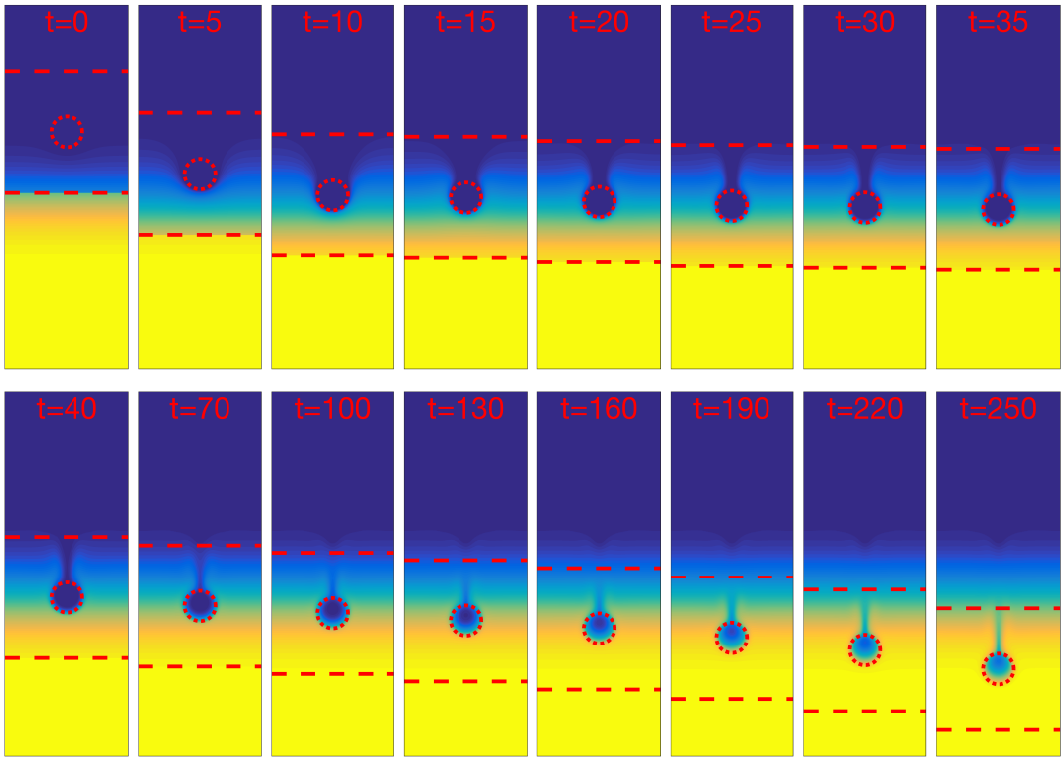

Figure 3.6: Snapshots of a porous particle settling from a lighter to a heavier layer at several times, with blue showing low values of the concentration c and yellow high values of c. The red circle indicates the porous sphere, and the red dashed lines the moving frame of reference. The domain shown is from $-4 \leq r \leq 4$ and $38 \leq z \leq 62$, and the parameters for this simulation are $\mathrm{Re} = 4$, $\mathrm{Pe} = 1746$, $\xi = 1.8$, $\gamma = 11.6$, $\eta = 0.0058$, $\mathrm{Da} = 5 \times 10^{-4}$ and $\phi = 0.992$

.

We begin by simulating a typical porous sphere settling in a two-layer stratification. In Figure 3.6 we show several snapshots of the concentration c, with blue corresponding to $c = 0$ and yellow to $c = 1$, and the position of the sphere, as the dashed red circle. The moving frame of reference is also shown as the dashed red lines. The displacement between consecutive frames is indicative of the sphere's vertical velocity. The first row shows images taken every 5 time units, and the lower row shows images taken every 30 time units. A video of the entire settling process is also available [60]. The parameters here are in the middle of the range of this study: Re $= 4$, Pe $= 1746$, $\xi = 1.8$, $\gamma = 11.6$, and Da $= 5 \times 10^{-4}$. Prior to the first image presented, the sphere was left to reach steady-state in a uniform ambient. As it approaches the transition layer, the sphere begins to slow, as can be seen at times $t = 10$ and $t = 15$. The wake behind the sphere, with concentration approximately zero, is then very broad owing to the sudden deceleration. When inertial effects are large enough and the transition layer is sufficiently sharp, bouncing may occur as the sphere overshoots its temporary level of neutral buoyancy, as discussed in more detail below. Once the sphere has lost its original momentum, it progresses slowly across the transition layer, as diffusion slowly increases its mass. The concentration within the sphere can be seen to increase slowly between times $t = 15$ and $t = 250$. Eventually, around $t = 220$, the sphere exits the transition layer. Its internal fluid remains relatively light, and as it settles into the lower layer, it will continue to become heavier, and accelerate until reaching a new steady-state where its internal fluid density matches that of the ambient.

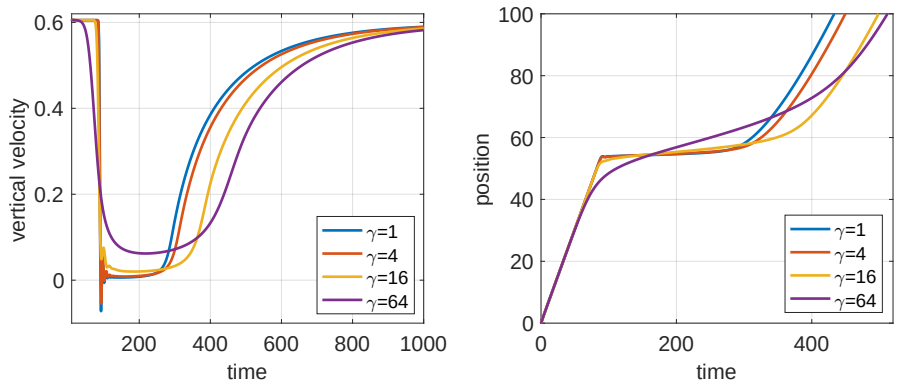

Figure 3.7: Left: Non-dimensional particle vertical velocity over time for several transition layer thicknesses γ. Right: Distance settled over time for the same values of γ. Other than γ, parameters used are the same as in the case shown in Figure 3.6.

We present in Figures 3.7 (left) and 3.7 (right) the vertical velocity and position of the particle, respectively, over time as it settles over a depth of 100 radii centered on the transition region for different transition depths γ. We vary γ between 1 and 64 and keep all other parameters constant at the values used in the simulation shown in Figure 3.6. For sharper transitions (small γ), the particle reaches a lower minimum vertical velocity. However, the retention time is overall smaller because the particle quickly accelerates again. Figure 3.7 (right) shows that for the largest transition depth considered, $\gamma = 64$, the particle slows down at a higher position as it reaches the transition layer earlier. It initially falls behind particles settling in a sharper transition, but due to the slow density variation, it maintains a relatively high minimum vertical velocity, and temporarily overtakes particles settling in sharper density gradients. Since the transition layer depth is much longer when $\gamma = 64$, the particle stays in the density gradient region longer and ends up with the longest retention time. However, the retention time is nearly independent of transition depth when $\gamma \geq 32$.

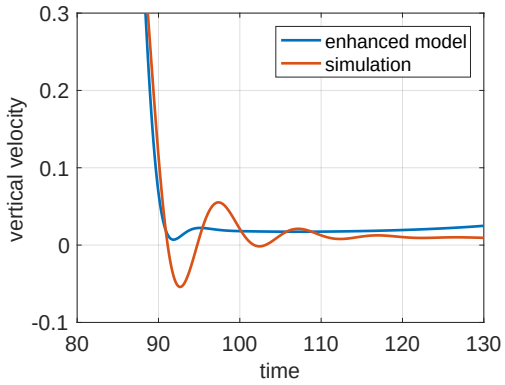

Figure 3.8: Enlarged portion of Figure 3.7 (left) showing the particle's vertical velocity over time for $\gamma = 4$ and other parameters as in Figure 3.6. We show the vertical velocity computed via the enhanced model (equation (3.19)) in blue and simulations in red.

When a particle with sufficiently high inertia approaches a sharp density gradient, in these simulations, as seen for $\gamma = 1$ and $\gamma = 4$, it experiences an oscillatory vertical motion that we refer to as bouncing, as can be seen in Figure 3.7 (left) and in the enlarged plot of the case $\gamma = 4$ shown in Figure 3.8. Inertia causes the particle to sink to a depth with higher ambient density than its own, where buoyancy then pushes it back up. This bouncing motion is captured in the simulations as well as, to a lesser extent, in the enhanced model (equation (3.19)), see Figure 3.8. In the enhanced model, the amplitude of the oscillation is not sufficiently large to cause the velocity to reverse direction. The more pronounced oscillation amplitude in the simulations indicates that entrainment plays a signifiant role in the bouncing process, as is the case for solid particles [14] and drops [40] settling in a sharp stratification. In the simulations, when the layer thickness was kept constant at $\gamma = 11.6$, and the Reynolds number was varied, bouncing was observed for $\mathrm{Re} \geq 8$. When the Reynolds number was kept constant at $\mathrm{Re} = 4$ and the layer thickness was varied, bouncing was observed for $\gamma \leq 8$.

We consider next variations in the Péclet number, a measure of the ratio of inertial effects to diffusive effects, with higher Pe indicating that diffusion is slow and that advection is the dominant transport mechanism. Inside the porous particle, fluid flow is negligible for the Darcy number considered, $\mathrm{Da} = 5 \times 10^{-4}$, and hence diffusion is the main mechanism of salt transport into the particle. For smaller Pe, salt diffuses quickly into the particle, making it heavier than the ambient fluid. As can be seen in Figure 3.9, the particle decelerates upon approaching the transition region but passes through fairly quickly. As Pe gets larger, diffusion becomes slower, almost allowing the particle to come to rest. The particle stays nearly stagnant for a long time before it once again becomes dense enough to proceed into the denser lower fluid. Upon entering the stratification, the particle experiences oscillations in its velocity for all simulated Pe, though without direction reversal. The total settling and retention time is seen to increase significantly with increasing Pe.

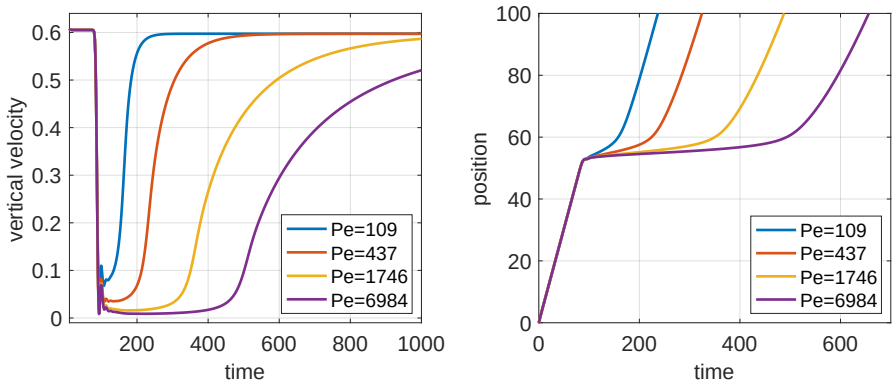

Figure 3.9: Left: Non-dimensional vertical velocity over time for several Pe. Right: Distance settled over time for the same values of Pe. Other than Pe, parameters used are the same as in the case shown in Figure 3.6.

We study next the effects of varying the Darcy number, and plot the velocity and position versus time in Figure 3.10. The settling velocity in homogenous ambient fluid is higher for larger Da as the particle experiences a lower drag. The drag converges quickly to that of a solid particle for smaller Da. A value of Da = 0 indicates a particle with no internal advection of fluid where diffusion is the sole mean of salt transport. The slower rate of salt penetration into the particle and enhanced entrainment at small Da, result in slower settling across the density transition layer. Particles with larger Da are clearly seen to accelerate earlier across the density gradient, as transport of salt into the particle occurs through both advection and diffusion. The retention time in density-stratified fluid is thus clearly dependent on Da.

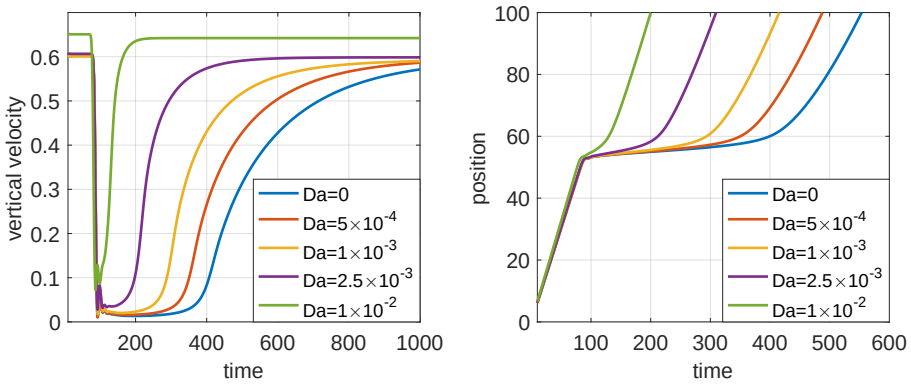

Figure 3.10: Left: Non-dimensional vertical velocity over time for several Da. Right: Distance settled over time for the same values of Da. Other than Da, parameters used are the same as in the case shown in figure 3.6.

We vary next the parameter $\xi = \frac{\rho_l - \rho_u}{(\rho_s - \rho_u)(1-\phi)}$, which captures the importance of diffusive effects on the settling dynamics of a porous particle. For $\xi < 1$, the particle experiences only a slight reduction in vertical velocity because it is always heavier than the lower layer fluid and does not rely on diffusion to settle through the transition layer. For $\xi \geq 1$, the retention time increases quickly, as the particle nearly comes to rest while salt diffuses into the particle. The vertical velocity versus

time, shown in Figure 3.11 (left), shows a very similar pattern for all values of ξ, with a nearly stationary period that increases with ξ. The retention time is thus strongly correlated with ξ.

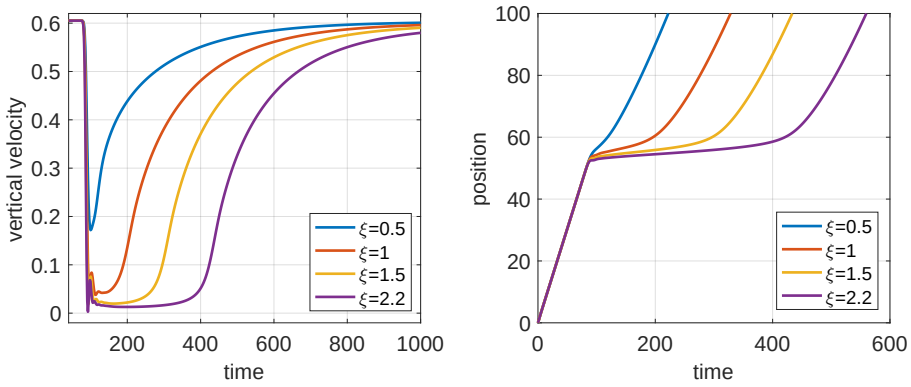

Figure 3.11: Left: Non-dimensional vertical velocity over time for several ξ. Right: Distance settled over time for the same values of ξ. Other than ξ, parameters used are the same as in the case shown in figure 3.6.

Lastly, we study settling particles with several different Reynolds numbers. Vertical velocity and position of the particle versus time are shown in Figure 3.12. Bouncing is seen to occur for $\mathrm{Re} = 1$ and $\mathrm{Re} = 4$ in Figure 3.12 (left), and is also visible in the position plot, Figure 3.12 (right) when looking closely. The nearly stationary period is seen to have nearly the same duration for all Reynolds numbers. However, the non-dimensional settling speed in a uniform ambient decreases with higher Re. This is somewhat counter-intuitive, but results from the selection of the Stokes' vertical velocity for our non-dimensionalization. Figure 3.12 (right) shows that the highest Reynolds number particles are slowest in non-dimensional time units, which seems to be mostly attributable to their slower non-dimensional settling speed in a uniform ambient.

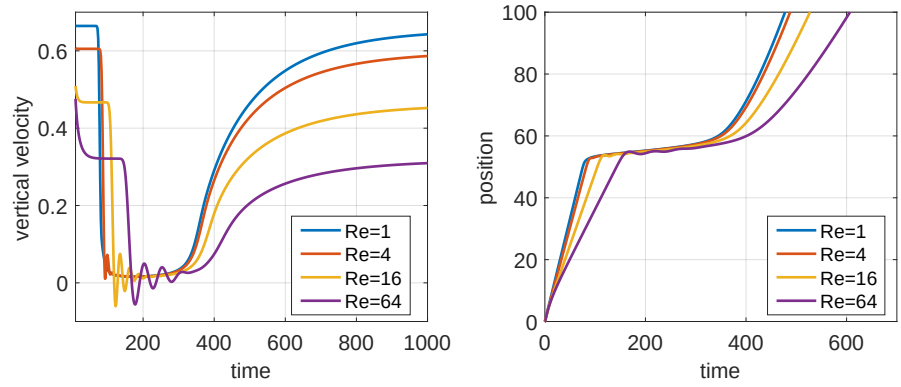

Figure 3.12: Left: Non-dimensional vertical velocity over time for several Re. The particle experiences bouncing for $\mathrm{Re} \geq 8$. Right: Distance settled over time for the same values of Re. Other than Re, parameters used are the same as in the case shown in Figure 3.6.

3.5 Discussion

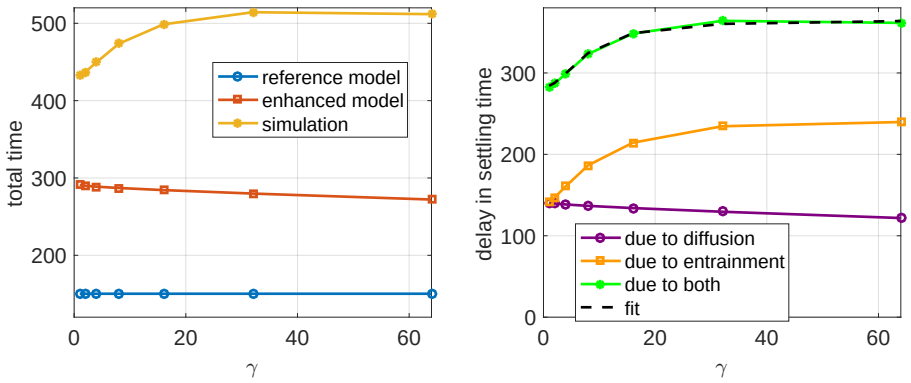

Figure 3.13: Left: Time required to settle a distance of 100 radii across a density gradient for several transition layer thicknesses γ. The reference time t_{ref} (blue) was computed using equation (3.17), the enhanced model time t_{enh} (red) using equation (3.19), and the simulation time t_{sim} (yellow) using our full numerical simulations. Right: Delay in settling time due to diffusion within the particle ($t_{\text{enh}} - t_{\text{ref}}$, purple), diffusion within the entrained fluid ($t_{\text{sim}} - t_{\text{enh}}$, orange), and both ($t_{\text{sim}} - t_{\text{ref}}$, green). The fit of equation (3.20) is shown as a dashed black line.

We now proceed to quantify the total settling time of a porous sphere settling through a two-layer density stratification and compare it to the models introduced in Section 3. We consider the time taken in our simulations for a porous sphere to settle through a column of height 100 radii centered on the transition layer and denote it t_{sim}. We compare this to the settling time t_{ref} computed by our reference model, which assumes instantaneous diffusion as described in equation (3.17). We also compute the time t_{enh} taken by a particle described by the enhanced model of equation (3.19), which includes a finite diffusion time but does not account for diffusion through the entrained fluid. We may then identify what fraction of the delay is due to diffusion within the porous sphere, and what fraction is due to diffusion within the entrained fluid. Because this delay is computed over a distance extending well beyond the transition region, we expect that it also provides a good estimate of the delay a porous sphere would experience if taller water columns were considered.

For each parameter, we provide an empirical formula fitting the delay observed in the simulations. These formulae were obtained based on our data and accounting for known limiting cases. Other functional forms may provide acceptable fits as well, but the ones presented here were chosen as simple forms that closely matched our data.

The computed reference model, enhanced model, and simulations times are shown for several transition layer thicknesses γ in Figure 3.13 (left). We first note that the reference and enhanced model times are nearly independent of γ. The delay due to diffusion within the sphere, captured by $t_{\text{enh}} - t_{\text{ref}}$ shown in Figure 3.13 (right) is therefore nearly constant, as time required for salt to diffuse into the particle varies only weakly with γ. However, the simulations show that large transition layers contribute to slowing down the porous sphere, at least for $\gamma < 32$. Delays due to diffusion in the entrained fluid are captured by $t_{\text{sim}} - t_{\text{enh}}$ and labelled as "due to entrainment" in Figure 3.13 (right). These delays increase with γ before leveling off. In a sharp density gradient, the entrained fluid is more buoyant, and tends to detach from the porous particle, leaving less fluid through which salt must diffuse, thus resulting in a shorter delay. For a sufficiently large value of γ, the entrained fluid travels with the porous particle, resulting in a longer delay. While for small γ the delay due to diffusion within the particle is similar to that due to entrainment, for larger γ

values, diffusion through entrained fluid is dominant. As will be seen below, γ only has a relatively small effect on the total settling time compared to other parameters. We fitted the delay relative to the reference model as a function of γ and found

$$t_{\text{sim}}(\gamma) \approx t_{\text{ref}}(\gamma) + 365\left(1 - \frac{0.225}{1 + 0.016\gamma^2}\right). \tag{3.20}$$

This fit is shown as the black dashed line in Figure 3.13 (right). Figure 3.14 (left) shows the computed total settling times as a function of the Péclet number. The reference model assumes $\text{Pe} = 0$ and so does not allow variations in Péclet numbers. The time found using the enhanced model (equation (3.19)) includes diffusion through the particle only, and so finds a settling time that increases nearly linearly with Pe, since the time required for diffusion to penetrate a radius a into the particle scales as $\tilde{t}_{\text{diff}} \sim a^2/D$. This is consistent with results reported by [16] and non-dimensionalizes to $t_{\text{diff}} \sim \text{Pe}$. The additional delay due to diffusion through entrained fluid is more complicated, as can be seen in Figure 3.14 (right), where it is seen to be non-monotonic. For small Pe, the additional delay is relatively small, as diffusion through the entrained fluid occurs quickly. As Pe increases, the delay increases until reaching a maximum near $\text{Pe} = 1800$. The delay due to entrainment then decreases with Pe. By observing videos of the concentration [60–62], one can see the volume of entrained fluid decreasing with increasing Pe. In a stratified ambient, the entrained fluid is always buoyant. For sufficiently large Pe, diffusion is slow and so is the particle's motion. The entrained fluid then has time to detach from the porous particle, effectively resulting in less entrainment. The volume of fluid through which salt must diffuse then decreases with increasing Pe, reducing the entrainment delay. The delay due to the combined effects of diffusion and entrainment remains monotonically increasing with Péclet number, but in a logarithmic manner. We fit the additional delay relative to the reference model as a function of Pe, and enforce that in the limit Pe the delay should approach zero to find

$$t_{\text{sim}}(\text{Pe}) \approx t_{\text{ref}}(\text{Pe}) + 120\log(1 + \frac{\text{Pe}}{100}) \tag{3.21}$$

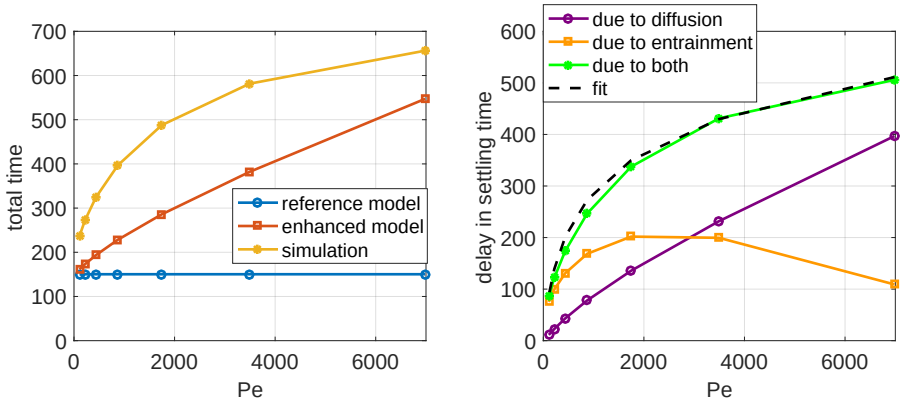

Figure 3.14: Left: Time required to settle a distance of 100 radii across a density gradient for several Péclet numbers Pe. The reference time t_{ref} (blue) was computed using equation (3.17), the enhanced model time t_{enh} (red) using equation (3.19), and the simulation time t_{sim} (yellow) using our full numerical simulations. Right: Delay in settling time due to diffusion within the particle ($t_{\text{enh}} - t_{\text{ref}}$, purple), diffusion within the entrained fluid ($t_{\text{sim}} - t_{\text{enh}}$, orange), and both ($t_{\text{sim}} - t_{\text{ref}}$, green). The fit of equation (3.21) is shown as a dashed black line.

We present in Figure 3.15 (left) the computed settling times as a function of the Darcy number within the porous sphere, Da. Neither the reference nor the enhanced model allow any flow within

the sphere, and their predictions are therefore independent of Da. In the simulations, larger values of Da allow more flow to penetrate the sphere, and may thus transport salt within it. Eventually, this advective transport may even dominate the diffusive transport for large Da. The simulations show an initially linear decrease of the settling time with increasing Da. As Da increases further, this effect levels off as advection dominates salt transport within the sphere. We quantify the reduction of the delay due to non-zero Darcy number as

$$t_{\mathrm{sim}}(\mathrm{Da}) \approx t_{\mathrm{ref}}(\mathrm{Da}) + \frac{400}{1 + 1700\mathrm{Da}^{1.18}} \tag{3.22}$$

We note, however, that for the continuum hypothesis to be applicable to the porous medium, and so for our representation of flow within the particle to be relevant, we must have $\mathrm{Da} \leq 0.01$.

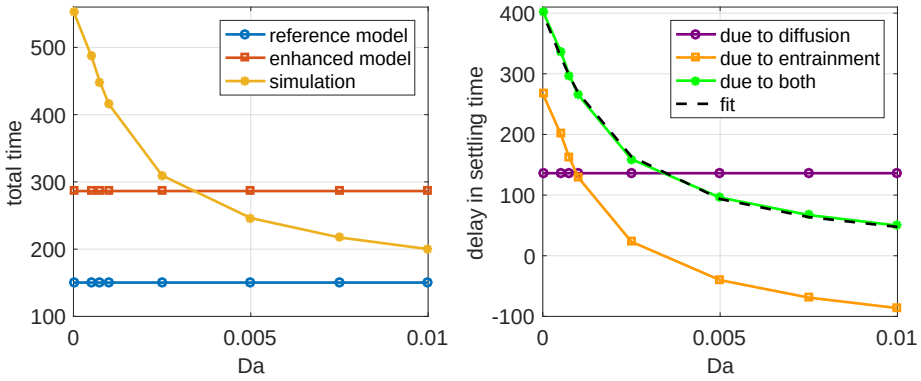

Figure 3.15: Left: Time required to settle a distance of 100 radii across a density gradient for several Darcy numbers Da. The reference time t_{ref} (blue) was computed using equation (3.17), the enhanced model time t_{enh} (red) using equation (3.19), and the simulation time t_{sim} (yellow) using our full numerical simulations. Right: Delay in settling time due to diffusion within the particle ($t_{\mathrm{enh}} - t_{\mathrm{ref}}$, purple), diffusion within the entrained fluid ($t_{\mathrm{sim}} - t_{\mathrm{enh}}$, orange), and both ($t_{\mathrm{sim}} - t_{\mathrm{ref}}$, green). The fit of equation (3.22) is shown as a dashed black line.

The parameter $\xi = \frac{\rho_l - \rho_u}{(\rho_s - \rho_u)(1-\phi)}$ captures the importance of diffusive effects in determining the buoyancy of the porous sphere. As can be seen in Figure 3.16, the two models and the simulations yield settling times that are similar when $\xi \leq 1$, as diffusion then plays only a minor role. As ξ increases, the delay due to diffusion within the sphere increases, as does the delay due to diffusion within the entrained fluid. Within the range of ξ considered, we find that the delay relative to the reference model grows linearly with ξ. Including the consideration that there is no delay in the limit $\xi \to 0$, we find that our data is well approximated by

$$t_{\mathrm{sim}}(\xi) \approx t_{\mathrm{ref}}(\xi) + 185\xi. \tag{3.23}$$

For naturally occurring values of the governing parameters, we therefore expect ξ and Pe to be the most determinant parameters in the total settling time of a porous particle.

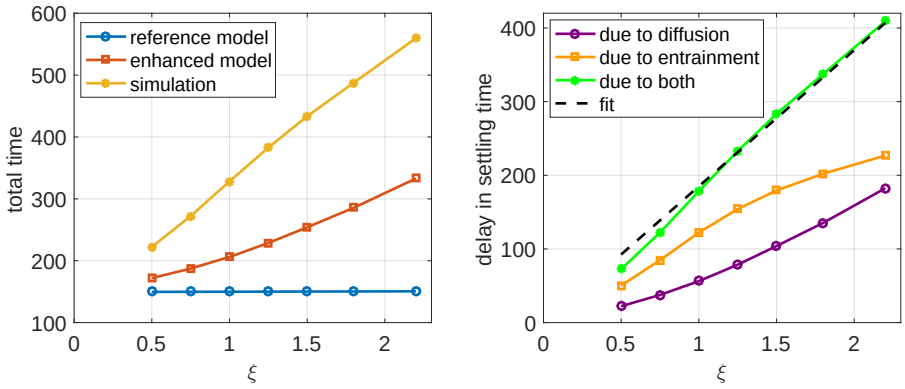

Figure 3.16: Left: Time required to settle a distance of 100 radii across a density gradient for several values of $\xi = \frac{\rho_l - \rho_u}{(\rho_s - \rho_u)(1-\phi)}$. The reference time t_{ref} (blue) was computed using equation (3.17), the enhanced model time t_{enh} (red) using equation (3.19), and the simulation time t_{sim} (yellow) using our full numerical simulations. Right: Delay in settling time due to diffusion within the particle ($t_{\text{enh}} - t_{\text{ref}}$, purple), diffusion within the entrained fluid ($t_{\text{sim}} - t_{\text{enh}}$, orange), and both ($t_{\text{sim}} - t_{\text{ref}}$, green). The fit of equation (3.23) is shown as a dashed black line.

Finally, we present the effects of varying the Reynolds number on the non-dimensional settling time in Figure 3.17. The Reynolds number influences several aspects of the flow. First, a larger Re corresponds to smaller non-dimensional settling speed, and thus all three computed times increase with Re. The additional settling time due to diffusion within the sphere is found to be nearly independent of Re, as it does not affect internal diffusive processes. Larger Reynolds numbers correspond to less entrained fluid, thus reducing total diffusion time. Moreover, as Re increases, the flow within the porous sphere increases, and so does transport of salt into the sphere. The overall settling delay thus shows a modest decrease with increasing Re, though it remains nearly constant for the diffusion induced delay, shown in purple in Figure 3.17 (right). We quantify this effect as

$$t_{\text{sim}}(\text{Re}) \approx t_{\text{ref}}(\text{Re}) + \frac{356}{1 + 0.026\text{Re}^{0.5}}. \tag{3.24}$$

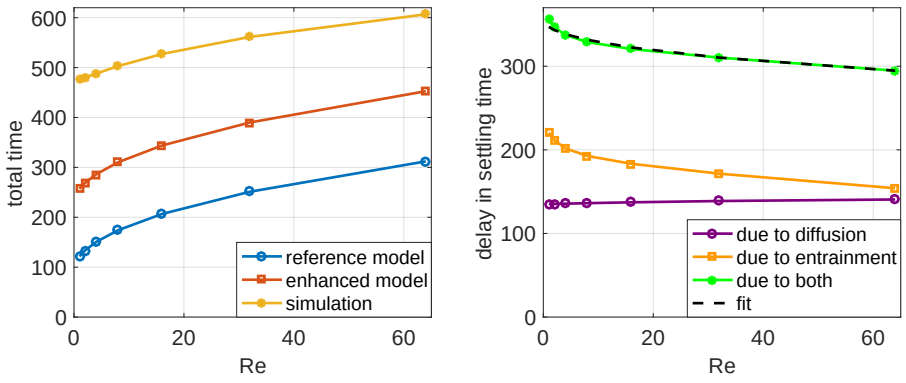

Figure 3.17: Left: Time required to settle a distance of 100 radii across a density gradient for several Reynolds numbers Re. The reference time t_{ref} (blue) was computed using equation (3.17), the enhanced model time t_{enh} (red) using equation (3.19), and the simulation time t_{sim} (yellow) using our full numerical simulations. Right: Delay in settling time due to diffusion within the particle ($t_{\mathrm{enh}} - t_{\mathrm{ref}}$, purple), diffusion within the entrained fluid ($t_{\mathrm{sim}} - t_{\mathrm{enh}}$, orange), and both ($t_{\mathrm{sim}} - t_{\mathrm{ref}}$, green). The fit of equation (3.24) is shown as a dashed black line.

3.6 Summary

We presented in this study numerical simulations of the settling of a porous sphere in a two-layer stratified ambient fluid. Prior work focused on the effects of diffusion within the particle, but did not quantify the effects of diffusion through the entrained fluid. The simulations presented here include fluid motion and diffusion through the entrained fluid to give a more complete picture of the settling dynamics. We focused on quantifying the effects of entrained fluid in combination with those of diffusion to provide a comprehensive picture of the settling of porous particles. We identified the dominant parameter $\xi = \frac{\rho_l - \rho_u}{(\rho_s - \rho_u)(1-\phi)}$, capturing the importance of diffusive effects on total settling time. We compared simulated settling time to the prediction of a simple reference model that assumes constant excess density of the particle. We quantified the effects of ξ, as well as those of the Reynolds, Péclet, and Darcy numbers. In addition to ξ, we found that Pe was the second most determinant parameter in the system, showing a logarithmic growth of the settling time, which over small intervals appears consistent with previous results showing a quadratic dependence of the settling time on particle size [16]. For relatively large Darcy numbers, the settling was significantly accelerated. However, most realistic values of Da are rather small, with $\mathrm{Da} < 10^{-4}$, and thus have a weaker impact on the total settling time. The effects of the Reynolds number were mostly well captured by our simple reference model which includes a Reynolds number-dependent drag coefficient. We considered also the settling time dependence on the density transition thickness γ, and found that the total settling time was not affected by the exact transition layer thickness if it exceeded approximately 30 times the particle radius. We thus provided a qualitative and quantitative picture of all the dominant parameters affecting the settling time of marine snow.

Chapter 4

New numerical method for fluid-porous domains

4.1 Introduction

In many natural settings and industrial applications, fluid flows in an environment partially consisting of porous medium. Examples where this setup occurs include rivers and oceans flowing over sandy deposits [23, 63–65], oil reservoirs and groundwater flow [66], flow past porous scaffolds in bioreactors [67] and blood clot formation in an artery [68–70]. In particular, the chemical pollution of our water resources through contaminated deposits is a significant issue [71], which requires models that can predict and quantify the spread of chemicals removed from contaminated soil by rainfall and flooding [72]. For most geometries, only numerical solutions are available. We present here a numerical method to simulate a system consisting of porous media and homogenous fluid separated by a sharp interface. This method is simple to implement and allows for a mobile interface between the porous and fluid regions.

The interaction of a freely flowing fluid with a porous matrix is complex and considerable effort has been dedicated to determine proper treatment of the interface between the two media. One of the early studies of the fluid-porous boundary condition was done by Beavers and Joseph in 1967 [73], where a semi-empirical slip velocity corresponding to a velocity jump was introduced to match the Navier-Stokes equations with a porous flow described by Darcy's law. Neale and Nader [74] used the Brinkman equations to describe the porous flow, and assumed continuous stress and velocity across the interface. The use of the Brinkman's equations and its associated effective viscosity, has been used by numerous authors [75–77] since it allows for more accurate matching at the interface. Vafai and Kim presented an exact analytical solution for fluid flow at the interface by matching both velocity and stress [78]. A more detailed volume-averaging study led by Ochoa-Tapia & Whitaker [79] deduced a condition of tangential stress jump at the interface which has since been widely accepted and used in many applications [26, 80, 81]. We will therefore make use of the Brinkman equations to describe the flow in the porous medium, and of a tangential stress jump boundary condition at the interface, for more accurate results.

Fluid-porous problems are typically solved either using a two-domain approach [77, 82], or a single-domain approach [83, 84]. In a two-domain approach, two sets of coupled governing equations are applied to the fluid and porous regions of the domain and matching boundary conditions are

enforced at the interface. This approach is more complicated to implement but provides means to apply a broad range of boundary conditions at the fluid-porous interface [85]. In a single-domain approach the entire domain is represented by one governing equation with variables undergoing a spatial variation across the interface [86]. This formulation avoids the explicit matching of boundary conditions at the fluid-porous interface and hence is widely used in numerical simulations of thermal natural convection [87]. We will make use of this approach to apply a tangential stress-jump boundary condition at the fluid-porous interface.

Various numerical methods have been used to solve the equations governing flow in fluid-porous domains. Because of the complex geometries associated with porous media, finite elements have been widely used [26, 80, 81, 88] as have finite volumes [85]. However many of these approaches rely on a fixed boundary between the two media. Our proposed method is based on finite-difference approximations of derivatives and accurately describes the flow in both media while allowing for a moving interface between the two sub-domains. The potentially mobile interface is defined by Lagrangian markers, whose position is governed by a simple differential equation. The stress-jump boundary condition is applied through a forcing term along the interface without requiring any matching. This approach is analogous to the immersed boundary method [89] and related methods used in multiphase flow [55–57]. There, a stress jump is imposed across a fluid-fluid interface, and the Navier-Stokes equations are solved on both sides of the interface with different parameters. Here, we employ a similar approach, but solve the Brinkman equations on one side of the interface, and the Navier-Stokes equations on the other. The immersed boundary method is often implemented using numerical delta functions to capture the interfacial forcing while in multiphase fluid flow a Volume-Of-Fluid method is often used, which corresponds to an interface that is one grid-cell thick. Here, we will compare both implementations.

After validating our method, we proceed to use it to describe the motion of fluid and particles in erosive systems where the geometry of the surface over which currents propagate may undergo a continuous change. At present, a complete understanding of resuspension of particles from an irregular bed of particles remains elusive. Direct numerical simulations have been employed to study the lift-off of particles in plane Poiseuille flow [65], but such simulations are constrained to a limited number of circular particles [90]. In contrast, the continuum approach used here may describe much larger systems. Our fluid-porous solver can also be used as part of a larger fluid solver to locally quantify suspension of particles and predicting changes in surface geometry. Suspended particles representing different type of contaminants, viruses or bacteria, could also easily be traced by adding an advection-diffusion equation and tracking concentration fields [91].

In this chapter, we first present the governing equations. Our model and numerical approach are described later and validated. We discuss our results and consider erosion applications with fixed and moving interfaces.

4.2 Equations of fluid-porous domains

We consider an incompressible Newtonian fluid flowing over a fixed porous medium with potentially variable permeability, see figure 4.1. We make use of the continuum approach, as opposed to a model tracking individual particles, to allow for simulations over domains encompassing more particles. The homogenous fluid portion of the system is governed by the incompressible Navier-Stokes equations

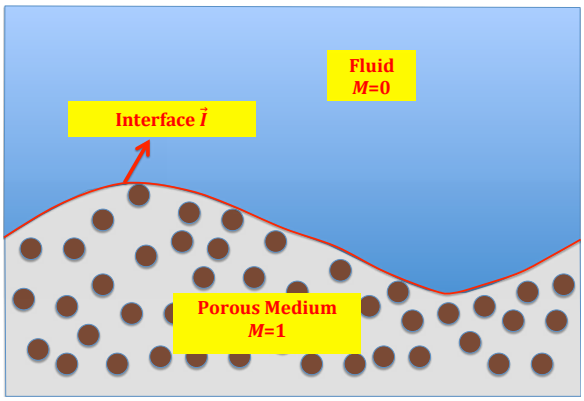

Figure 4.1: Schematics of the domain under consideration. The porous medium (below) and homogenous fluid (above) are separated by a sharp interface $\vec{I}$. Flow in the fluid portion is described by the Navier-Stokes equations, and flow within the porous medium is described by the Brinkman equations.

The equations used to describe the flow within porous media typically depends on the specific flow characteristics such as the local Reynolds number, porosity, and accuracy level desired in the vicinity of the boundaries. We assume here a stationary porous matrix, saturated by a fluid flowing with a locally low Reynolds number. Under these conditions, the flow adjusts instantaneously to changes in the boundary conditions and is well described by the Brinkman equations [26]

We note that the Brinkman equations are of second order in space, like the Navier-Stokes equations, which will facilitate matching at the interface, $\vec{I}$, separating the two sub-domains.

For configurations containing both fluid and porous medium, boundary conditions have been derived to match flow quantities at the interface between the two sub-domains. We enforce the commonly used boundary condition of continuous velocities and a tangential stress jump [79] across the interface $\vec{I}$, which result from balancing mass, momentum and energy [77]. So at the interface we have:

$$\vec{u}_p = \vec{u}_f = \vec{u}_{\vec{I}} \tag{4.1}$$

$$\vec{n} \cdot (\bar{\bar{T}}_f - \bar{\bar{T}}_p) \cdot \vec{t} = \frac{\zeta \mu}{\sqrt{K}} \vec{u}_{\vec{I}} \cdot \vec{t}, \tag{4.2}$$

where $\bar{\bar{T}}_f = -p\bar{\bar{I}} + \mu(\nabla\vec{u} + (\nabla\vec{u})^T)$ is the fluid stress tensor, $\bar{\bar{T}}_p = -p\bar{\bar{I}} + \mu_e(\nabla\vec{u} + (\nabla\vec{u})^T)$ is the stress tensor in the porous domain, μ_e is the effective viscosity inside the porous medium, $\vec{u}$ the fluid velocity vector, $\vec{t}$ and $\vec{n}$ are, respectively, unit tangential and normal vectors to the interface, ζ is an empirical constant of order 1 and $K = ||\bar{\bar{\kappa}}||$ is the magnitude of the permeability tensor.

To model both the fluid and porous regions, we adopt here a single domain approach using a convex combination of the Brinkman and Navier-Stokes equations. To distinguish between the two domains, we use an indicating function M, which is set to 0 in the homogenous fluid and to 1 in the porous medium, as shown in figure 4.1. Rather than solving separately the governing equations in both domains and matching them using (4.2), we impose the stress jump boundary condition by the addition of an interfacial force, $\vec{f}_{\vec{I}}$, as is commonly done in multiphase flow [55, 56, 89]. More precisely, we introduce a force along the interface, which originates from the divergence of the stress jump

$$\vec{f}_{\vec{I}} = \delta_{\vec{I}} \left(\zeta \frac{\mu}{\sqrt{K}} \vec{u} \cdot \vec{t} \right) \vec{t}. \tag{4.3}$$

Here $\delta_{\vec{I}}$ is a one-dimensional delta function which indicates that the force is only non-zero along the interface. This allows for an efficient and flexible numerical approach that can be used to determine flow characteristics in partially porous domains.

We proceed to non-dimensionalize the equations given above using quantities describing the fluid system. We use a typical fluid density, ρ, and velocity scale U. We also use a length scale L relevant to the fluid flow (for example for the pipe flow validation L is the diameter of the pipe). The pressure p is non-dimensionalized by the dynamic pressure ρU^2. This results in two non-dimensional numbers. The Reynolds number $Re = \rho UL/\mu$ describes the ratio of inertial to viscous effects in the fluid. The Darcy number, $Da = K/L^2$, is the ratio of the typical length over which flow variations are observed in the porous medium to the length scale of the fluid flow, squared. The value of Da is typically smaller than 10^{-3}, which indicates that the flow in the porous medium is averaged over several pores. In addition, the viscosity ratio $\beta = \mu/\mu_e$ also appears in the non-dimensional porous stress tensor. In this study, we will proceed to set $\beta = 1$ for simplicity.

Since the non-dimensionalization was done using reference quantities in the fluid domain, the Reynolds number above does not describe the importance of inertial effects in the porous medium. We can, however, compute a porous Reynolds number as

$$Re_p = \frac{\rho U_p L_p}{\mu_e} = \beta \; Da \; Re \tag{4.4}$$

where $L_p \sim \sqrt{K} = \sqrt{Da}\; L$ and $U_p \sim \frac{L_p}{L} U = \sqrt{Da}\; U$ are typical length and velocity scales of the flow in the porous medium. We will restrict our attentions to systems where $Re_p \leq 1$ warranting the use of Brinkman equations in the porous medium.

The resulting non-dimensional convex combination of Navier-Stokes and Brinkman equations, including the interfacial forcing term is then,

$$\begin{aligned} \nabla \cdot \vec{u} &= 0 \qquad (4.5) \\ M\Big[\frac{1}{Da \cdot Re}\vec{u}\Big] + (1-M)\Big[\frac{\partial \vec{u}}{\partial t} + \vec{u} \cdot \nabla \vec{u}\Big] &= M\nabla \cdot \bar{\bar{T}}_p + (1-M)\nabla \cdot \bar{\bar{T}}_f + \vec{f} + \vec{f}_{\vec{I}} \end{aligned}$$

where we now use $\vec{u}$ to denote a non-dimensional velocity, and the non-dimensional stress tensors are

$$\bar{\bar{T}}_f = -p\bar{I} + \frac{1}{Re}(\nabla \vec{u} + (\nabla \vec{u})^T) \quad \text{and} \tag{4.6}$$

$$\bar{\bar{T}}_p = -p\bar{I} + \frac{1}{\beta Re}(\nabla \vec{u} + (\nabla \vec{u})^T). \tag{4.7}$$

As boundary conditions at the edge of the domain, we prescribe the fluid velocity $\vec{u}$, and impose $\frac{\partial p}{\partial n} = 0$ at the top and bottom boundaries. In the horizontal direction the flow is assumed periodic. Although we focus here on a two-dimensional system, the formulation is identical in three dimensions.

While we do not move the interface between the two media in this paper, one could easily do so provided that the flux, F, of particulates leaving the porous medium and entering the fluid is known. In cases where this flux normalized with the particle settling speed U_s is non-zero, it will cause the interface $\vec{I}$ to deform according to

$$\frac{\partial \vec{I}}{\partial t} = -F \; U_s \; \vec{n}.$$

We discuss in section 4 how such a flux may be computed.

4.3 Combined solver

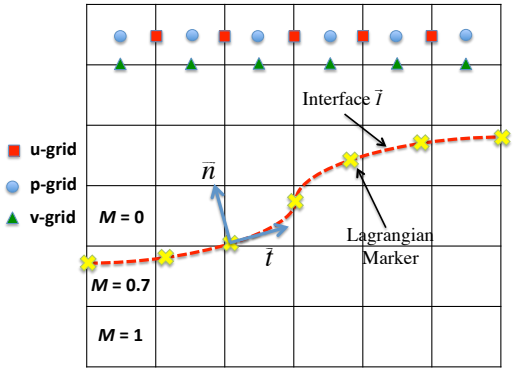

Figure 4.2: In this figure the dashed red line represents the border between porous medium and unimpeded flow. The potentially mobile interface is constructed by Lagrangian markers connected by cubic splines capable to resume any shape.

We solve equations (4.5) numerically in a two-dimensional domain. We discretize the spatial derivatives using centered differences on a Marker-and-Cell (MAC) grid. The grid is fixed and uniform for simplicity, though our method is conducive to adaptive-grid-refinement. The interface separating the porous medium from the homogenous fluid is a curve tracked with Lagrangian markers connected by cubic splines [55]. This allows for a smooth interface that may easily accommodate a variety of interfacial geometries. We place the markers at approximately equal distance along the curve of the interface. We compute the indicating function M based on the location of the interface and its intersections with the MAC grid. This value is always between 0 and 1, see figure 4.2, and describes the volumetric average of the Navier-Stokes and Brinkman equations.

To ensure stability with reasonable time steps, we use an implicit scheme for the diffusive terms, as shown in more details below. Explicit methods may also be used, but would have greater time step constraints. Both the implicit Crank-Nicholson and time independent Brinkman terms require an additional linear system to be solved, although in practice it is not as computationally demanding as the linear system used to solve for the pressure. This latter term is found using a well-established projection method [82]. At the top and bottom of our domain, a Neumann boundary condition is used for pressure p, while in the horizontal direction we use the periodicity of the system. Our method can be described in three major steps.

1. We begin by ignoring the pressure term and update the velocity $\vec{u}^*$, using a second order Adams-Bashforth method for the convective terms, and Crank-Nicholson for the diffusive terms, yielding a first, sparse, linear system:

$$\Big(M\Delta t\big[\frac{1}{Da\cdot Re}-\frac{1}{Re}\nabla^2\big]+(1-M)\big[\bar{\bar{I}}-\frac{\Delta t}{2Re}\nabla^2\big]\Big)\vec{u}^*= \tag{4.8}$$
$$(1-M)\vec{u}^n+\frac{\Delta t}{2}\Big(3\big[\vec{f}+\vec{f}_I+(1-M)[-\vec{u}\cdot\nabla\vec{u}\big]^n-$$
$$\big[\vec{f}+\vec{f}_I+(1-M)[-\vec{u}\cdot\nabla\vec{u}\big]^{n-1}+(1-M)\frac{1}{Re}\nabla^2\vec{u}^n\Big).$$

2. By imposing that the velocity must be divergence-free, we obtain a Poisson equation for the pressure, which results in a second linear system after discretization

$$\nabla \cdot A^{-1} \cdot \nabla p^{n+1} \Delta t = \nabla \cdot \vec{u}^*, \tag{4.9}$$

$$A = M\Delta t\big[\frac{1}{Da \cdot Re} - \frac{1}{Re}\nabla^2\big] + (1-M)\big[\bar{\bar{I}} - \frac{\Delta t}{2Re}\nabla^2\big]. \tag{4.10}$$

Although A is a sparse Matrix, A^{-1} is not, nor is it symmetric or positive definite. This results in limitations for larger systems or when memory is a limited resource. For smaller problems, a direct method is preferred while larger problems require an iterative approach [92]. The fastest convergence for our iterative solver was achieved using the Biconjugate Gradient Stabilized Method [93].

3. Finally, the velocity field at each grid point is obtained by adding the pressure correction term to the updated velocity.

$$A\vec{u}^{n+1} = A\vec{u}^* - \nabla p^{n+1} \Delta t \tag{4.11}$$

Because of our one-domain approach, the numerical process of time integration is computationally more expensive than for that of a pure fluid, as the matrix A is more complicated here than for a pure fluid, where it would be a diagonal matrix. Although most of the results obtained here were retrieved using a serial code, we have verified that this approach may also be implemented in parallel, for both implicit and explicit methods.

4.3.1 Line-integral method

There are two main strategies to implement the interface force, see equation (4.3), used to enforce the stress-jump condition denoted as "line-integral" and "delta-force" methods.

First, in what we refer to as the "line-inegral" method [55], the force is averaged over each grid cell using a double integral. The resulting average interfacial force over grid cell (i, j) can be expressed as

$$\vec{f}_{I_{ij}} = \frac{\iint_{D_{ij}} \vec{f}_I dxdy}{\Delta x \Delta y} = \frac{\int_{C_{ij}} \zeta \frac{\mu}{\sqrt{K}} (\vec{u} \cdot \vec{t})\, \vec{t}\, ds}{\Delta x \Delta y}. \tag{4.12}$$

The strategy for calculating the interface force numerically is:

1. Loop over grid cells and find the ones intersecting the interface.
2. Record where the interface enters and exits those cells.
3. Introduce along the interface inside each recorded cell n points to use in our numerical integration.
4. Evaluate at each point, the s-value (arc length), velocity vector $\vec{u}$ and the tangent vector $\vec{t}$.
5. Evaluate the interfacial force using equation 4.12.

4.3.2 Delta-force method

An alternative approach, which we refer to as the "delta-force" method, [89] distributes the interface force $\vec{f}_I$ to the closest neighboring grid points using a discretized delta function $\delta_{h_{ij}}$. In our

simulations this delta function has full strength right at the interface and decays to zero within 2 neighboring cells.

$$\vec{f}_{I_{ij}} = \frac{\sum_m \delta_{h_{ij}}(\vec{f}_{I_m})}{\Delta x \Delta y} \tag{4.13}$$

The strategy is:

1. Loop over all markers and store the grid indices for each marker.
2. Divide the interface into m sections with m the number of markers.
3. Evaluate the s-value (arc-length from the beginning of the interface) associated with the beginning and end of each section.
4. Divide each section into n equidistant points. At each point $\vec{u}$ and $\vec{t}$ are evaluated to compute $\vec{f}_{I_m}$.
5. Use a delta function $\delta_{h_{ij}}(\vec{f}_{I_m})$ to spread the force into neighboring grid points within 2 cells from the marker.
6. Evaluate the interfacial force using equation 4.13.

4.4 Validation of the combined solver

We validate our combined fluid-porous solver by focusing initially on the individual components. The heat equation or the viscous part of the Navier-Stokes is validated first. Second, we validate the full Navier-Stokes equations using presribed forcing terms. Third, the Brinkman equations are validated in a similar manner. Last, our combined solver is validated by using the analytical solution to a pipe flow and drag convergence for a porous cylinder. Each validation is explained separately in its own subsection.

4.4.1 Heat equation

We solve the heat equation problem in 4.14 using our numerical solver and compare our results with the analytical solution 4.17. We apply periodic boundary conditions in x-direction and Dirichlet in y.

$$u_t = \mu(u_{xx} + u_{yy}) \tag{4.14}$$

Boundary Conditions: (4.15)

$$\begin{aligned} u(0,y,t) &= u(1,y,t) \\ u(x,0,t) &= 1 \\ u(x,1,t) &= 1 \end{aligned}$$

Initial Conditions: (4.16)

$$u(x,y,t=0) = \sin(\pi y)\cos(2\pi x) + 1$$

The exact solution to the BVP 4.14 is

$$u(x,y,t) = e^{-5\pi^2 \mu t}\sin(\pi y)\cos(2\pi x) + 1. \tag{4.17}$$

We validate the convergence of the numerical solution by comparing it to the exact solution, see figure 4.3. The rate of convergence is second order in both time and space. The numerical solution is denoted U, the exact solution u and the absolute error $|u - U|$.

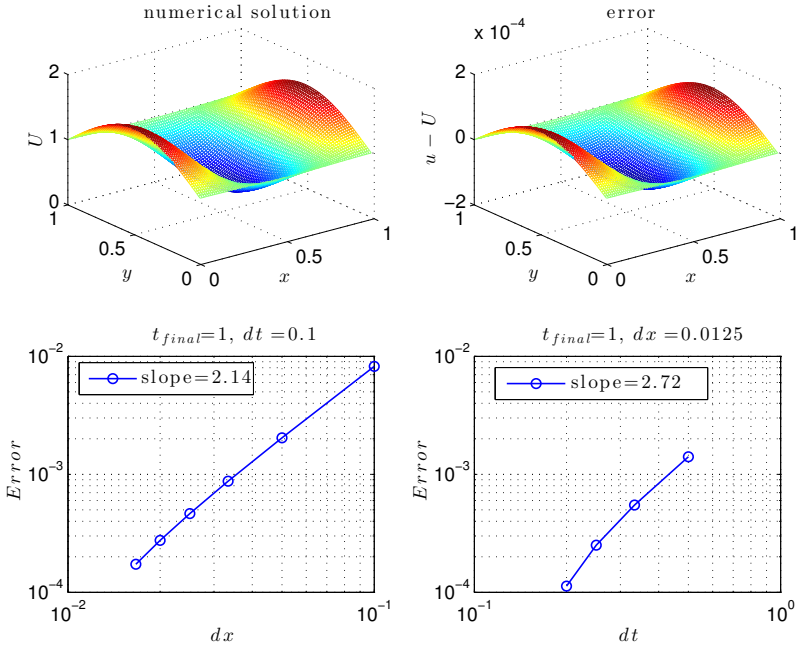

Figure 4.3: Heat equation problem is solved numerically and compared with an exact analytical solution. We obtain second order convergence in time and space.

Next, we solve the poisson equation numerically and compare our results with the exact solution. The result is shown in figure 4.4. The convergence is second order in space as expected.

Differential Equation: (4.18)

$$\begin{aligned} p_{xx} + p_{yy} &= -5\pi^2 \cos(2\pi x)\cos(\pi y) \\ & x: \ 0 \le x \le 1 \\ & y: \ 0 \le y \le 1 \end{aligned}$$

Boundary Conditions: (4.19)

$$\begin{aligned} & p(x=0,y) = p(x=1,y) \\ & p_y(x,y=0) = p_y(x,y=1) = 0 \end{aligned}$$

Exact Solution: (4.20)

$$p(x,y) = \cos(2\pi x)\cos(\pi y)$$

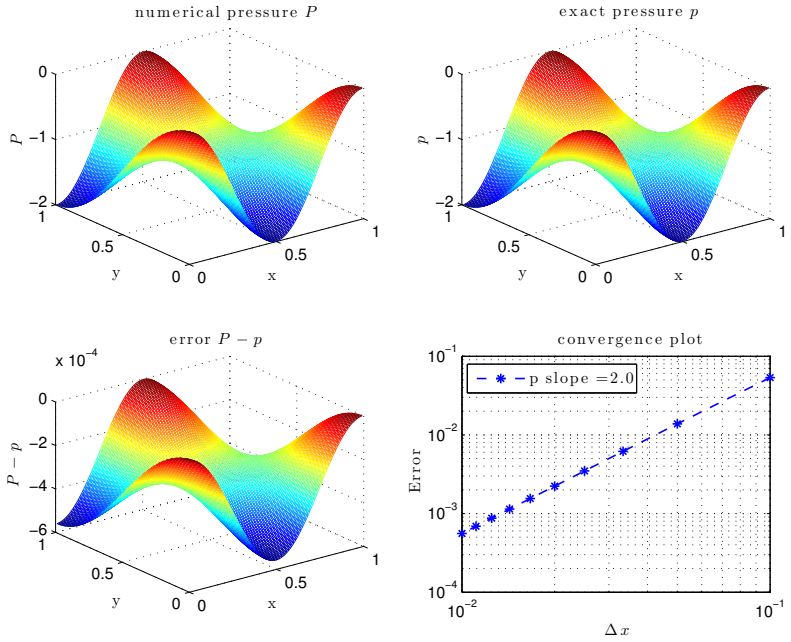

Figure 4.4: Poisson problem is solved numerically and compared with an exact analytical solution. We obtain second order convergence.

4.4.2 Navier-Stokes

We apply the projection method to the Navier-Stokes equations and obtain a numerical solution. We solve equation 4.8, with $M = 0$ over the entire domain. The steps of the projection method are outlined in the appendix. We use central difference approximations on a MAC grid for our spatial derivatives and a combination of Adams-Bashforth2 and Crank-Nicolson for our time integration. f_1 and f_2 are the horizontal and vertical components of the force $\vec{f}$. We apply periodic boundary

condition in the x direction and in the y direction, Neumann for pressure, and Dirichlet for velocity.

Differential Equation: (4.21)

$$\begin{aligned}
\frac{\partial \vec{u}}{\partial t} &= -\vec{u}\cdot\nabla\vec{u} + \vec{f} + \frac{1}{Re}\nabla^2\vec{u} - \nabla p \\
f_1 &= -2\pi\sin(2\pi x)\cos(\pi y) - \Big[(\alpha + 20\frac{\pi^2}{Re})\sin(2\pi x)\sin(4\pi y)\Big]e^{\alpha t} \\
&+ \pi\sin(4\pi x)\Big[\sin^2(4\pi y) - 2\sin^2(2\pi y)\cos(4\pi y)\Big]e^{2\alpha t} \\
f_2 &= -\pi\cos(2\pi x)\sin(\pi y) + \Big[\cos(2\pi x)\Big(2\frac{\pi^2}{Re} + \alpha\sin^2(2\pi y) - 10\frac{\pi^2}{Re}\cos(4\pi y)\Big)\Big]e^{\alpha t} \\
&+ \Big[\pi\sin(4\pi y) - \pi/2\sin(8\pi y)\Big]e^{2\alpha t}
\end{aligned}$$

Boundary Conditions: (4.22)

$$\begin{aligned}
u(0,y,t) &= u(1,y,t) \\
u(x,0,t) &= 0 \\
u(x,1,t) &= 0 \\
v(0,y,t) &= v(1,y) \\
v(x,0,t) &= 0 \\
v(x,1,t) &= 0 \\
p(0,y,t) &= p(1,y) \\
p_y(x,0,t) &= 0 \\
p_y(x,1,t) &= 0
\end{aligned}$$

Initial Conditions: (4.23)

$$\begin{aligned}
u(x,y,0) &= -\sin(2\pi x)\sin(4\pi y) \\
v(x,y,0) &= \cos(2\pi x)\sin^2(2\pi y) \\
p(x,y,0) &= \cos(2\pi x)\cos(\pi y)
\end{aligned}$$

Exact Solution: (4.24)

$$\begin{aligned}
u(x,y,t) &= -\sin(2\pi x)\sin(4\pi y)e^{\alpha t} \\
v(x,y,t) &= \cos(2\pi x)\sin^2(2\pi y)e^{\alpha t} \\
p(x,y,t) &= \cos(2\pi x)\cos(\pi y)e^{\alpha t}
\end{aligned}$$

The force is non-linear and tailor-made with the objective to attain an analytical solution. The numerical solution converges to the exact solution as depicted in figure 4.5. The convergence is second order in time and space in accordance to the theory. The domain size is 1×1 and the parameters used are $\alpha = -10$ and $Re = 10$.

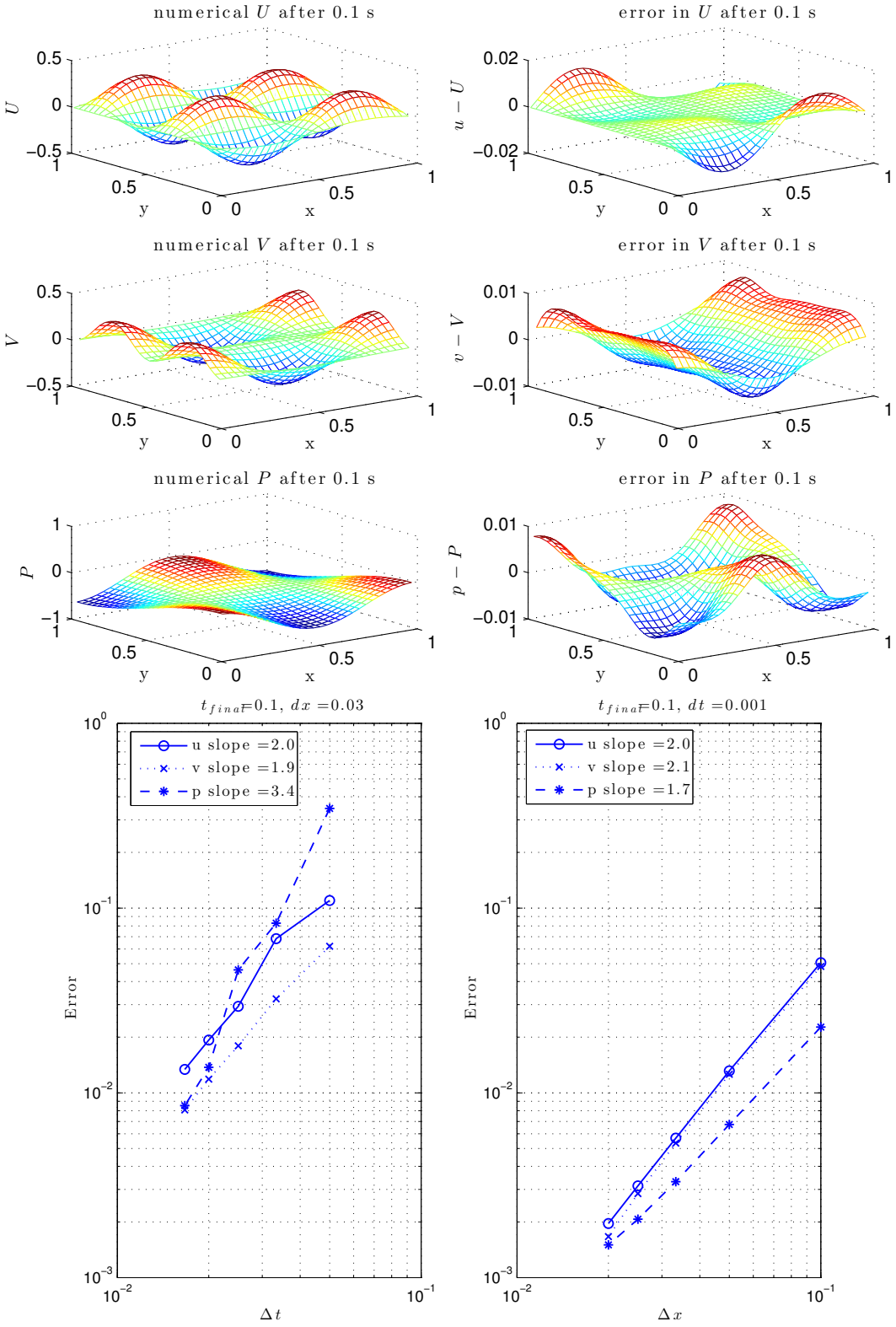

Figure 4.5: Navier-Stokes equations are solved numerically and compared with an exact analytical solution. We obtain second order convergence in both time and space.

4.4.3 Brinkman

We solve a Brinkman problem with known analytical solution using our numerical solver. This corresponds to solving equation 4.8 with $M = 1$ over the entire domain. f_1 and f_2 are as before the horizontal and vertical prescribed forces. The flow is periodic in the x direction. In the y direction, we apply Neumann for pressure and Dirichlet for velocity. The numerical solution and the error are plotted in figure 4.6. The convergence rate is second order for both velocity and pressure.

Differential Equation: (4.25)

$$\begin{aligned}
\frac{1}{Da \cdot Re}\vec{u} &= \nabla \cdot -P\bar{I} + \frac{1}{\beta \cdot Re}\nabla^2\vec{u} + \vec{f} \\
f_1 &= -\Big(\frac{1}{Da\ Re} + \frac{20\pi^2}{\beta Re}\Big)\sin(2\pi x)\sin(4\pi y) - 2\pi\sin(2\pi x)\cos(\pi y) \\
f_2 &= \Big(\frac{1}{Da\ Re} + \frac{4\pi^2}{\beta Re}\Big)\cos(2\pi x)\sin^2(2\pi y) - \frac{8\pi^2}{\beta Re}\cos(2\pi x)\cos(4\pi y) \\
&+ \pi\cos(2\pi x)\sin(\pi y)
\end{aligned}$$

Boundary Conditions: (4.26)

$$\begin{aligned}
u(0,y) &= u(1,y) \\
u(x,0) &= 0 \\
u(x,1) &= 0 \\
v(0,y) &= v(1,y) \\
v(x,0) &= 0 \\
v(x,1) &= 0 \\
p(0,y) &= p(1,y) \\
p_y(x,0) &= 0 \\
p_y(x,1) &= 0
\end{aligned}$$

Exact Solution: (4.27)

$$\begin{aligned}
u(x,y,t) &= -\sin(2\pi x)\sin(4\pi y) \\
v(x,y,t) &= \cos(2\pi x)\sin^2(2\pi y) \\
p(x,y,t) &= \cos(2\pi x)\cos(\pi y) - 1
\end{aligned}$$

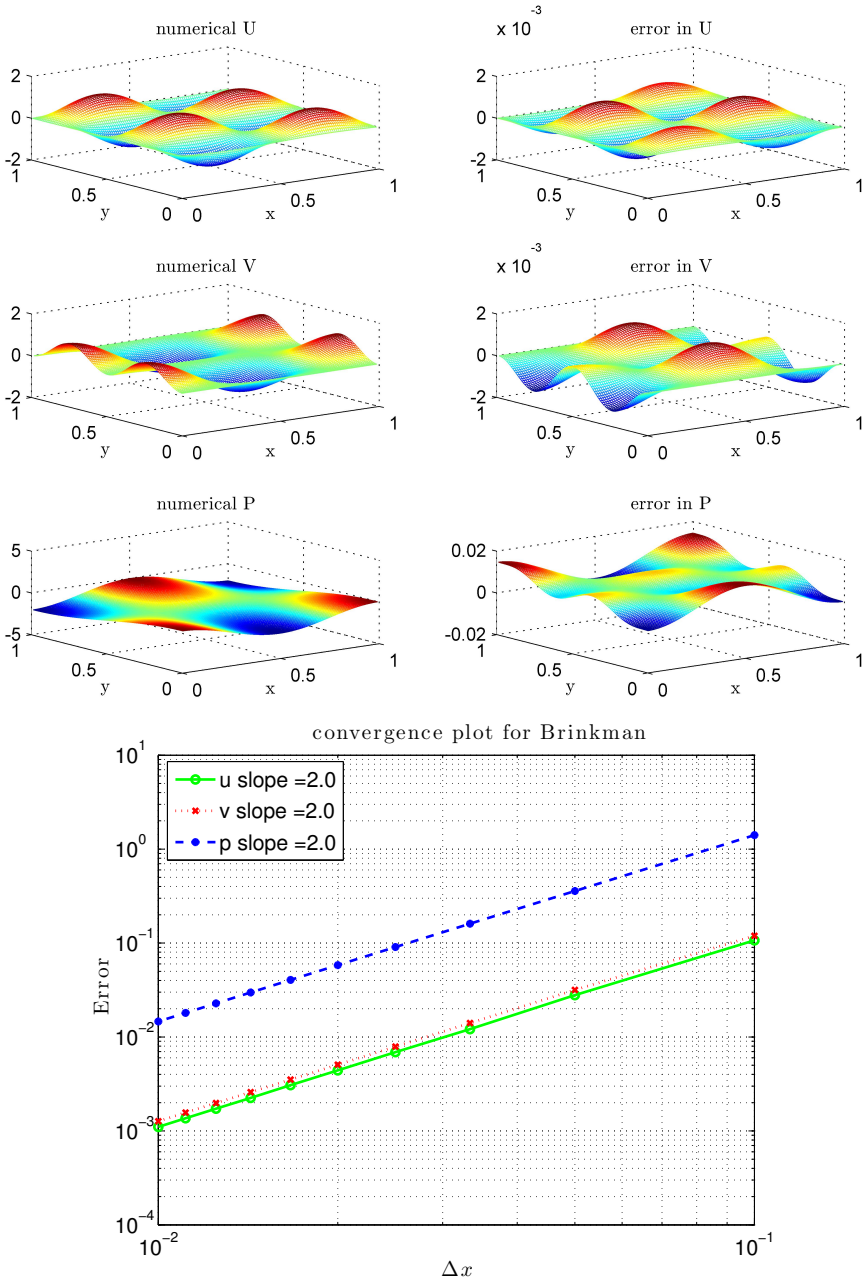

Figure 4.6: Brinkman equations are solved numerically and compared with an exact analytical solution. We obtain second order convergence.

4.4.4 Fluid-porous domains

We first validated our solver for the case of a homogeneous fluid. We obtained an analytical solution to the Navier-Stokes equations subject to a tailor-made sinusoidal force. As expected, we found second order convergence in both space and time. We then moved to consider a domain partially

made of a porous medium. We selected a standard two dimensional pipe flow with a fixed interface as depicted in figure 4.7, for which an analytical solution may be obtained.

We computed a transient solution for an infinite-size porous domain. However, for clarity, we present here the steady-state solution only. Details of the transient solution can be found in the Appendix. We consider an overlying fluid region of non-dimensional depth 1. Denoting the vertical coordinate with y, the velocities in the homogenous fluid and the porous medium are, respectively,

$$u_f = \frac{G\ Re}{2}(y-1)(y+\delta) \quad \text{and,} \tag{4.28}$$

$$u_p = \frac{G\ Re}{2}(2Da-\delta)e^{\sqrt{\frac{\beta}{Da}}y} - G\ Re\ Da \tag{4.29}$$

where $\delta = \frac{2Da+\sqrt{\beta Da}}{1+\sqrt{\beta Da}+\sqrt{\beta}\zeta}$ and $G = \frac{dP}{dx}$ is constant. The stress jump boundary condition affects only the value of δ, and has the most impact on the interface velocity at $y = 0$.

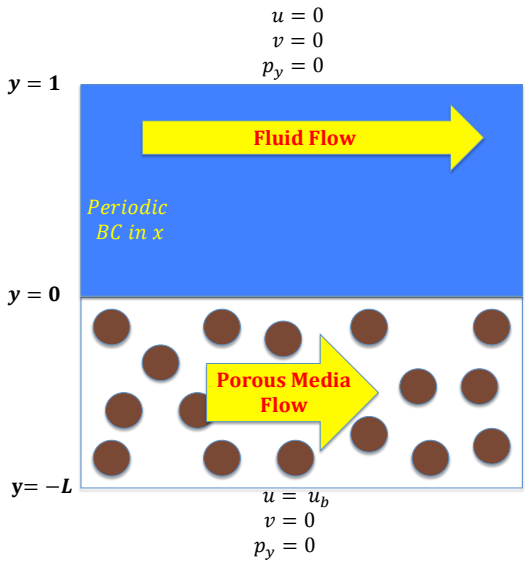

Figure 4.7: Pipe flow model used for validation of our porous-fluid solver. The driving force is a constant pressure gradient in the x direction ($\nabla p =< -G, 0 >$). The horizontal bottom boundary velocity u_b is set to the analytical velocity calculated at depth $y = -L$ by equation (4.29).

Simulation results for both methods are shown in figure 4.8 for $\zeta = 0.5, \zeta = 0$ and $\zeta = -0.5$.

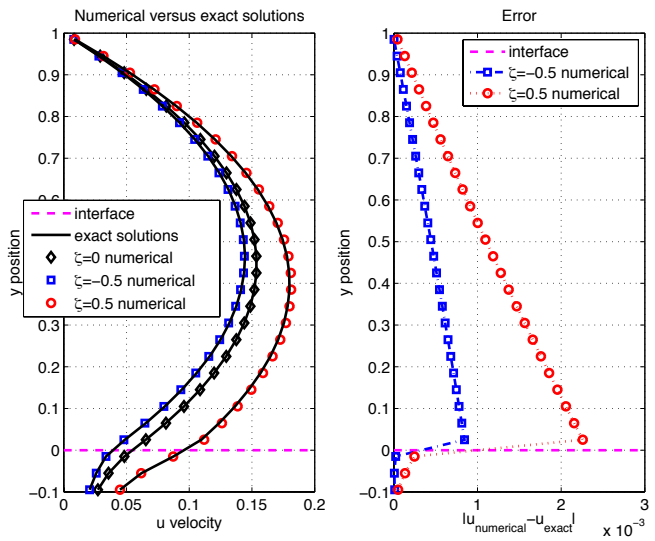

Figure 4.8: Analytical and numerical results for pipe flow with constant pressure gradient G at steady-state. The parameters used for these simulations are $Re = 1$, $Da = 0.01$, $dy = 0.01$, $dt = 0.01$ and $G = 1$. For clarity only the line-integral method is depicted as the numerical solution.

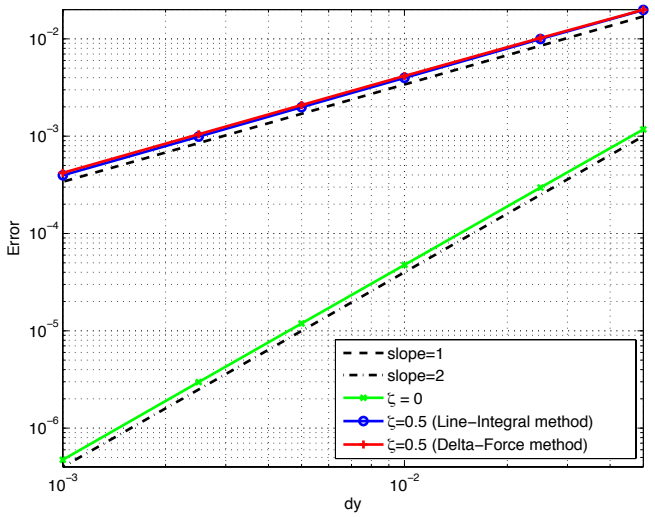

Figure 4.9: Convergence plot for pipe flow with constant pressure gradient. The error was computed where it was the largest and parameters used were $Re = 1$, $Da = 0.01$, $dt = 0.01$ and $L = 0.1$.

Negative ζ values tend to decelerate the flow and positive ζ values do the opposite. When $\zeta = 0$, there is no stress jump, and both methods are identical. We note that the largest error always occurs close to the interface, on the fluid side. The most critical location in applications is at the interface itself, so we present convergence plots based on the error for the interpolated velocity at the interface. The convergence is found to be of first order for $\zeta = 0.5$ and second order for $\zeta = 0$, as shown in figure 4.9. The non-zero ζ implies that the velocity gradient is not continuous across the interface, causing the convergence to be only first order for both approaches, though with different

coefficients. The specific location of the interface relative to the grid also affects the magnitude of the error, especially when the interface is parallel to the grid as is the case here.

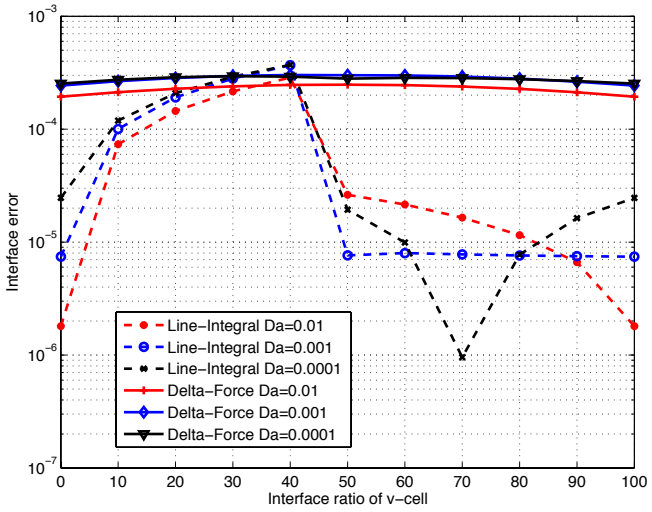

Figure 4.10: Error dependence on location of interface with respect to the grid. The parameters used in this simulation are $Re = 1$, $\zeta = 0.5$, $dy = 0.001$ and $dt = 0.01$. The error is calculated using the steady-state solution. The domain size is kept fixed while the interface is moved across the v-cell.

Figure 4.10 depicts a summary of results obtained for various interface positions relative to the grid. Here 0 or 100 percent interface ratio of v-cell means that the interfaces passes through the u grid-points, where it can be seen to yield the most accurate result. The convergence plot shown in figure 4.9 was obtained while the interface was located at 30% with respect to the v-cell, where both methods yield almost identical results. We see in figure 4.10 that the "delta-force" method is less sensitive to the interface position, presumably because it is more broadly distributed. On the other hand, in the "line-integral" method the forcing term is applied to a more focused area. The closer the interface is to the neighboring u grid-points, the more accurate the results are.

For all three Da numbers considered here, the "line-integral" method had a significantly lower error on average, and hence was found to be superior to the "delta-force" method for applications where velocity at the interface is important. We note that the error may change sign, and thus go lower than expected, as is the case for the "line-integral" method with $Da = 10^{-4}$ near an interface ratio of 70%. In light of these results, we will use the "line-integral" method throughout the remainder of this study, as it provides overall more accurate velocities at the interface.

4.4.5 Flow past a porous cylinder

In this section the flow past a porous cylinder will be studied in more detail. The objective is to validate the correctness of our method by comparing it to other similar numerical simulations. The velocity and pressure fields are solved inside and outside the porous cylinder and the drag convergence is verified using Oseen's equations.

The computational domain consists of a rectangular area with horizontal flow past a porous cylinder in the middle of the domain. Due to symmetry the simulation is performed only in the upper half of the domain, to lower the computational cost. Generally there are three main categories of boundary conditions for pipe flow, pressure driven flow, velocity driven flow or a hybrid of both types. In our simulations, the velocity driven boundary conditions were mostly used. Two different configurations are outlined in figures 4.11 and 4.12 with corresponding boundary conditions. Here u and v represent horizontal and vertical components of the velocity vector $\vec{u}$. We consider 2 configurations:

Configuration1, shown in figure 4.11, includes Dirichlet boundary condition for velocity and Neumann for pressure at inflow and Neumann boundary condition for velocity and Dirichlet for pressure at outflow. The symmetry line in the middle shown as a dashed line helps us to simulate half a domain size. We apply Neumann for horizontal velocity and pressure and assume no vertical flow. At the top and lower boundaries, we apply Dirichlet boundary conditon for velocity and Neumann for pressure.

Inlet: $\vec{u} = \vec{u}_0$ and $\frac{\partial p}{\partial x} = 0$, Outlet: $\frac{\partial \vec{u}}{\partial x} = 0$ and $p = 0$

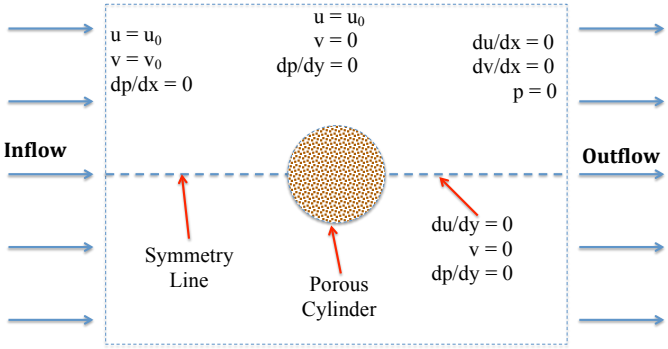

Figure 4.11: Porous cylinder in rectangular domain used for validation of solver. Neumann boundary condition is used for velocity at the output.

Configuration 2, shown in figure 4.12, includes Dirichlet boundary condition for velocity and Neumann boundary condition for pressure at inflow and outflow. Along the symmetry line, we apply Neumann for horizontal velocity and pressure and assume no vertical flow as before. At the top and lower boundaries, we apply Dirichlet boundary conditon for vertical velocity and Neumann for pressure and horizontal velocity.

Inlet: $\vec{u} = \vec{u}_0$ and $\frac{\partial p}{\partial x} = 0$, Outlet: $\vec{u} = \vec{u}_0$ and $\frac{\partial p}{\partial x} = 0$

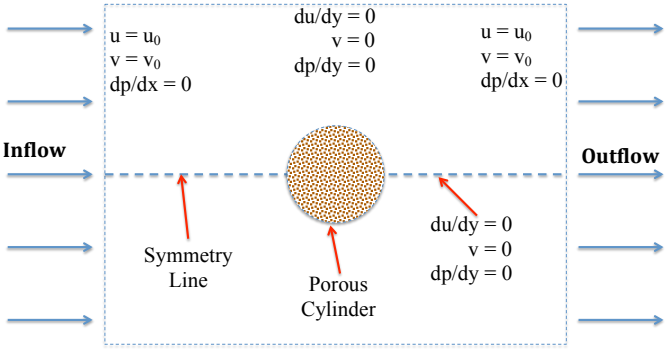

Figure 4.12: Porous cylinder in rectangular domain used for validation of solver. Dirichlet boundary condition is used for velocity at the output.

Both configurations can be used for drag calculations. For smaller domain sizes and lower Reynolds numbers, configuration 2 is preferred as it preserves the symmetry of the flow. Fluid drag calculation is critical in many applications. Here we will use it primarily for validation. The strategy for calculating the drag is outlined in six steps.

1. The neighboring grid points are located at each marker position on the cylinder.
2. The pressure p and the velocity gradients u_x and v_y are evaluated on neighboring p-grid points. The grid points for p, u and v are shown in figure 4.20.
3. The velocity gradients u_y and v_x are evaluated on neighboring cross points.
4. Bilinear interpolation is used to interpolate the pressure p and the velocity gradients at each marker position.
5. The stress tensor $\bar{\bar{T}}$ is evaluated at each marker position.

$$\bar{\bar{T}}_{ij} = -p_{ij}\bar{\bar{I}} + \mu(\frac{\partial u_i}{\partial x_j} + \frac{\partial u_j}{\partial x_i}) = \begin{pmatrix} -p + \mu 2u_x & \mu(u_y + v_x) \\ \mu(u_y + v_x) & -p + \mu(2v_y) \end{pmatrix} \tag{4.30}$$

6. The total drag force in the horizontal direction is obtained by summation of the individual contributions from each marker

$$F_{drag} = \sum_m F_m = \sum_m (\bar{\bar{T}} \cdot \hat{n}) \cdot \hat{e}_x \Delta s \tag{4.31}$$

where $\hat{n}$ is the normal vector at marker m and Δs is the boundary length attributed to each marker.

The theoretical solution for Oseen's equations are used for validation of our drag algorithm. The Oseen's equations for flow due to a moving body at small Reynolds number are the solutions to the Navier-Stokes equations at steady state [94]. The boundary conditions used in this case are the ones for a rigid body immersed in a uniform flow $\vec{U}$.

$$\vec{u} = 0 \quad \text{at the surface of the rigid body} \tag{4.32}$$

$$\vec{u} \rightarrow \vec{U} \quad \text{when} \quad \vec{r} \rightarrow \infty \tag{4.33}$$

$$p \rightarrow p_0 \quad \text{when} \quad \vec{r} \rightarrow \infty \tag{4.34}$$

There are no exact solutions that satisfy all the boundary conditions, however if we neglect the flow features at infinity, approximate solutions can be obtained [94],

$$\vec{u} = C\vec{U}\Big(-\frac{1}{2}\log\frac{r}{a} - \frac{1}{4} + \frac{1}{4}\frac{a^2}{r^2}\Big) + C\vec{x}\frac{\vec{U}\cdot\vec{x}}{r^2}\Big(\frac{1}{2} - \frac{1}{2}\frac{a^2}{r^2}\Big) \quad \text{and} \tag{4.35}$$

$$p = p_0 + C\mu\frac{\vec{U}\cdot\vec{x}}{r^2}. \tag{4.36}$$

The normal and tangential stresses at the surface of the cylinder can be derived from equations 4.35 and 4.36. These stresses exert a force on the cylinder surface causing a drag per unit length equal to $D = C\ 2\pi\ \mu\ \vec{U}$ where C is an arbitrary constant [94]. The convergence for our drag algorithm using $\vec{u}$ and p given by equations 4.35 and 4.36 is shown in figure 4.13.

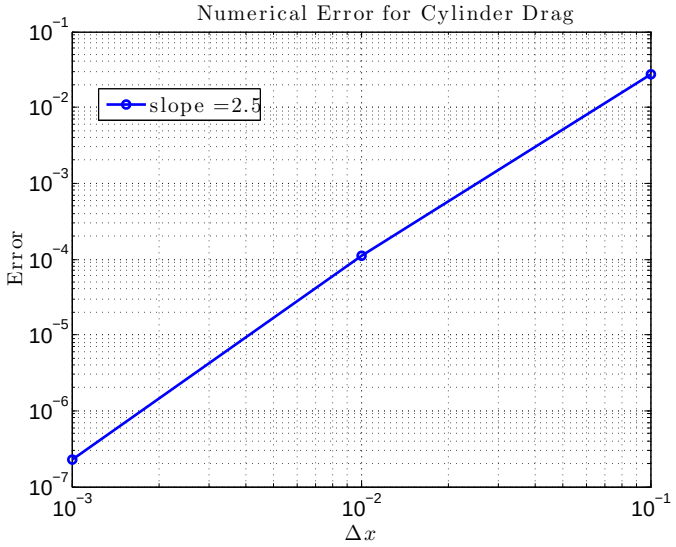

Figure 4.13: Convergence of drag using Oseen's theoretical solution for a solid cylinder. The absolute error is shown versus resolution.

Next, we simulate the flow around a porous cylinder located in the center of a rectangular domain. The boundary conditions are selected according to the configuration outlined in figure 4.12 with u_0 and v_0 calculated from equation 4.35. The numerical velocity and pressure are shown in figure 4.14 for $Re = 1$ and $Da = 10^{-4}$.

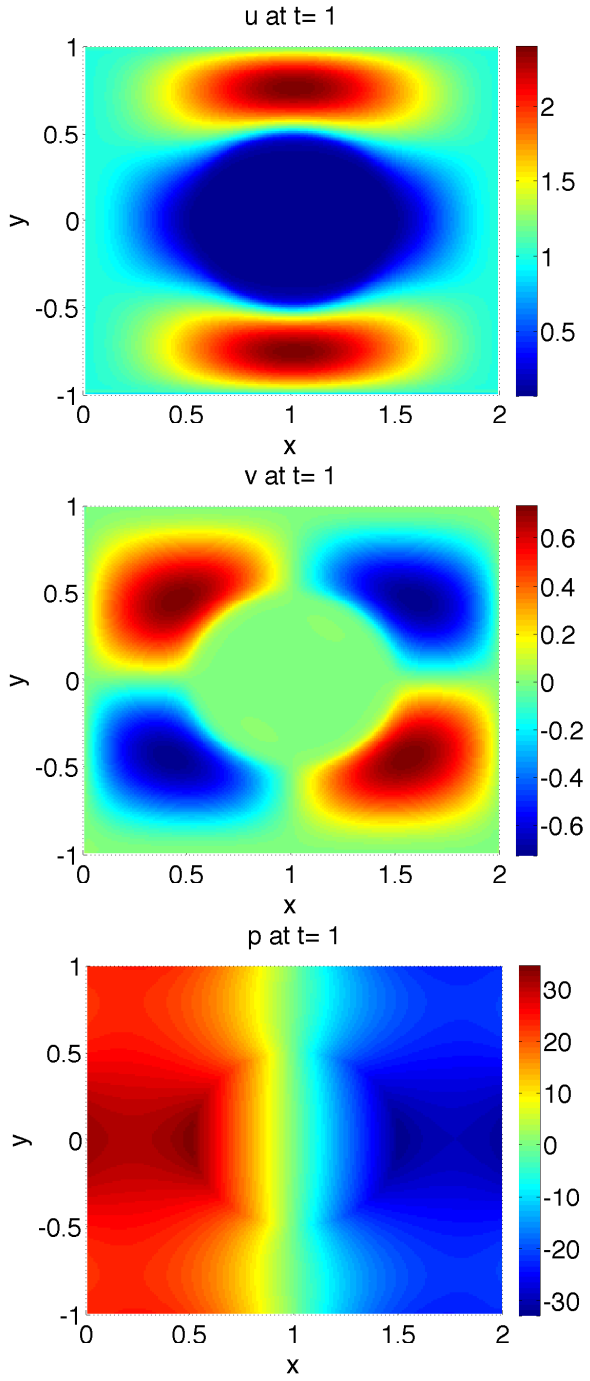

Figure 4.14: Simulation results for velocity and pressure fields around a porous cylinder for $Re = 1$ and $Da = 10^{-4}$.

The flow around a porous cylinder is validated by comparing the numerical drag versus the Oseen drag. We use $Re = 1$ and $Da = 10^{-4}$ to replicate a similar flow as the Oseen flow in equation 4.35. Published results confirm that a porous cylinder with $Da = 10^{-4}$ has similar drag to a solid cylinder within an error margin of two percent. [95]. In addition Oseen equations are valid for flow

at $Re = 1$ [94]. We conclude that although we use a porous cylinder in our simulation, the flow features are very similar to the flow around a solid cylinder. Figure 4.15 confirms the convergence of the numerical drag toward the Oseen drag as $\Delta x \to 0$. Convergence appears slow, because of the large changes in derivatives near the interface. For the resolution used ($\Delta x \geq 0.01$), the relative numerical error for gradients close to the interface remains large (< 0.2).

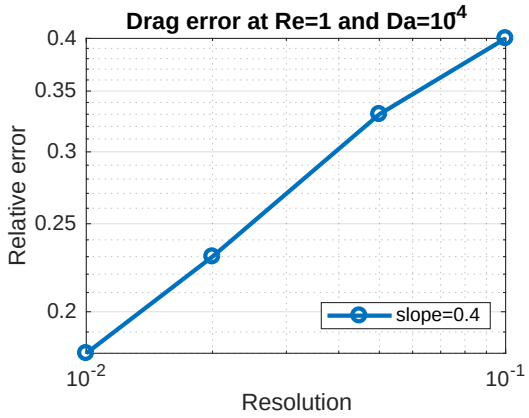

Figure 4.15: Numerical drag converges with resolution. Relative error approaches zero as $\Delta x \to 0$. The data point at $\Delta x = 0.1$ was ignored for the slope evaluation.

4.5 Domain decomposition and parallel computing

In the bigger perspective, utilizing the single domain approach over the whole domain for estimating erosion is not realistic unless unlimited computer resources are available. The mixed solver uses an implicit numerical method because of the Brinkman equation and hence is computationally more expensive than the fluid solver. We intend to apply the mixed domain approach only in areas where the probability for erosion is high. In the mixed domain, fluid velocity at the fluid-porous interface is non-zero and can be used to determine the erosion rate. This approach requires the fluid solver to exchange boundary information with the mixed solver in the selected subdomain. In cases where the flow is periodic in the x-direction the boundary information exchange is not required for the left and right hand side boundaries.The sketch in figure 4.16 discloses the details of this unique process.

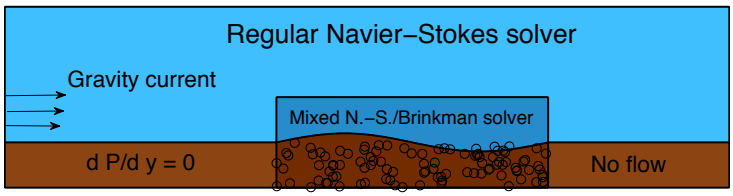

Figure 4.16: Our fluid-porous solver is applied in areas where erosion is likely to occur.

The challenge with this approach is to obtain the fluid velocities at the boundaries of the designated box. Measured data is normally not available in these situations, therefore we must rely on an external fluid solver. We call this new approach with a mixed subdomain inside a larger fluid

domain, for "Domain Decomposition". There are three main strategies to obtain the boundary data in the fluid-porous domain.

1. The same methodology as a parallel fluid solver is implemented. At each time step, the pressure will be solved iteratively in both domains simultaneously. This method is efficient and accurate but complex. The accuracy is identical to the case as if the whole domain was solved in one large big mixed-domain.
2. Fluid and mixed solver run simultaneously and exchange boundary information at each time step as depicted in figure 4.18. In this approach, the horizontal and vertical velocity components (u and v)are matched at the boundaries while the pressure is solved separately in each domain. It is possible to employ a predictor-corrector step, where boundary information is exchanged between the fluid and mixed domain multiple times (cycles) within each time step. One or more cycles could be repeated to achieve the desired accuracy depending on the selected overlap height. The overall solution will converge slowly as the flow approaches steady-state. Although this method is easy to implement, the solution is most accurate only at steady-state. The usefulness of this method is questionable as for reliable predictions of erosion, the interface velocities must be accurate at all times.
3. The fluid solver simulates the flow with no slip boundary condition at the bottom. The velocity and pressure are saved at each time step and used as boundary condition in the mixed-domain solver. This strategy is simple but works best when the flow at the interface is relatively small.

4.5.1 Modular mixed and fluid solvers

The ideal design for fluid-porous simulations is a modular approach where pure fluid and mixed solver subdomains are connected similar to pieces of a puzzle. This approach is flexible and powerful and can be used for any arbitrary porous-fluid configuration. The main three advantages are:

1. Each subdomain runs on a separate processor. This allows the user to run simulations with higher resolution over larger domains.
2. Any fluid-porous configuration can be simulated.
3. External fluid solvers can easily be integrated into our unique mixed solver.

We allow each subdomain to have one layer of overlap with other subdomains because of the MAC grid. The overlap layer can be chosen in different formats but since the mixed subdomain is solved using an implicit method the overlap should be chosen in such a way that it surrounds the mixed subdomain at all sides.

We demonstrate this approach by simulating flow over a porous cylinder. This configuration includes 5 fluid and 1 mixed subdomains as depicted in figure 4.17. We validated that this flow was identical to as if we had one contiguous larger domain. Erosion simulations are computationally expensive because they require high resolution specially at the interface separating the fluid from porous media.

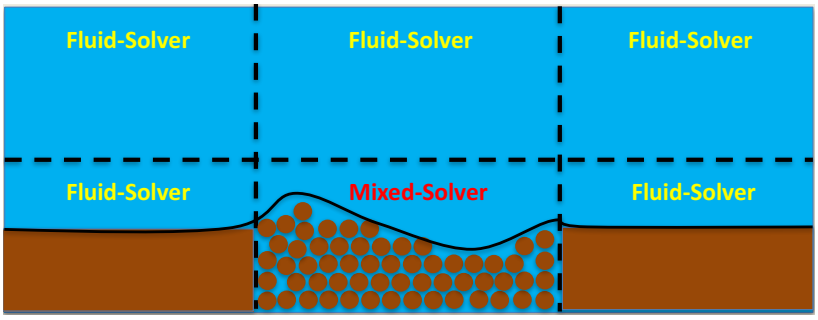

Figure 4.17: A fluid-porous domain is divided into smaller subdivisions. This modular design uses parallel computing for fluid-porous simulations.

4.5.2 Domain decomposition by matching velocities

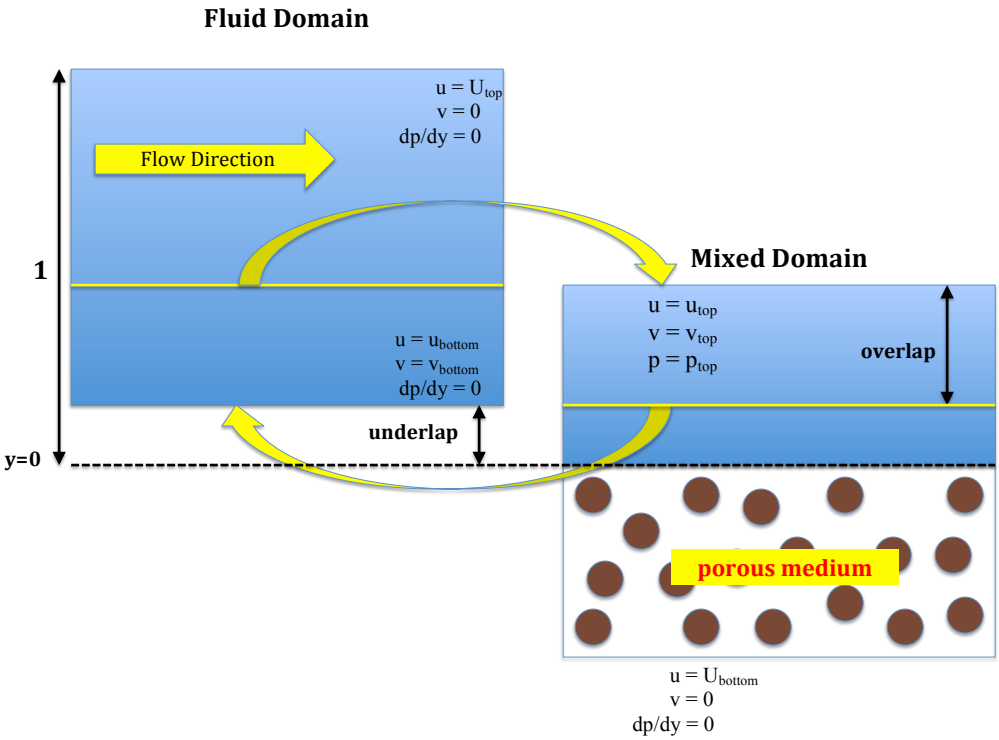

Figure 4.18: The fluid solver and the mixed solver exchange boundary information at each time step. Initially, the error is large but coverges quickly as we march toward steady state.

The schematics of domain decomposition technique is depicted in figure 4.18. The steps for implementing this method are:

1. We select the desired overlap and underlap heights. The underlap is the distance between the lower boundary of the fluid domain and the interface. It is important that the underlap is always greater than zero since we apply a tangential stress jump at the interface. The overlap parameter must be chosen with care. A bigger overlap is computationally more expensive but offers more stability.

2. We integrate the fluid domain from t^n to t^{n+1} using u_{bottom} and v_{bottom} at $y = underlap$ from the mixed domain. If an implicit solver is used for the fluid domain it is important to choose the boundary conditions at the right time. This step is called the predictor step.

3. We complete our cycle by integrating the mixed domain from t^n to t^{n+1} using u_{top}, v_{top} and p_{top} from the fluid domain at $y = underlap + overlap$. For our time integration, we use the boundary conditions at the right time. This step is called a corrector step.

4. For each time step it is recommended that the cycle is repeated two times. There is a significant improvement by repeating two cycles versus only one. To reduce the error we could also try to choose a bigger overlap at the expense of computational cost. The solution of the split-domain solver approaches the solution for the full mixed domain solver at steady state.

Validation and numerical error for domain decomposition

We validate the split-method using the pipe flow example shown in figure 4.7 where exact analytical solutions are available.

Generally the numerical error for the split method converges well as the solver marches toward steady-state. The behavior and the order of convergence depends on different parameters such as ζ, Da, Re, number of cycles, overlap and underlap. The trend is shown in the figure series 4.19. We will not explore this method further as the error is larger in most situations compared with the single domain mixed solver.

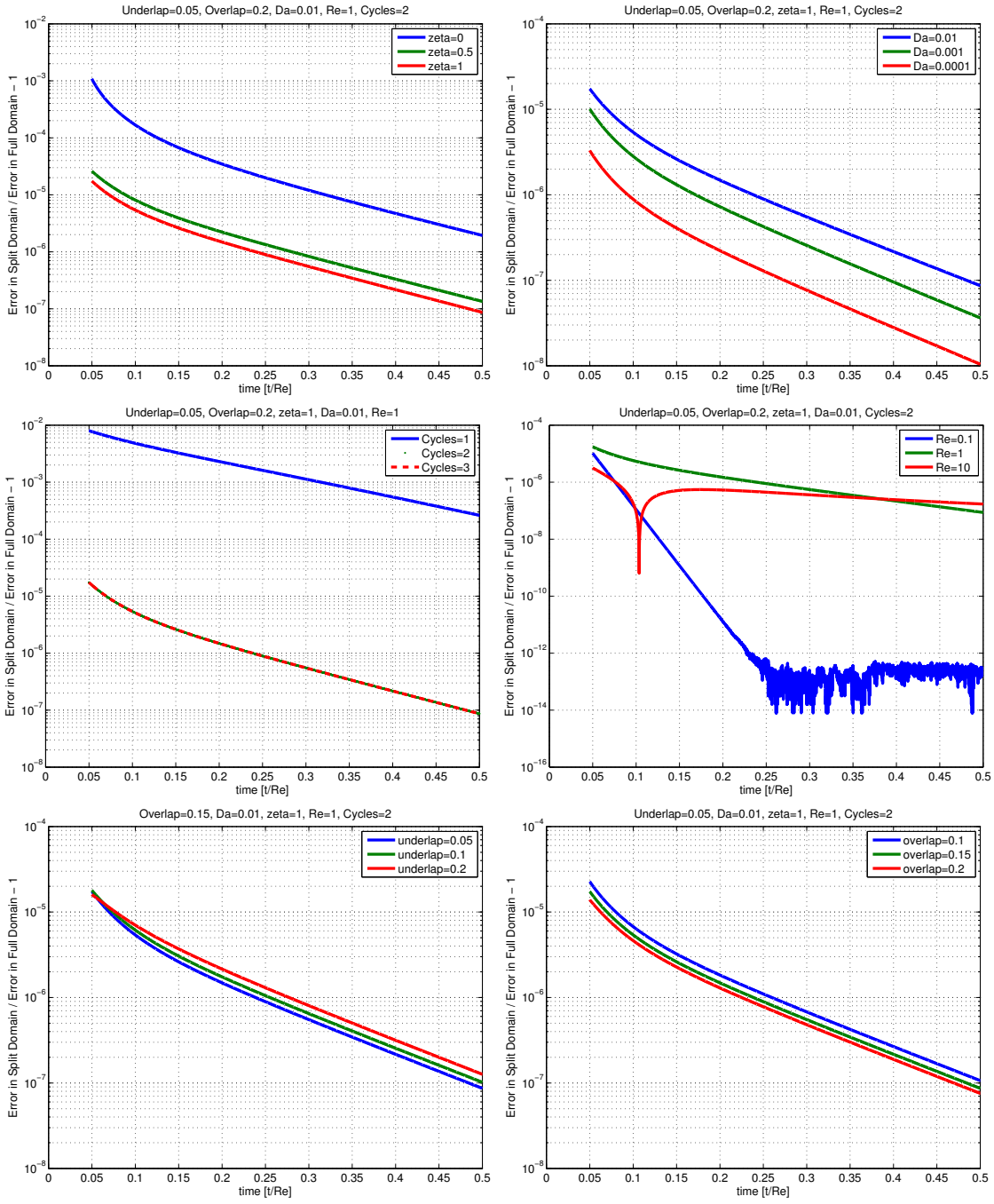

Figure 4.19: Convergence plots are shown for different parameters in our domain decomposition approach. The numerical error is larger than the single domain mixed solver but converges well at steady state.

4.5.3 Explicit parallel fluid solver

We present a parallel fluid solver for 2D incompressible Navier-Stokes equations. We employ finite differences on a staggered grid as depicted in figure 4.20. The projection method is used to solve for the pressure and the updated velocity. In a parallel solver, the boundary information must be shared between subdomains at each time step. Because of the nature of the staggered grid there must be one layer of overlap between the subdomains. Different boundary conditions require different grid configurations which must be taken into consideration.

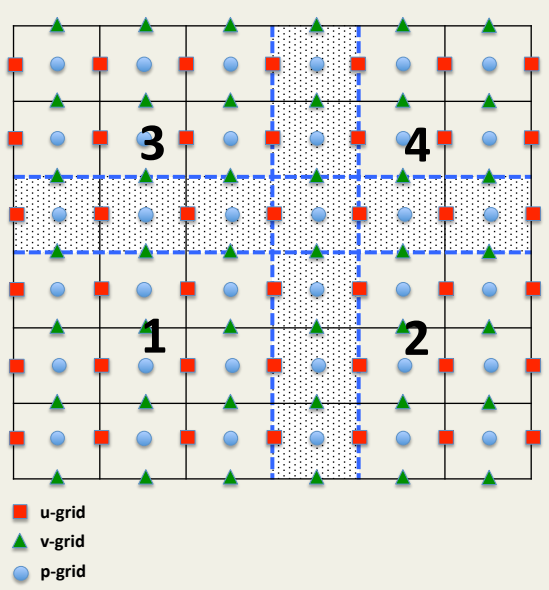

Figure 4.20: MAC grid was used in our simulations. The numbers indicate splitting of our domain into subdivisions for parallel computing.

The steps for our parallel solver implementation are:

1. We evaluate $\vec{u}^*$ by neglecting the pressure term. Boundary information for each subdomain must be updated before evaluating $\vec{u}^*$.

$$\vec{u}^* = A^{-1}\Big[\vec{u}^n + \Delta t\Big(- \vec{u}\cdot\nabla\vec{u} + \frac{1}{Re}\nabla^2\vec{u} + \vec{f}\Big)\Big]$$

   Note that the operator A^{-1} becomes the identity matrix for an explicit solver. For implicit methods like Crank-Nicolson and our new mixed solver, A^{-1} will become a non-sparse matrix.

2. Next, we use the projection method to solve for the pressure by enforcing the volume conservation of the fluid. This implies that we have to solve the poisson equation at each time step.

$$\nabla\cdot A^{-1}\nabla p = \frac{\nabla\cdot\vec{u}^*}{\Delta t}$$

   We solve the poisson equation by iterative means (Biconjugate Gradient Stabalized Method). We repeat the iteration in each subdomain until the residual is reduced below the tolerance. This process requires the pressure boundary values for each subdomain to be updated at each iteration.

3. If any of the subdomains contains porous media, the A^{-1} operator must be applied to an augmented mixed subdomain with an extra layer of grid points from neighboring subdomains. The augmented subdomain ensures that A^{-1} operator is applied correctly to all discrete pressure values inside the mixed subdomain.

4. Last, we update $\vec{u}^*$ to retain the correct velocity. This step can be performed separately within each subdomain, using the most updated boundary values.

$$\vec{u} = \vec{u}^* - \Delta t \; A^{-1} \nabla p$$

4.6 Iterative and direct methods for pressure solver

In many areas of scientific computing, iterative methods are employed for solving large sparse linear systems. Even with the latest advances in development of more efficient iterative algorithms, convergence to a solution can not be guaranteed. The direct solution methods are still very popular in real applications because they are more robust and predictable. Iterative linear solvers are ideal when physical information of a specific problem can be used to obtain more robust methods. In addition, iterative methods are easier to implement for parallel computing [96].

There are many different iterative methods available for solving a linear system for pressure. Two methods, GMRES (Generalized Minimal Residual Mehod) [97] and BICGSTAB (Biconjugate Gradient Stabalized Method) [93] were chosen for a closer investigation. The single most important issue is to ensure convergence for large systems. Also parameters like convergence time and number of iterations are critical for computational efficiency. The evaluation result for these methods is summarized for systems with different sizes in table 4.1.

Method	Size of Matrix A	Tolerance	Convergence Time [s]	Number of Iterations
BICGSTAB	2400 x 2400	1.00 E-12	0.12	54
BICGSTAB	9800 x 9800	1.00 E-12	0.34	87
BICGSTAB	19600 x 19600	1.00 E-12	0.92	112
BICGSTAB	40000 x 40000	1.00 E-12	2.2	148
GMRES	2400 x 2400	1.00 E-12	0.22	39 x 5
GMRES	9800 x 9800	1.00 E-12	2.5	125 x 7
GMRES	19600 x 19600	1.00 E-12	5.2	183 x 3
GMRES	40000 x 40000	1.00 E-12	21.1	371 x 1

Table 4.1: Comparison of BICGSTAB and GMRES

The linear systems we consider here, are mostly sparse but non-symmetric and consequently ideal for a selected number of iterative methods. We demonstrated numerically that the "BICGSTABL" method is consistently superior than "GMRES" specially when it comes to higher resolutions.

Next, we compare the BiCGSTABL algorithm with a direct linear solver. We would like to know how much faster the "BICGSTABL" algorithm is compared with a direct solver and what is the highest resolution we could run without the iterative error becoming the dominant error. The iterative error will increase with resolution as the differential error will decrease. The iterative pressure solver is not ideal when the iterative error dominates relative to the finite difference approximation.

We analyze the performance of the iterative pressure solver (BICGSTABL) by using a convergence study to illustrate its usefulness and limitations compared to a direct pressure solver. A fluid problem with known analytic solution was used for convergence study. The computational domain size was "1×1", $dt = 0.00005$ and $t_{final} = 0.001$. The result is shown in figure 4.21.

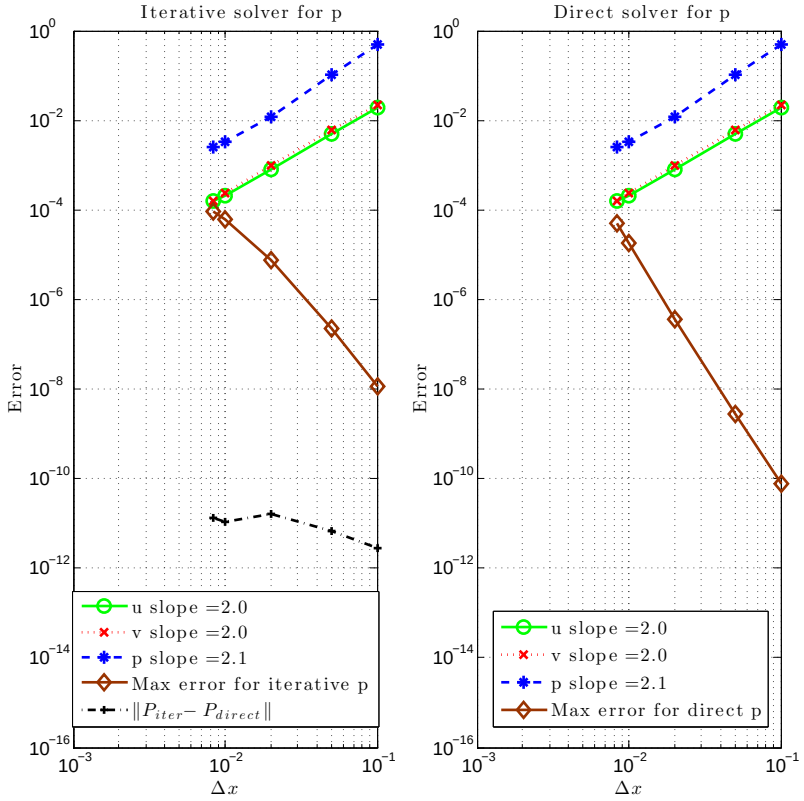

Figure 4.21: Error study was conducted for direct and iterative pressure solvers. Iterative solver performs as well as the direct solver.

The convergence plot illustrates the second order convergence for both solvers. This indicates that both methods yield acceptable results. The best approach is to pick the faster method in each scenario. The brown curves in figure 4.21 show the maximum numerical error in pressure. This error is proportional to the condition number which increases with grid size N. Once the maximum error is greater than the error due to the finite difference approximation for pressure, the theoretical limit for lowest possible error has been reached and further resolution enhancement will not contribute to a more accurate pressure. The blue and brown curves intersect at $\Delta x \approx 0.005$ if the tolerance for the iterative pressure solver is set to 10^{-11}.

$$\text{Blue line:} \quad log_{10}(\|P - P_{exact}\|)_{FD} = 2log_{10}(\Delta x) + 1 \tag{4.37}$$

$$\text{Brown line:} \quad log_{10}(\|P - P_{exact}\|)_{Iter} = -3log_{10}(\Delta x) - 10.5 \tag{4.38}$$

We conduct a time study to quantify the efficiency difference between the iterative and the direct solver. In figure 4.22, we plot the time to solve for pressure versus grid size $(N)^{1/2}$.

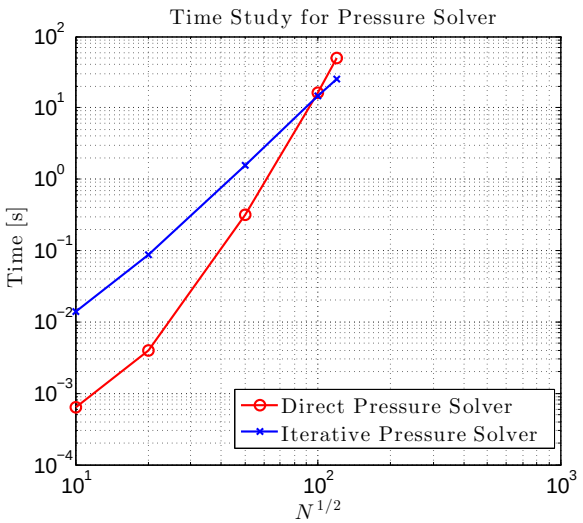

Figure 4.22: Time study was conducted for direct and iterative pressure solvers. The iterative solver is preferred for larger grid sizes.

The direct solver is faster for lower N but at $N^{1/2} \approx 100$, the iterative solver takes over and becomes faster. Matrix A is not sparse, hence it is computationally expensive to evaluate A and perform a direct Ap multiplication. This operation requires huge memory allocation and makes the iterative solver always slower than the direct solver. An alternative approach is to do the multiplication Ap in steps outlined in equations 4.39 and 4.40.

$$\begin{aligned}
A\ P^{n+1} &= \left(D_x^p[A^u]^{-1}D_x^u + D_y^p[A^v]^{-1}D_y^v\right)P^{n+1} \quad \Rightarrow \\
A\ P^{n+1} &= D_x^p[A^u]^{-1}D_x^u\ P^{n+1} + D_y^p[A^v]^{-1}D_y^v\ P^{n+1} \quad \Rightarrow \\
A\ P^{n+1} &= P_1 + P_2 \\
\text{Where,}& \\
P_1 &= D_x^p[A^u]^{-1}D_x^u\ P^{n+1} \quad \text{and} \\
P_2 &= D_y^p[A^v]^{-1}D_y^v\ P^{n+1}
\end{aligned} \tag{4.39}$$

P_1 and P_2 are evaluated separately and added up toward the end. The steps for calculating P_1 are shown below:

$$\begin{aligned}
P_1 &= D_x^p[A^u]^{-1}D_x^u\ P^{n+1} \quad \Rightarrow \\
P_1^1 &= D_x^u\ P^{n+1} \\
A^u P_1^2 &= P_1^1 \\
P_1 &= D_x^p\ P_1^2
\end{aligned} \tag{4.40}$$

P_2 will be evaluated exactly the same way and added to P_1 which completes the multiplication process. The reason this modified multiplication method is less expensive in terms of efficiency and memory allocation is that D_x, D_y, A^u and A^v are all band matrices but their inverse matrices are typically non-sparse. For a 120×120 grid size system, it takes 25 seconds to solve the poisson equation using the iterative pressure solver versus 50 seconds using the direct solver on a personal laptop.

4.7 Summary

We have introduced a numerical method for accurate and flexible simulation of a system consisting of homogenous fluid and porous medium separated by a sharp interface. In particular, our approach can easily be made to adjust to any geometry, and can also track a mobile interface between the two media. We developed our method by incorporating the idea of single-domain covered by an Eulerian grid, supplemented by a localized force on a Lagrangian interface able to account for a stress jump boundary condition. To implement this interfacial force, we compared a line-integral approach with a numerical delta function approach, and concluded that the line-integral approach is generally more accurate, though its error varies more with the position of the interface relative to the grid. Our method was validated against an analytical pipe-flow solution and found to be second order accurate both in time and space away from the interface, and first order at the interface when there is a stress jump.

We also found that solving for the pressure was computationally the most expensive step, requiring to solve a non-sparse linear system. We compared iterative and direct pressure solvers and presented a time study confirming the benefits of iterative solvers for big systems. For larger domains, our method is therefore better incorporated in parallel to a traditional fluid solver. The localized use of our method will provide a more accurate description of the flow near and below the interface. We discussed three different modular approaches and concluded that the most accurate parallel solution is to solve for pressure iteratively in the whole domain.

Chapter 5

Simulation of erosion

5.1 Introduction

In natural systems involving sediment, particulate movement occurs mainly through two mechanisms: suspension (or resuspension) and bed-load transport. Suspended particles are advected by the flow and detach from the bed completely. On the other hand, bed-load transport consists of particles that slide, roll or saltate in proximity to the deposit [20, 98]. Such particle movement is somewhat erratic, with brief pulses of motion affecting random local groups of particles.

As the flow becomes stronger, smaller particles moving near the bed are lifted upward by turbulent eddies and travel downstream as suspended load [98]. The concentration of suspended sediment increases rapidly as the flow gains more vigor. While bed-load transport involves mostly particle-particle interactions, which are notably difficult to capture with a continuum approach, resuspension occurs mostly through fluid-particle interactions. As our simulations allow for an accurate description of the fluid flow near the interface, we will focus here on the resuspension effects and demonstrate the use of our new method to simulate the erosion of a particulate deposit.

Our simulations will account for flow in and over the deposit, in contrast to the classical approach, which assumes a solid deposit [23,99]. We consider the porous matrix to be fixed, as we focus on the onset of erosion. As erosion occurs, the top-most particles will become suspended in the fluid and the interface profile will be altered. Our method has the capability to allow for a mobile interface, but as an initial implementation we assume the interface fixed. In most fluid-porous media interactions, erosion is limited to narrow locations, and we anticipate that our mixed solver can be integrated into a larger fluid solver, and used only where erosion is highly probable. This process can be easily parallelized.

5.2 Equations of erosion

The physical system we described so far depends on three non-dimensional parameters: the Reynolds number Re, the Darcy number Da and the constant ζ. In erosion applications, an additional description of the deposited particles is required. We assume here that the fluid consists entirely of water at normal atmospheric conditions with $\rho_f = 1000 \frac{\text{kg}}{\text{m}^3}$ and $\mu = 10^{-3}$ Pa s. The Reynolds

number in natural environmental settings is often very high, and hence requires high resolution and small time steps. To keep computational times reasonable, we consider a smaller domain, envisioning that it is part of a larger simulation. In our simulation model, we set the physical domain width to $L = 1$ mm. For simplicity, the porous medium is assumed to consist of perfect spherical plastic beads. The particle diameter, which affects permeability and so Da, is typically set to $d = 0.1$ mm, enforcing the constraint $d \leq \frac{L}{10}$ to maintain the validity of the Brinkman equations. We relate the permeability, K, to the deposit's porosity, ϵ, and particle size, d, through an empirical formula for randomly packed spherical particles $K = \frac{\epsilon^{5.5}}{5.6} d^2 = Da\ L^2$ [100]. Smaller values of Da require higher resolution and we therefore choose the largest particle diameter allowed by our domain size.

The density of the deposited beads is taken to be $\rho_p = 1100 \frac{\text{kg}}{\text{m}^3}$. This is lower than the density of sand particles, but comparable to beads used in experiments, and enables us to promote erosion at a lower Re. We choose the range of our key parameters to ensure we capture the onset of erosion, yielding: $100 \leq Re \leq 700$, $2 \times 10^{-5} \leq Da \leq 5 \times 10^{-5}$, and $-0.5 \leq \zeta \leq 0.5$. The selected Da range corresponds to a porosity of $44.2\% \leq \epsilon \leq 52.2\%$ when $d = 0.1$ mm.

Various empirical models have been developed to quantify entrainment from both resuspension and bed-load transport [101]. For comparison, we will refer to a model widely used in applications derived by Garcia & Parker [23], which we refer to as the GP model. This model accurately averages erosion over larger domains, but it does not provide detailed information about local effects, or distinguish between bed-load transport and resuspension. In the GP model, the resuspension flux $F_r = F_{GP}\ U_s$, is evaluated by an empirical formula, with U_s denoting the particle settling speed determined using the empirical formula developed by Dietrich [102]. The resuspension flux is related to the particle Reynolds number Re_{pa} and bottom shear velocity u_{sh}. The strength of the resuspension is a smoothed step-function of the variable Z, defined as

$$Z = u_{sh}\ Re_{pa}^{0.6} \quad \text{if } Re_{pa} > 2.36, \tag{5.1}$$

$$Z = 0.586\ u_{sh}\ Re_{pa}^{1.23} \quad \text{if } Re_{pa} \leq 2.36 \tag{5.2}$$

where u_{sh} and Re_{pa} can be expressed as

$$u_{sh} = \frac{U}{U_s} \sqrt{\frac{1}{Re_f} \frac{\partial(\vec{u} \cdot \vec{t})}{\partial n}\Big|_{\text{interface}}}\ , \tag{5.3}$$

$$Re_{pa} = \frac{\rho_f\ d\ (gdR)^{1/2}}{\mu} \tag{5.4}$$

where g is the gravitational acceleration and $R = \frac{\rho_p - \rho_f}{\rho_f}$. In our simulations Re_{pa} is always close to one and hence only the lower branch of Z is used. The normalized resuspension flux, $F_{GP} = \frac{F_r}{U_s}$, is defined as

$$F_{GP} = \frac{aZ^5}{1 + \frac{a}{0.3} Z^5} \tag{5.5}$$

where $a = 1.3 \times 10^{-7}$ is an empirical constant. This normalized flux may also be viewed as a concentration of entrained particles, and may not exceed 0.3 due to a saturation mechanism.

In our model, instead of relating the erosion flux empirically to the tangential stress, we consider the velocity of the flow at the porous interface, and compare it to the particle settling speed. The positive normal component of the fluid velocity minus the particle settling velocity, u_{pa}, is defined as

$$u_{pa} = \max\left(\left\{(\alpha \vec{u}\Big|_{\text{interface}} - U_s \hat{e}_z) \cdot \vec{n}, 0\right\}\right), \tag{5.6}$$

where α is an empirical constant that may be used to take other factors into account, for example the adhesive forces between the particles. However, in the absence of a quantitative analysis, we

don't yet know how exactly α may depend on d, Re, or Da, and so we set $\alpha = 1$. The normalized resuspension flux for the new model F_{new}, is defined as the product of the interface particle velocity u_{pa} and the non-dimensional particle concentration in the deposit

$$F_{new} = \frac{u_{pa}\ (1-\epsilon)}{U_s}. \tag{5.7}$$

Figure 5.1 depicts schematically both models.

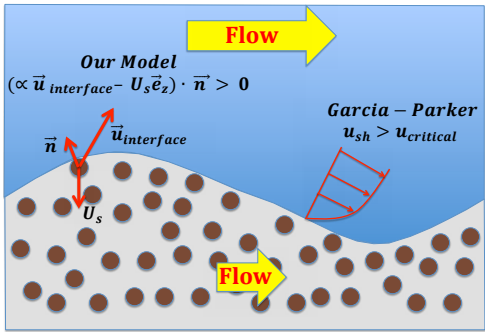

Figure 5.1: Schematics of the GP erosion model and of the proposed erosion model.

We note that our model uses exclusively the computed velocities at the interface to determine the suspension of particles. This is expected to be most useful in situations where suspension is the dominating mode of transport, such as the spread of contaminants or bacteria. For a complete erosion model, one will need to incorporate the bed-load transport occurring mostly at lower Re or when larger particles are present. However, quantifying suspension and the fluid flow in the porous medium is a necessary step toward obtaining an erosion model that accurately captures both effects and provides insight into erosion mechanisms. The empirical model we show here for comparison does not separate resuspension and bed-load transport. We therefore anticipate that it will predict more erosion than our partial model which focuses on resuspension alone, but will still provide a useful benchmark to assess the usefulness of our model.

5.3 Swirling flow

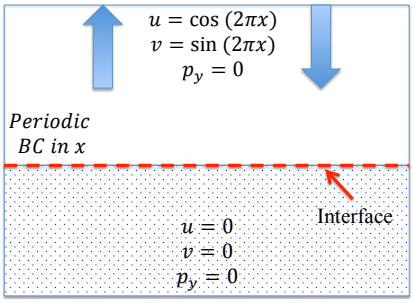

Figure 5.2: Schematic of the swirling flow simulated, with boundary conditions applied.

The first application simulated was what we called a "swirling flow", which is depicted in figure 5.2, along with the relevant boundary conditions. At the top boundary, we apply a sinusoidal velocity

profile, creating a circulating flow inside the domain. The velocity profile is symmetric at the top, with exactly one period across the domain, which ensures no net flow into or out of the domain. At the bottom boundary beneath the porous medium, we apply a no-slip, no-penetration boundary condition. A sample result for $Re = 600$, $\zeta = 0$ and $Da = 2 \times 10^{-5}$ is shown in figure 5.3. The velocity vector field shows the pattern of the flow in our computational domain, and the streamlines are shown close to the interface. We also show the vorticity pattern over the whole domain.

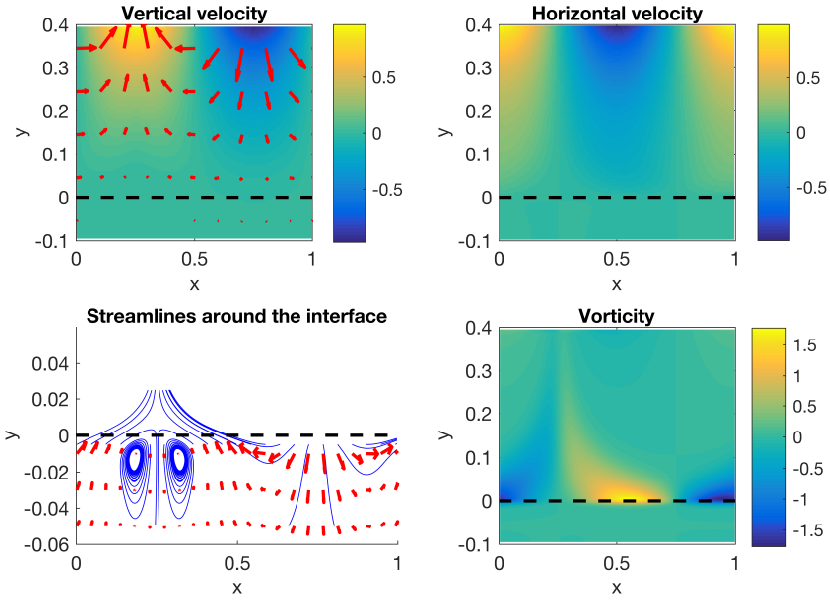

Figure 5.3: Swirling flow velocity profile in the computation domain and zoomed in at the interface. The double vortex in the left corner of the porous medium causes the flow to become asymmetrical at higher Re numbers.

We first note the presence of a double vortex in the porous matrix beneath the region of upflow, as can be seen in figure 5.3, breaking the flow's symmetry close to the interface. As Re gets larger, these vortices grow in vigor and penetrate the interface into the fluid domain. These vortices are the result of the (locally) high pressure area that forms around the stagnation point located beneath the region of upflow. As fluid is able to penetrate inside the porous layer, no stagnation point forms near the interface beneath the downflow region.

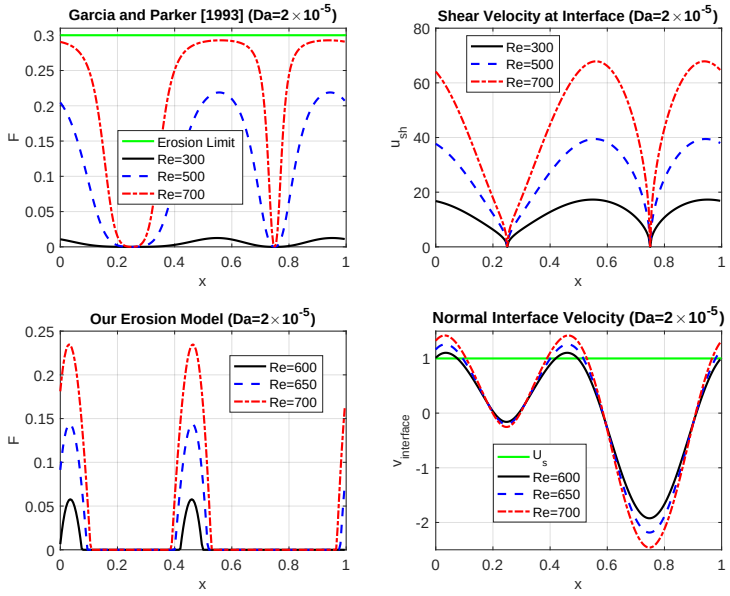

Figure 5.4: Erosion flux for swirling flow at different Reynolds numbers. The top two figures show results for the GP erosion model, and the bottom two figures show results for the proposed erosion model.

The most determinant parameter promoting erosion in our simulations is the Reynolds number. Higher Re indicate a flow with more momentum to transport solid particles away from the upper layer of the porous medium. Figure 5.4 shows the erosion flux for both the GP model and our model for different values of Re. Here, F represents the normalized flux and is shown versus the x position along the interface, with higher F corresponding to a greater erosion rate. The shear velocity u_{sh}, which is directly proportional to the stress at the interface, is also shown. All parameters are normalized with the non-dimensional settling speed U_s for ease of comparison. It can be seen that both models predict a significant increase of erosion for larger Re. Our model predicts that erosion first occurs at $Re = 600$, while the GP model predicts erosion at Re as low as 300. This is attributable to the fact that at lower Re particles move primarily as bed-load, by hopping, rolling, and/or sliding. The onset of erosion thus differs between the two models because the GP model includes both bed-load transport as well as suspension, while our model only captures resuspension, which occurs at higher Re. The factor of two difference between both models is consistent with observations of when bed-load and resuspension are triggered [103].

A comparison of the location where erosion is greatest shows both models predicting that entrainment occurs from two major peaks. The GP peaks are wider with the center located in the center and beneath the downflow portion of the domain, where the fluid stress and horizontal velocities are at maximum. In our model the peaks are narrowed and located where the upward flow is strongest. Because of the presence of the double vortex, there are two such locations, on either side of the upflow in fluid. We note that simulations in which the porous medium is replaced with a solid do not show a vortex pair, and therefore predict a rather different erosion pattern, with a much less pronounced M shape peak forming under the region of upflow.

The GP model saturates at 0.3, which is imputable to upper layer particles being removed before the particles at lower depth are impacted. Our current model does not have a saturation mechanism, though as the erosion rate is increased and more particles are entrained one could replace the interface

velocity with velocity taken at a depth that depends on the erosion rate. This feature could easily be incorporated in our approach, as the fluid velocity is known anywhere inside the porous medium.

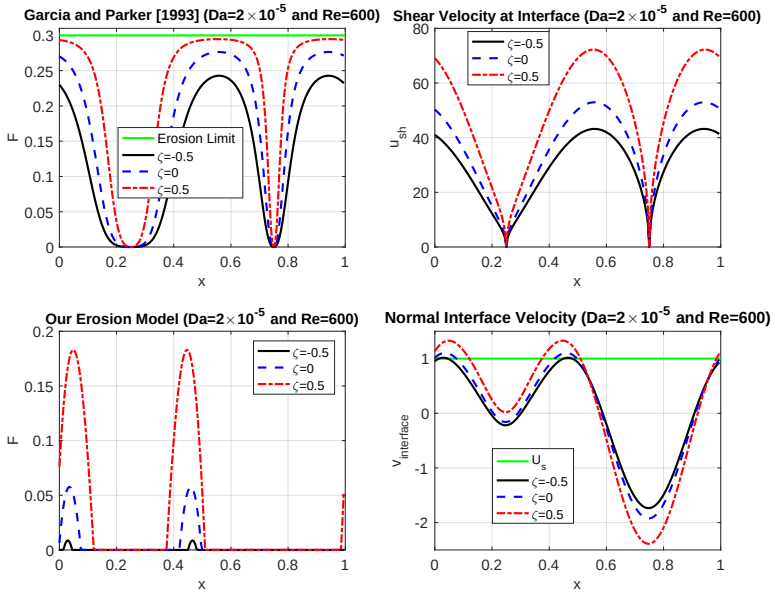

Figure 5.5: Erosion flux for swirling flow with a flat interface at different ζ. The top two figures show results for the GP erosion model, and the bottom two figures show results for the proposed erosion model.

Next we look at the influence of the parameter ζ, which measures the tangential stress jump across the boundary, with a positive ζ meaning higher stress at the boundary compared with a fluid-solid boundary. Both models predict higher erosion with increased ζ. This is directly understandable for the GP model, as greater ζ implies a larger stress at the interface, and so a higher erosion flux. Our model is based on the vertical fluid velocity at the interface, which is also increased by a greater interfacial stress, though indirectly: larger stresses enhance the strength of the circulation, which in turn increases the vertical velocity. It is also evident that the dependence of the erosion rate on ζ is greater for our model than for the GP model, which is attributable to enhanced suspension to bed-load ratio for higher stress, and the latter model's saturation level limiting its growth.

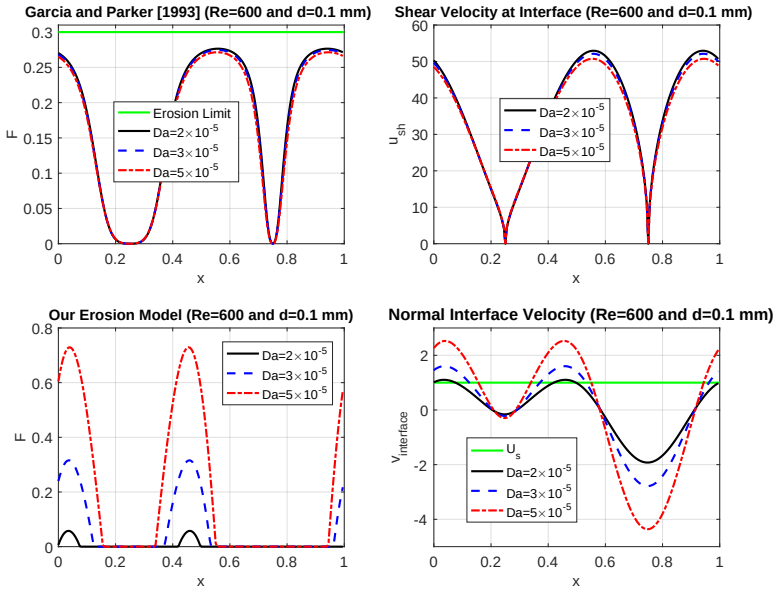

Figure 5.6: Erosion flux for swirling flow for different Da numbers and fixed particle size. The top two figures show results for the GP erosion model, and the bottom two figures show results for the proposed erosion model.

Finally, we look at how the parameter Da impacts the erosion rate. Increasing Da and keeping the size of our particles fixed to $d = 0.1$mm corresponds to increasing the porosity. We see in figure 5.6 that the GP model erosion flux is nearly independent of Da, while our model shows a strong increase of suspension flux with increased Da. For the values shown, and for smaller Da as well, increasing Da results in very slight reduction of stress at the interface. The GP model is thus nearly unaffected by such changes. However, for our method there are two major parameters influencing the erosion flux, vertical fluid velocity and particle concentration. As Da and porosity increases, the vertical fluid velocity increases rapidly while the particle concentration is reduced. The effect of higher vertical velocities is found to far outweigh the decrease in particle concentration, resulting in a rapid increase of suspension flux. An alternative interpretation of those results is that with increased Da, we encounter more suspension, while smaller Da corresponds to higher bed-load transport predicted only by the GP model.

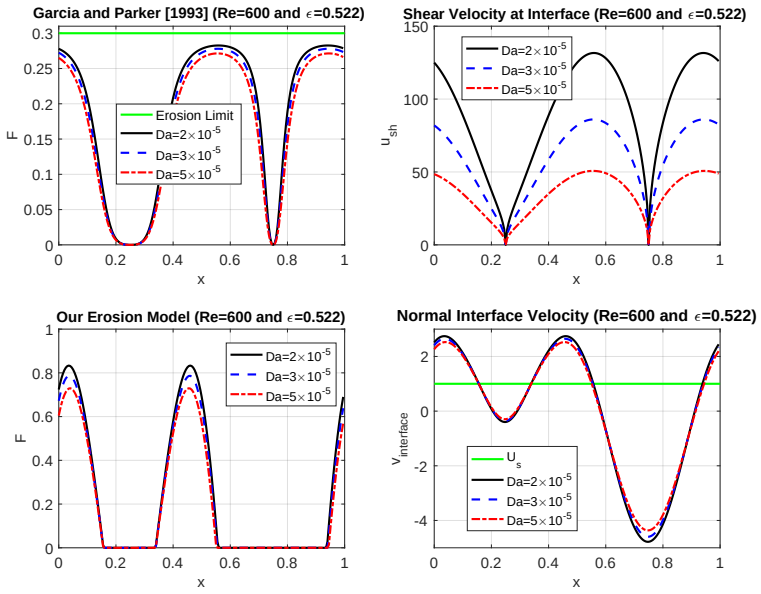

Figure 5.7: Erosion flux for swirling flow for different Da numbers and fixed porosity. The top two figures show results for the GP erosion model, and the bottom two figures show results for the proposed erosion model.

A change in Da can also be obtained by changing the particle diameter while keeping the porosity fixed. The normalized erosion flux for a fixed porosity $\epsilon = 0.522$ is shown in figure 5.7. Here, both models predict higher erosion flux with smaller Da. There are now two competing factors counteracting each other. Smaller particle sizes reduce the particle settling speed, which favors erosion in both models, either by increasing the non-dimensional stress for the GP model, or by decreasing the threshold velocity to exceed in our model. However, the flow in the porous matrix will be strongly impeded due to the low permeability associated to smaller particles. Overall, the effect of lower settling velocity prevails and the combined effect is a moderate increase in erosion flux. This result is consistent with experiments where smaller particles get eroded and suspended more easily than larger particles for a given flow, provided there are no excess adhesion forces between the particles as is the case for sediments like clay and silt. Our model could also be made to capture adhesion effects by choosing $\alpha > 1$.

5.4 Hill flow

Figure 5.8 shows the details of the second setup and boundary conditions we simulated, which we call "hill flow". This flow, with its wavy topography, is common to many natural settings. It also emphasizes the effectiveness of our method to easily simulate a system with a curvilinear interface, which is simply achieved by relocating the interfacial markers. At the top boundary, we apply a constant horizontal velocity, forcing the flow to move from left to right and transferring momentum to the fluid in the entire domain. At the bottom boundary below the porous medium, we apply a no slip, no penetration boundary condition for the velocity. The interface profile is a sine function with amplitude 0.05 and period 1 and is fixed in time.

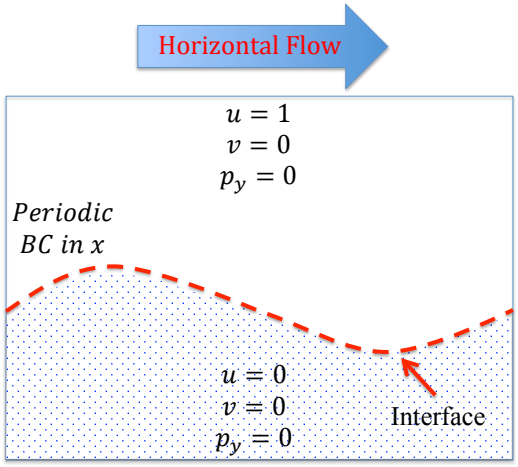

Figure 5.8: Schematics of the hill flow, with boundary conditions applied.

We show in figure 5.9 the flow resulting from letting the fluid approach steady-state from rest for $Re = 600$ and $Da = 2 \times 10^{-5}$. Although the flow on the upper part of the domain is predictably unidirectional, the flow near the interface is more interesting to analyze. Here, unlike in a system where the lower layer is solid, a portion of the flow pierces the interface across the hill profile. The most significant flow pattern is the vortex buildup behind the porous hump, sucking fluid from the trough of the interface. The flow close to the interface is strongest right at the top of the hump and slowest at the trough.

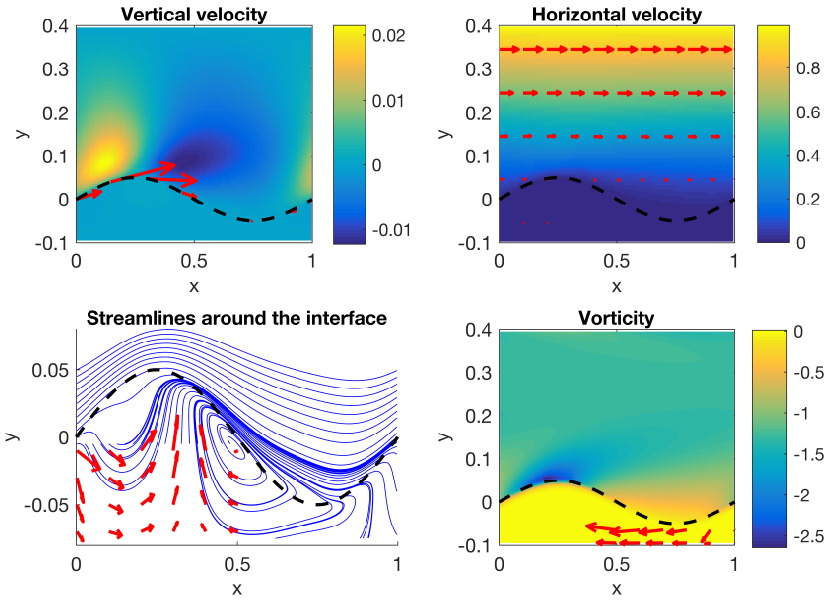

Figure 5.9: Hill flow velocity profile in the computation domain and zoomed in at the interface. The flow is strongest on top of the first hill and a vortex is formed below the middle of the interface.

The erosion flux for a hill flow for both models is shown in figure 5.10 for three different values of Re. The vertical axis F indicates the normalized flux of particles eroding away from the boundary

and the horizontal axis indicates the position along the interface. Due to the dependence of the numerical accuracy on the relative interface-grid location as shown in figure 4.10, the curvilinear interface velocity tends to be noisy. Here, to obtain a more regular resuspension profile for the same resolution as in the previous section, we computed the resuspension flux using a velocity that was averaged over two markers on each side. As in the swirling flow case, there is a significant increase of erosion when Re is higher. Our model predicts erosion starting first around $Re = 450$, while for the GP model, erosion starts at $Re = 300$. Erosion is again promoted at a lower Re for the GP model, but the difference is smaller in this set-up. This is mostly due to the increased flow within the hump region in this curvilinear set-up, which favors erosion in our model, and to a lesser degree the reduction in the normal component of the settling speed due to the slope of the interface.

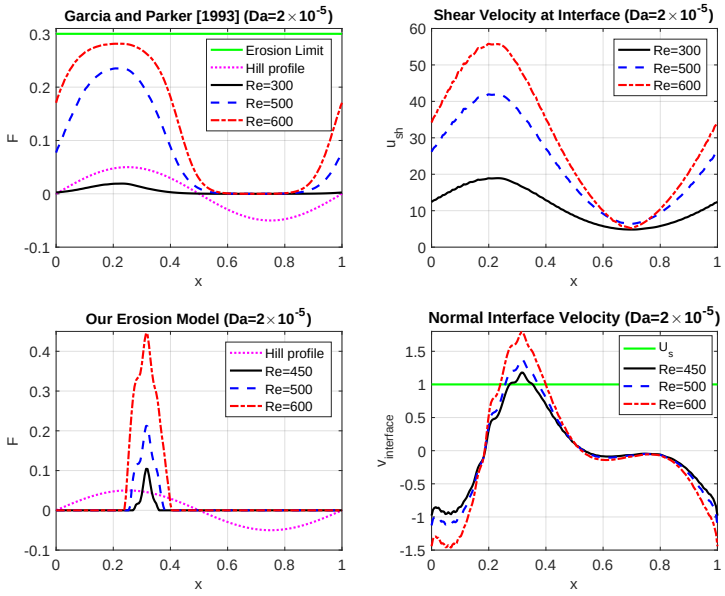

Figure 5.10: Hill flow erosion flux for both models are shown at various Re numbers. The top two figures show results for the GP erosion model, and the bottom two figures show results for the proposed erosion model.

There is also a slight difference in the location where the erosion flux is strongest. The GP model shows maximum erosion on top of the first bump with a fairly large spread covering the left side of the domain. Our model on the other hand shows a more focused maximum intensity, slightly downstream of the hump. This implies that suspension will take place most vigorously downstream of the hump, while bed-load transport starts earlier and covers the whole bump. The trends for parameters Da and ζ was similar to what was seen in the swirling flow, showing no enhanced effect with the change in geometry.

5.5 Mobile interface

In realistic natural settings, as water flows over a particulate deposit with sufficient strength, smaller size particles will be forced into suspension. This erosive process alters the shape of the interface which in turn will affect the dynamics of the flow. This complex interaction between flow and the interface is fundamental for accurate determination of flow characteristics and erosion flux. Most

traditional solvers assume a fixed interface separating the porous media from the fluid and neglect this coupled interaction. In our case, as stated previously, we construct our interface with Lagrangian markers connected by cubic splines that can easily be moved.

We now allow the interface to be mobile and observe the flow dynamics as erosion occurs. Our new approach for simulation of a mobile interface, has been implemented for the two previously examined flow types swirling flow and hill flow. It is important to reiterate the fact that our simulations focus solely on suspension and omit bedload transport, the other major component in erosion applications for simplicity. The main steps for our moving interface algorithm can be summarized as follows.

1. Initially, the particle velocity $\vec{u}_{pa}$ is calculated at each marker position used for construction of the interface. Particle velocity is defined as the normal component of the fluid velocity minus the particle settling velocity as stated in equation (25).
2. If the particle velocity is non-zero anywhere along the interface, that specific marker is repositioned by $\Delta\vec{I} = -u_{pa}\ \Delta t\ (1-\epsilon)\ \vec{n}$.
3. At every time step, all the markers are redistributed in an equidistant manner along the new interface. The periodicity in the x direction ensures that the first and last markers are positioned at the opposite ends of the x-domain, having the same y position.
4. The indicating function M identifying the porous region, is updated if the interface is displaced. This will force the fluid flow to adjust to the new profile.
5. The matrix A in the pressure poisson equation is updated since it depends on the indicating function M. This is the most computationally expensive step as it requires the recalculation of the matrix A and its inverse at every time step when erosion occurs.

The moving interface simulations have been observed to be stable for any geometry using our implicit fluid-porous solver as long as the CFL condition is satisfied, as was the case for the fixed interface case. The dominant numerical error for our method is at the interface where the largest velocity gradients are. We tried four different interpolation methods to minimize the error at the interface. The biharmonic spline interpolation was marginally superior to other methods as shown in figure 5.11.

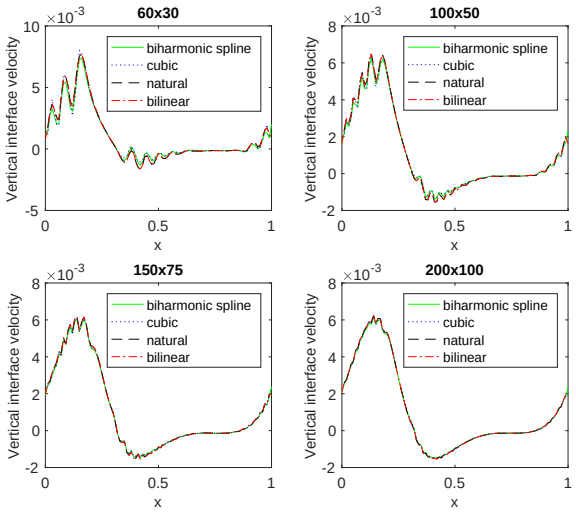

Figure 5.11: Different interpolation methods used to compute the vertical velocity at the interface of the hill profile. The parameters used were $Re = 600$ and $Da = 5 \times 10^{-5}$.

The interpolated vertical velocity at the hill profile interface is shown in figure 5.12 for different grid sizes. As expected, the oscillatory behavior originating from the numerical error dependence on the interface position with respect to the grid abates with increased resolution. We can conclude that the best way to insure a smooth interpolation is higher resolution at the interface.

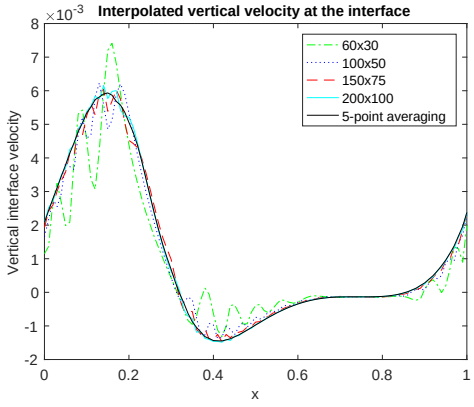

Figure 5.12: Interpolated vertical velocity at the interface for different grid resolutions for the hill flow steady state velocity profile with parameters $Re = 600$ and $Da = 5 \times 10^{-5}$. The oscillations subside with higher resolution and converge toward a smooth velocity profile.

Results

Our first experiment with a mobile interface was to repeat the swirling flow simulations. The boundary conditions and domain size are identical to our fixed interface simulations. The parameters used were $Re = 600, \zeta = 0$ and $Da = 2 \times 10^{-5}$. The main advantage here is that we can observe the fluid interaction with the porous medium as erosion takes place. We start the simulation with the steady state velocity profile for our fixed interface swirling flow. Under these specific flow conditions, the flow is strong enough to initiate erosion proportional to the normal fluid velocity at the interface. The moving interface is shown together with the vertical fluid velocity in figure 5.13 and compared with the classical Garcia-Parker model. In the GP model, the displacement is $\Delta\vec{I}_{GP} = -F_{GP}\ U_s\ \Delta t\ \vec{n}$ where F_{GP} is the erosion flux given by equation (24). For this model only, we assume constant flux calculated from the fixed interface flow and hence the displacement is given by $\vec{I}_{GP} = -F_{GP}\ U_s\ t\ \vec{n}$.

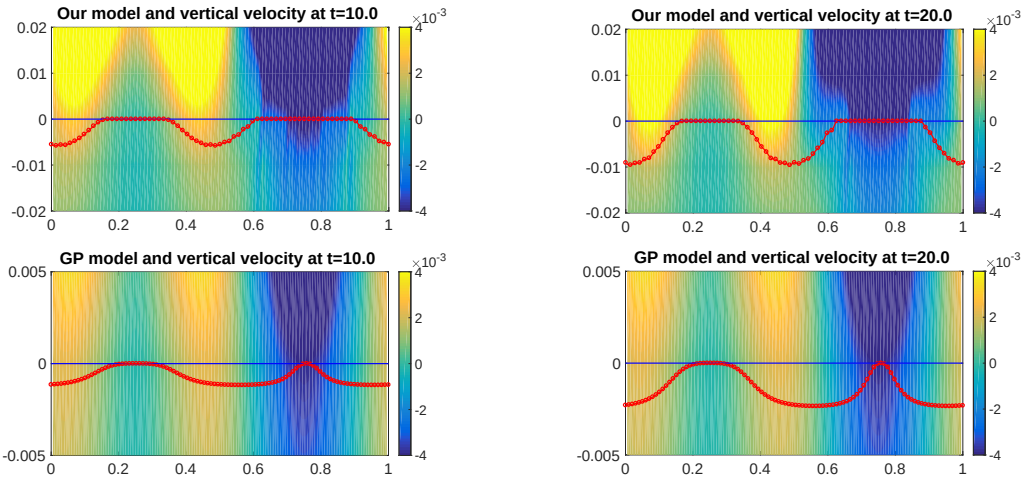

Figure 5.13: The dynamic interface for swirling flow is depicted at different times for our model versus GP model. The parameters used are $Re = 600$, $Da = 5 \times 10^{-5}$, promoting erosion at a relatively fast rate. For comparison the original interface is shown as well in solid blue.

Both models predict similar locations of erosion maxima and minima. The erosion for our model is more focused and it can be observed that at $t = 20$, the flow penetrates deeper into the sand at locations where the interface has been displaced. A significant difference between the two models is the four times higher erosion rate for our model compared to the GP model. The main reason is that the normalized flux for the GP model never exceeds 0.3 because of a saturation mechanism. We deliberately chose our parameters to promote erosion at a higher rate to reduce computational times, and as a result the saturation of the GP model is emphasized. We note that our model predicts much less erosion underneath the area where the flow is mostly downward. Stresses generated in this region are large enough to generate erosion in the GP model, but because the flow pushes particles downward into the deposit, our model does not predict any erosion.

The next application we explored is the hill flow profile depicted in figure 5.14. The interaction of flow with the sand profile is visible as the erosion continues until the hill is flattened. The flow conditions are identical to our fixed interface simulations.

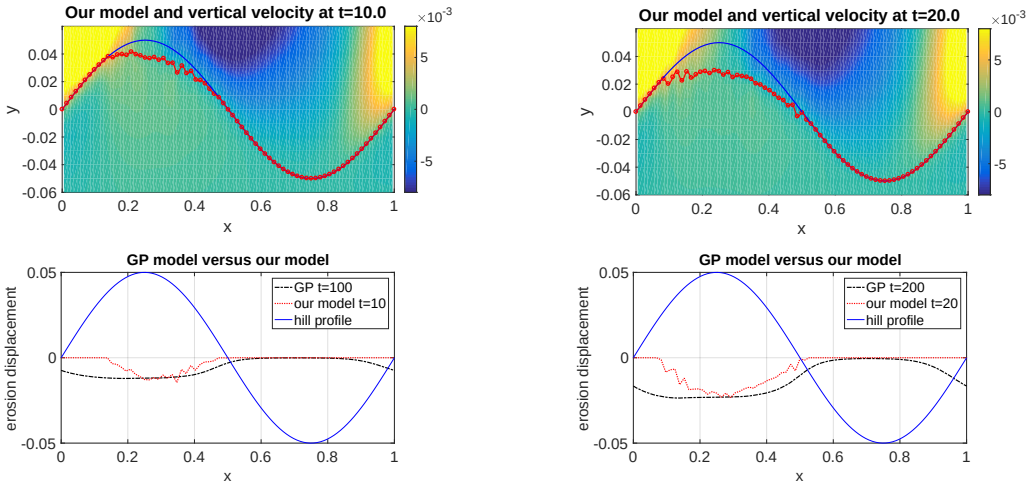

Figure 5.14: Dynamic interface for hill flow depicted at different times for our model and the GP model. The parameters used are $Re = 600$, $Da = 5 \times 10^{-5}$, promoting erosion at a relatively fast rate. For comparison the original interface is shown as well in solid blue.

Both models predict erosion over the hill portion of the profile with the maximum near the peak. The GP model is predicting erosion over slightly larger area including the entire raised section while our model is more focused around the peak of the hill. The intensity of erosion is many times larger for our model again due to the saturation mechanism for the GP model. It can be observed that the interface becomes more horizontal as the peak of the hill slowly flattens out.

5.6 Summary

We applied our new numerical method discussed in chapter 4 on two different erosion applications; swirling flow and hill flow. We computed the erosion flux using the fluid velocity at the interface and compared our results with an empirical erosion model (Garcia-Parker) based on the tangential stress. Both models predict increased erosion rate for higher Re, zeta and smaller particle size. The GP model does not respond to porosity changes while our model indicates a strong increase of the erosion rate for higher porosity.

Next, we simulated the swirling flow and hill flow profiles with a mobile interface. The parameters are selected such that erosion is promoted at a fast rate. The interface alteration for our model correlates well with the GP model. We noted that the impact of the GP model is broader while its erosion rate is slower mainly because of the flux saturation. Our model is strongly correlated to the vertical velocities at the interface and predicts less erosion if the upward fluid velocity is weak. The GP model predicts erosion in locations along the interface where the stress is high although the fluid velocity is mostly pushing down into the sand. This explains the broader nature of erosion in GP model compared to ours.

Chapter 6

Conclusion

In this dissertation, we have studied the interaction of fluid with porous media in different environments. First, we investigated the settling of a porous spherical particle in density stratified fluid to understand the mechanisms behind marine snow aggregation in the ocean. We successfully determined a relationship between settling delay and quantities pertinent to the characteristics of the particle and the ambient fluid. Next, we developed a new numerical method for accurate and flexible porous-fluid simulations. This method is applicable to any geometry and can easily handle a mobile interface. Lastly, we applied this method on two erosion applications where fluid is flowing over sandy deposits of different shapes. We quantified the suspension rate of the sand particles into the fluid and observed the deformation of the interface. The novel idea in our method is that erosion is derived from the fluid velocity along the interface and may not require an empirical constant.

Systems with fluid flow through domains that are partially porous are relevant in many applications in geology, biology, medicine and bioengineering. The governing equations describing these systems can not be solved analytically in most cases. Therefore the most efficient approach is to analyze them by means of simulations. In our settling application, we quantified the settling delay of a porous particle in density stratified ambient with respect to the most important parameters of the system. While the parameter regime was too large to explore entirely, we quantified the effects of each parameter when varied individually. It remains to be confirmed that the quantitative effects described here are the same when several parameters are varied simultaneously. We intend to explore this in our future research.

The marine snow settling results presented here make use of two significant idealizations compared to real oceanographic systems. First, we considered a spherical particle, while marine snow is notoriously irregular in shape. To make use of our results, an effective radius may be identified to describe a real particle, particularly in the linear regime prevailing at low Reynolds numbers. It is possible, however, that the best effective radius to describe the fluid flow differs from the best effective radius to describe diffusive effects. Slender and spiky particles may entrain a volume of fluid dictated by the size of the convex hull encompassing them, while diffusive time scale tend to depend on the smallest length scale of the particle. A systematic study of the proper manner in which to characterize the size and shape of marine snow remains to be undertaken. A second important effect to consider in future research is that of the combined effects of several porous particles settling together. The study of sedimentation of solid particles has revealed particularly complex dynamics when large number of particles settle together [104, 105]. Even if these particles are localized and act as a cloud, [106, 107], the long term dynamics in a stratified ambient are complicated by the entrainment of ambient fluid. We anticipate the fluid entrained by a thermal or cloud of marine snow

to be even more determinant in the dynamics of clusters of porous particles than it is for clusters of solid particles.

In Chapter 4, we introduced a new numerical method for flow in fluid-porous applications with a mobile interface. We have successfully demonstrated the usefulness of our numerical method for simulation of different erosion applications. Our numerical scheme is robust and ideal for complex flows interacting with a porous medium. Although our method is missing the bedload transport mechanism, obtained results are still strongly correlated to the well recognized Garcia-Parker (GP) model [23]. We were able to analyze the sand profile together with the detailed flow conditions inside the porous region. Currently, the main disadvantage of our method is the computational cost required for each time step. For more efficient simulations, our numerical solver must be complemented with non-uniform grid refinement and parallel computation capabilities. In addition, we would like to add a variable density function to our Navier-Stokes solver coupled with the advection-diffusion equation used to track a soluble agent concentration (like salt). With these additions, one would be able to explore the spread of pollutants in situations where water flows over contaminated porous media.

An accurate description of the flow within and above a porous deposit can provide practical information about the spread of contaminants and pollutants in the ground caused by rain or flooding. Pollution of our water resources is a major concern for highly sensitive ecosystems, with serious health consequences [71]. Our method is well suited to track the concentration of contaminants removed from the soil. The interaction of vortices, both within and above the deposit, and contaminants is of special interest and provide a more complete description of contaminant transport. Our simulations showed that vortices may form inside the porous media beneath a swirling flow. We detected that vortices grow in size and strength with higher Re, eventually penetrating the fluid domain. A better understanding of the dominant transport mechanism may be useful to control and reduce the spread of pollutants.

In many applications where a concentration of suspended particles is transported by the fluid and particles may be deposited or eroded, the use of a mobile interface is an essential requirement. Our numerical method may easily incorporate this feature. In the present study, we focused on the onset of erosion and simulated the flow of water over different profiles of sandy deposits. The trigger for erosion in our model is based on whether the normal fluid velocity exceeds the particle settling velocity in contrast to the traditional way where an empirical model based on stress is used. Our results were consistent with ones obtained based on the GP model and predicted increasing erosion flux with higher Re, slip coefficient ζ and smaller particle size d. In addition, as our method is specifically targeting resuspension, the erosion is triggered at higher Re compared with the GP approach, which includes some bed-load transport [98]. In contrast to traditional fluid solvers where no-slip boundary conditions are applied, our method can provide the velocities within the porous medium and fluid, and can therefore capture differences due to variations in the porous medium. Our model thus predicted higher erosion for higher porosity, while the GP model showed no significant change.

The erosion model proposed here can be further refined, for example by including adhesion forces for smaller particles. To do so, we have introduced a parameter α, currently set to one, which allows the flexibility to take this into consideration. Moreover, for higher Re, as the interface normal velocities increase, the erosion flux should eventually become saturated. As the erosion flux increases, a deeper layer of particles below the interface will be affected and hence the effective normal velocity should be evaluated at a level below the interface. The level where the velocity is evaluated could therefore be correlated to the particle flux, for example by considering the flux from a previous time step. This is consistent with the GP model where erosion is saturated having maximum $F_{GP} = 0.3$. Further, one could include a mechanism accounting for rolling and bed-load

transport that occur at lower Re [108]. Accounting for the flow within a fixed porous deposit lays the ground for further exploration of how a porous matrix may be moved by its interstitial flow, as is the case in many erosive flows. If the porous matrix moves, the Brinkman equations still allow the determination of the fluid velocity relative to it. Computing how to move the porous matrix itself would require empirical models or detailed granular material simulations. The latter problem is particularly difficult to model, but obtaining an accurate description of the flow within the porous medium is an important step toward a useful representation of mobile porous matrices.

Appendix A

A.1 Implicit Navier-Stokes solver

A.1.1 Advection equation

We solve the advection equation on a 2D staggered grid using Adams-Bashforth2 for time integration and central differences for spatial discretization.

$$\frac{\partial \vec{u}}{\partial t} = -\vec{u} \cdot \nabla u + \vec{f} \tag{A.1}$$

$\vec{u}$ represents fluid velocity and $\vec{f}$ is an external body force. Equation A.1 is split into horizontal and vertical components,

$$u_t = -uu_x - vu_y + f_1 \quad \text{solved on u-grid} \tag{A.2}$$
$$v_t = -uv_x - vv_y + f_2 \quad \text{solved on v-grid} \tag{A.3}$$

where u and f_1 denote velocity and force in x-direction and v and f_2 the velocity and force in y-direction. We rewrite the spatial derivatives using finite difference approximation. The differential operators are written in matrix form and applied to discretized variables.

$$u_x = D_x^u U + C_1$$
$$u_y = D_y^u U + C_8$$
$$V^u = M^{v \to u} V + C_{16}$$

$$v_x = D_x^v V + C_3$$
$$v_y = D_y^v V + C_{10}$$
$$U^v = M^{u \to v} U + C_{15}$$

U and V are discrete velocites in horizontal and vertical directions. They reside on different grid points implied by our use of a MAC grid. M operator is used to evaluate a discrete variable on a different grid. D represents a central difference operator and C contains boundary information.

Next, we apply the AB2 scheme (Adams-Bashforth2) to PDEs A.2 and A.3.

$$\begin{aligned}
\frac{\partial \vec{u}}{\partial t} &= -\vec{u}\cdot\nabla u + \vec{f} \quad \Rightarrow \quad \text{in x-direction} \\
u_t &= -uu_x - vu_y + f_1 = f(u) \\
\{AB2\} \quad \Rightarrow U^{n+2} &= U^{n+1} + \frac{\Delta t}{2}\Big(- f(U^n) + 3f(U^{n+1})\Big) \quad \text{where} \\
f(U^n) &= -U^n\ (D_x^u U^n + C_1^n) - (M^{v\to u}V^n + C_{16}^n)\ (D_y^u\ U^n + C_8^n) + f_1^n
\end{aligned}$$

$$\begin{aligned}
\frac{\partial \vec{u}}{\partial t} &= -\vec{u}\cdot\nabla u + \vec{f} \quad \Rightarrow \quad \text{in y-direction} \\
v_t &= -uv_x - vv_y + f_2 = f(v) \\
\{AB2\} \quad \Rightarrow V^{n+2} &= V^{n+1} + \frac{\Delta t}{2}\Big(- f(V^n) + 3f(V^{n+1})\Big) \quad \text{where} \\
f(V^n) &= (-M^{u\to v}U^n + C_{15}^n)\ (D_x^v V^n + C_3^n) - V^n(D_y^v\ V^n + C_{10}^n) + f_2^n
\end{aligned}$$

A.1.2 Heat equation

We solve the heat equatioin on a MAC grid using Crank-Nicholson scheme. We followe the same procedure as the advection equation. The heat equation is broken into horizontal and vertical components and discretized.

$$\frac{\partial \vec{u}}{\partial t} = \mu\nabla^2\vec{u} \quad \Rightarrow \tag{A.4}$$

$$u_t = \mu(u_{xx} + u_{yy}) \tag{A.5}$$

$$v_t = \mu(v_{xx} + v_{yy}) \tag{A.6}$$

$$\begin{aligned}
u_{xx} &= D_{xx}^u\ u + C_2 \\
v_{xx} &= D_{xx}^v\ v + C_4 \\
u_{yy} &= D_{yy}^u\ u + C_9 \\
v_{yy} &= D_{yy}^v\ v + C_{11}
\end{aligned}$$

$$\begin{aligned}
\frac{\partial \vec{u}}{\partial t} &= \mu\nabla^2\vec{u} \quad \Rightarrow \\
u_t &= \mu(u_{xx} + u_{yy}) \quad \Rightarrow \quad \{Crank - Nicholson\} \quad \Rightarrow \\
U^{n+1} &= U^n + \frac{\Delta t\mu}{2}\Big((D_{xx}^u + D_{yy}^u)U^n + C_2^n + C_9^n + (D_{xx}^u + D_{yy}^u)U^{n+1} + C_2^{n+1} + C_9^{n+1}\Big) \quad \Rightarrow \\
U^{n+1} &= \Big[I - \frac{\Delta t\mu}{2}(D_{xx}^u + D_{yy}^u)\Big]^{-1}\left(\Big[I + \frac{\Delta t\mu}{2}(D_{xx}^u + D_{yy}^u)\Big]U^n + \frac{\mu\Delta t}{2}(C_2^n + C_9^n + C_2^{n+1} + C_9^{n+1})\right)
\end{aligned}$$

$$\begin{aligned}
\text{If} \quad A^u &= I - \frac{\Delta t\mu}{2}(D_{xx}^u + D_{yy}^u) \quad \Rightarrow \\
U^{n+1} &= [A^u]^{-1}\left(\Big[I + \frac{\Delta t\mu}{2}(D_{xx}^u + D_{yy}^u)\Big]U^n + \frac{\mu\Delta t}{2}(C_2^n + C_9^n + C_2^{n+1} + C_9^{n+1})\right)
\end{aligned} \tag{A.7}$$

$$
\begin{aligned}
v_t &= \mu(v_{xx} + v_{yy}) \quad \Rightarrow \quad \{Crank - Nicholson\} \quad \Rightarrow \\
V^{n+1} &= V^n + \frac{\Delta t \mu}{2}\Big((D^v_{xx} + D^v_{yy})V^n + C^n_4 + C^n_{11} + (D^v_{xx} + D^v_{yy})V^{n+1} + C^{n+1}_4 + C^{n+1}_{11}\Big) \quad \Rightarrow \\
V^{n+1} &= \Big[I - \frac{\Delta t \mu}{2}(D^v_{xx} + D^v_{yy})\Big]^{-1}\left(\Big[I + \frac{\Delta t \mu}{2}(D^v_{xx} + D^v_{yy})\Big]V^n + \frac{\mu \Delta t}{2}(C^n_4 + C^n_{11} + C^{n+1}_4 + C^{n+1}_{11})\right) \\
\text{If} \quad A^v &= I - \frac{\Delta t \mu}{2}(D^v_{xx} + D^v_{yy}) \quad \Rightarrow \\
V^{n+1} &= [A^v]^{-1}\left(\Big[I + \frac{\Delta t \mu}{2}(D^v_{xx} + D^v_{yy})\Big]V^n + \frac{\mu \Delta t}{2}(C^n_4 + C^n_{11} + C^{n+1}_4 + C^{n+1}_{11})\right) \qquad \text{(A.8)}
\end{aligned}
$$

A.1.3 Navier-Stokes equations

We solve the full Navier-Stokes equation using finite differences on a MAC grid. We use Adams-Bashforth2 scheme for time integration of the advection part and Crank-Nicholson for the diffusive part. We obtian the updated velocities, U^* and V^* by ignoring the pressure term. Lastly, we use the projection method to solve for pressure.

$$
\begin{aligned}
\frac{\partial \vec{u}}{\partial t} &= -\vec{u}\cdot\nabla u + \vec{f} + \frac{1}{Re}\nabla^2\vec{u} - \nabla p \quad \Rightarrow \quad \text{in x-direction} \\
u_t &= -uu_x - vu_y + f_1 + \frac{1}{Re}(u_{xx}+u_{yy}) - p_x \quad \{AB2 \ \& \ CN\} \quad \Rightarrow \qquad (A.9) \\
U^{(n+2)} &= U^{n+1} + \frac{\Delta t}{2}\Big(- conv^n + 3\ conv^{n+1}\Big) \\
&+ \frac{\Delta t}{2Re}\Big((D^u_{xx}+D^u_{yy})U^{n+1} + C_2^{n+1} + C_9^{n+1} + (D^u_{xx}+D^u_{yy})U^{n+2} + C_2^{n+2} + C_9^{n+2}\Big) \\
&- \Delta t(D^u_x P^{n+1} + C_6^{n+1}) \\
&= \Big[I - \frac{\Delta t}{2Re}(D^u_{xx}+D^u_{yy})\Big]^{-1}\Bigg(\Big[I + \frac{\Delta t}{2Re}(D^u_{xx}+D^u_{yy})\Big]U^{n+1} + \frac{\Delta t(C_2^{n+1}+C_9^{n+1}+C_2^{n+2}+C_9^{n+2})}{2Re} \\
&+ \frac{\Delta t}{2}\Big(- conv^n + 3\ conv^{n+1}\Big) - \Delta t(D^u_x P^{n+1} + C_6^{n+1})\Bigg)
\end{aligned}
$$

where,

$$
conv^n = \Big(- U^n\ (D^u_x U^n + C_1^n) - (M^{v\to u}V + C_{16}^n)\ (D^u_y\ U^n + C_8^n) + f_1^n\Big).
$$

$$
\begin{aligned}
\text{If} \quad A^u &= I - \frac{\Delta t\mu}{2}(D^u_{xx}+D^u_{yy}) \quad \Rightarrow \\
U^{(n+2)} &= [A^u]^{-1}\Bigg(\Big[I + \frac{\Delta t}{2Re}(D^u_{xx}+D^u_{yy})\Big]U^{n+1} + \frac{\Delta t(C_2^{n+1}+C_9^{n+1}+C_2^{n+2}+C_9^{n+2})}{2Re} \\
&+ \frac{\Delta t}{2}\Big(- conv^n + 3\ conv^{n+1}\Big)\Bigg) - \Delta t[A^u]^{-1}(D^u_x P^{n+1} + C_6^{n+1}) \\
&= U^{*(n+2)} - \Delta t[A^u]^{-1}(D^u_x P^{n+1} + C_6^{n+1}) \qquad (A.10)
\end{aligned}
$$

where,

$$
\begin{aligned}
U^{*(n+2)} &= [A^u]^{-1}\Bigg(\Big[I + \frac{\Delta t}{2Re}(D^u_{xx}+D^u_{yy})\Big]U^{n+1} + \frac{\Delta t(C_2^{n+1}+C_9^{n+1}+C_2^{n+2}+C_9^{n+2})}{2Re} \\
&+ \frac{\Delta t}{2}\Big(- conv^n + 3\ conv^{n+1}\Big)\Bigg) \qquad (A.11)
\end{aligned}
$$

$$
\begin{aligned}
\frac{\partial \vec{u}}{\partial t} &= -\vec{u}\cdot\nabla u + \vec{f} + \frac{1}{Re}\nabla^2\vec{u} - \nabla p \quad \Rightarrow \quad \text{in y-direction} \\
v_t &= -uv_x - vv_y + f_2 + \frac{1}{Re}(v_{xx}+v_{yy})) - p_y \quad \{AB2\ \&\ CN\} \quad \Rightarrow \qquad (A.12) \\
V^{(n+2)} &= V^{n+1} + \frac{\Delta t}{2}\Big(- conv^n + 3\ conv^{n+1}\Big) \\
&+ \frac{\Delta t}{2Re}\Big((D^v_{xx}+D^v_{yy})V^{n+1} + C_4^{n+1} + C_{11}^{n+1} + (D^v_{xx}+D^v_{yy})V^{n+2} + C_4^{n+2} + C_{11}^{n+2}\Big) \\
&- \Delta t(D^v_y P^{n+1} + C_{13}^{n+1}) \\
&= \Big[I - \frac{\Delta t}{2Re}(D^v_{xx}+D^v_{yy})\Big]^{-1}\Bigg(\Big[I + \frac{\Delta t}{2Re}(D^v_{xx}+D^v_{yy})\Big]V^{n+1} + \frac{\Delta t(C_4^{n+1}+C_{11}^{n+1}+C_4^{n+2}+C_{11}^{n+2})}{2Re} \\
&+ \frac{\Delta t}{2}\Big(- conv^n + 3\ conv^{n+1}\Big) - \Delta t(D^v_y P^{n+1} + C_{13}^{n+1})\Bigg)
\end{aligned}
$$

where,

$$
conv^n = \Big(- (M^{u\to v}U^n + C_{15}^n)\ (D^v_x V^n + C_3^n) - V^n\ (D^v_y\ V^n + C_{10}^n) + f_2^n\Big) \quad \Rightarrow
$$

$$
\begin{aligned}
\text{If} \quad A^v &= I - \frac{\Delta t}{2Re}(D^v_{xx}+D^v_{yy}) \quad \Rightarrow \\
V^{(n+2)} &= [A^v]^{-1}\Bigg(\Big[I + \frac{\Delta t}{2Re}(D^v_{xx}+D^v_{yy})\Big]V^{n+1} + \frac{\Delta t(C_4^{n+1}+C_{11}^{n+1}+C_4^{n+2}+C_{11}^{n+2})}{2Re} \\
&+ \frac{\Delta t}{2}\Big(- conv^n + 3\ conv^{n+1}\Big)\Bigg) - \Delta t[A^v]^{-1}(D^v_y P^{n+1} + C_{13}^{n+1}) \\
&= V^{*(n+2)} - \Delta t[A^v]^{-1}(D^v_y P^{n+1} + C_{13}^{n+1}) \qquad (A.13)
\end{aligned}
$$

where,

$$
\begin{aligned}
V^{*(n+2)} &= \Big[A^v\Big]^{-1}\Bigg(\Big[I + \frac{\Delta t}{2Re}(D^v_{xx}+D^v_{yy})\Big]V^{n+1} + \frac{\Delta t(C_4^{n+1}+C_{11}^{n+1}+C_4^{n+2}+C_{11}^{n+2})}{2Re} \\
&+ \frac{\Delta t}{2}\Big(- conv^n + 3\ conv^{n+1}\Big)\Bigg). \qquad (A.14)
\end{aligned}
$$

AB2 scheme is a multi-step method and requires the two previous time steps. We use forward Euler for our first time stepping.

$$
\begin{aligned}
U^{*1} &= U^0 + \Delta t\Big(- U^0\ (D^u_x U^0 + C_1^0) - (M^{v\to u}V^0 + C_{16}^0)\ (D^u_y\ U^0 + C_8^o) + f_1^0 + (D^u_{xx}+D^u_{yy})U^0 + C_2^0 + C_9^0\Big) \\
V^{*1} &= V^0 + \Delta t\Big(- (M^{u\to v}U^0 + C_{15}^0)\ (D^v_x V^0 + C_3^0) - V^0\ (D^v_y\ V^0 + V_{10}^0) + f_2^0 + (D^v_{xx}+D^v_{yy})V^0 + C_4^0 + C_{11}^0\Big)
\end{aligned}
$$

The pressure P^{n+1} can be obtained by utilizing that the velocity for incompressible flow is divergence free (projection method).

$$
\begin{aligned}
U^{n+2} &= U^{*(n+2)} - \Delta t[A^u]^{-1}(D^u_x P^{n+1} + C_6^{n+1}) \qquad (A.15) \\
V^{n+2} &= V^{*(n+2)} - \Delta t[A^v]^{-1}(D^v_y P^{n+1} + C_{13}^{n+1}) \qquad (A.16)
\end{aligned}
$$

$$
\begin{aligned}
\Rightarrow \quad U_x^{*(n+2)} + V_y^{*(n+2)} &= \Delta t\Big(D_x^p[A^u]^{-1}(D_x^u P^{n+1} + C_6^{n+1}) + C_7^{n+1}\Big) \\
&+ \Delta t\Big(D_y^p[A^v]^{-1}(D_y^v P^{n+1} + C_{13}^{n+1}) + C_{14}^{n+1}\Big) \\
\Rightarrow \quad \Big(D_x^p[A^u]^{-1}D_x^u + D_y^p[A^v]^{-1}D_y^v\Big)P^{n+1} &= \frac{U_x^{*(n+2)} + V_y^{*(n+2)}}{\Delta t} \\
&- C_7^{n+1} - C_{14}^{n+1} - D_x^p[A^u]^{-1}C_6^{n+1} - D_y^p[A^v]^{-1}C_{13}^{n+1} \\
\Rightarrow \quad A\ P^{n+1} &= b \qquad \text{(A.17)}
\end{aligned}
$$

The pressure is obtained by solving the linear system A.17. This linear system can be solved directly or by using an iterative method. Iterative methods are preferred for higher resolutions when the memory resources are limited.

A.2 Brinkman equations

We solve the non-dimensional Brinkman equations numerically using finite differeces on a MAC grid. We use cetral difference operators to approximate our spatial derivatives. The velocity is divergence free because of the incompressibility of the fluid. We use projection method to solve for pressure similar to the Navier-Stokes equations.

$$
\begin{aligned}
\frac{1}{Da \cdot Re}\vec{u} &= \nabla \cdot -p\bar{I} + \frac{1}{\beta \cdot Re}\nabla^2\vec{u} + \vec{f} \quad \Rightarrow & \text{(A.18)} \\
\frac{1}{Da \cdot Re}u &= -p_x + \frac{1}{\beta \cdot Re}(u_{xx} + u_{yy}) + f_1 & \text{(A.19)} \\
\frac{1}{Da \cdot Re}v &= -p_y + \frac{1}{\beta \cdot Re}(v_{xx} + v_{yy}) + f_2 & \text{(A.20)}
\end{aligned}
$$

$$
\begin{aligned}
u_{xx} &= D_{xx}^u\ U + C_2 \\
u_{yy} &= D_{yy}^u\ U + C_9 \\
v_{xx} &= D_{xx}^v\ V + C_4 \\
v_{yy} &= D_{yy}^v\ V + C_{11} \\
p_x &= D_x^u\ P + C_6 \\
p_y &= D_y^v\ P + C_{13}
\end{aligned}
$$

$$
\Big[\frac{1}{Da \cdot Re}\bar{\bar{I}} - \frac{D_{xx}^u + C_2 + D_{yy}^u + C_9}{\beta \cdot Re}\Big]U = -(D_x^u P + C_6) + f_1 \qquad \text{(A.21)}
$$

$$
\text{if } A = \Big[\frac{1}{Da \cdot Re}\bar{\bar{I}} - \frac{D_{xx}^u + C_2 + D_{yy}^u + C_9}{\beta \cdot Re}\Big] \Rightarrow
$$

$$
U = -A^{-1}(D_x^u P + C_6) + U^* \qquad \text{(A.22)}
$$

$$
\text{where, } U^* = A^{-1}f_1
$$

$$
\Big[\frac{1}{Da \cdot Re}\bar{\bar{I}} - \frac{D_{xx}^v + C_4 + D_{yy}^v + C_{11}}{\beta \cdot Re}\Big]V = -(D_y^v P + C_{13}) + f_2 \qquad \text{(A.23)}
$$

$$
\text{if } B = \Big[\frac{1}{Da \cdot Re}\bar{\bar{I}} - \frac{D_{xx}^v + C_4 + D_{yy}^v + C_{11}}{\beta \cdot Re}\Big] \Rightarrow
$$

$$
V = -B^{-1}(D_y^v P + C_{13}) + V^* \qquad \text{(A.24)}
$$

$$
\text{where, } V^* = B^{-1}f_2
$$

$$\nabla \cdot \vec{u} = 0 \quad \Rightarrow \tag{A.25}$$
$$U_x + V_y = 0 \quad \Rightarrow$$
$$D_x^p\big(- A^{-1}(D_x^u P + C_6) + U^*\big) + C_7 + D_y^p\big(- B^{-1}(D_y^v P + C_{13}) + V^*\big) + C_{14} = 0 \quad \Rightarrow$$
$$\big[D_x^p A^{-1} D_x^u + D_y^p B^{-1} D_y^v\big] P = D_x^p(-U^* + A^{-1}C_6) + D_y^p(-V^* + B^{-1}C_{13}) - C_7 - C_{14} \quad \Rightarrow$$
$$P = \big[D_x^p A^{-1} D_x^u + D_y^p B^{-1} D_y^v\big]^{-1}\big[D_x^p(-U^* + A^{-1}C_6) + D_y^p(-V^* + B^{-1}C_{13}) - C_7 - C_{14}\big]$$

$$U = -A^{-1} D_x^u P + U^* \tag{A.26}$$
$$V = -B^{-1} D_y^v P + V^* \tag{A.27}$$

A.3 Mixed domain pipe flow with infinite porous depth

In this derivation for pipe flow we assume horizontal flow and constant pressure gradient. u the horizontal velocity is fixed at top boundary and the flow is periodic in x direction. The fluid height is D and the porous medium is infinite. The flow starts from rest and approaches steady-state as $t \to \infty$. These assumptions are used to simplify the non-dimensionalized governing equations (4.5). The Initial Boundary Value problem for our pipe flow becomes much simpler as the nonlinear convective terms disappear. This leaves, in the fluid

$$\frac{\partial u_f}{\partial t} = -\nabla p + \frac{1}{Re}\frac{\partial^2 u_f}{\partial y^2}$$

and in the porous medium

$$\frac{1}{Da\ Re} u_p = -\nabla p + \frac{1}{\beta Re}\frac{\partial^2 u_p}{\partial y^2}.$$

The boundary conditions at the walls are

$$\begin{aligned} u_f(y = D) &= u_{top} \\ u_p(y \to -\infty) &= -G\ Re\ Da \end{aligned}$$

and along the interface

$$\begin{aligned} u_f &= u_p \\ \tfrac{\partial u_f}{\partial y} &= \frac{1}{\beta}\frac{\partial u_p}{\partial y} + \frac{\zeta}{\sqrt{Da}} u_p \end{aligned} \tag{A.28}$$

where the second boundary condition is the steady-state flow caused in the porous medium by a pressure gradient G. The analytical solution for velocity in the fluid region, u_f and the porous region

u_p is expressed below.

$$
\begin{aligned}
u_f &= \frac{G\ Re}{2}y^2 + Ay + B + \sum_{n=1}^{\infty} A_n \ \ \sin\left[k_n(y-D)\right]e^{-\frac{k_n^2}{Re}t} \qquad \text{(A.29)}\\
u_p &= Ce^{\sqrt{\frac{\beta}{Da}}y} - G\ Re\ Da + \sum_{n=1}^{\infty} B_n\ e^{\sqrt{\frac{\beta}{Da}}y}\\
A &= \frac{1}{\sqrt{\beta Da}}C + \frac{\zeta}{\sqrt{Da}}B\\
B &= C - G\ Re\ Da\\
C &= \frac{u_{top} - \frac{G\ Re}{2}D^2 + G\ Re\ Da + D\ \zeta\ Re\ G\sqrt{Da}}{1 + \frac{D}{\sqrt{\beta Da}} + \frac{D\zeta}{\sqrt{Da}}}\\
k_n &= -\frac{1/\sqrt{\beta} + \zeta}{\sqrt{Da}}tan(k_n D) \quad \text{and,}\\
A_n &= \frac{\frac{-G\ Re\ D^2}{2k_n} + \left(\frac{2G\ Re}{k_n^3} - \frac{2B}{k_n}\right)\ \sin^2(\frac{Dk_n}{2}) + \frac{A}{k_n^2}\sin(Dk_n) - \frac{AD}{k_n}}{\frac{D}{2} - \frac{\sin(2Dk_n)}{4k_n}}\\
B_n &= -A_n e^{-\frac{k_n^2}{Re}t}\sin(Dk_n)
\end{aligned}
$$

The solution is as expected a combination of a transient part slowly dying away and a constant steady-state. There is no analytical solution for eigenvalues k_n and hence they must be obtained numerically. Fortunately only a handful of them are required to obtain an accurate solution. If an accuracy of 10^{-15} is required for the analytical solution, we have:

$$
\begin{aligned}
e^{-\frac{k_n^2}{Re}t} &< 10^{-15}\\
k_n &> \sqrt{-\ln(10^{-15})\frac{Re}{t}}\\
k_n &> 6\sqrt{\frac{Re}{t}} \qquad \text{(A.30)}
\end{aligned}
$$

A.4 Mixed domain pipe flow with finite porous depth

The steady-state analytical solution when the porous thickness is finite has been derived as well and used in our simulations. For a fluid height D and a porous medium thickness L, the simplified Navier-Stokes and Brinkman equations and the known boundary conditions yield the boundary value problem below. The differential equations in the fluid and porous medium are

$$
\begin{aligned}
0 &= -\nabla p + \frac{1}{Re}\frac{\partial^2 u_f}{\partial y^2}\\
\frac{1}{Da\ Re}u_p &= -\nabla p + \frac{1}{\beta Re}\frac{\partial^2 u_p}{\partial y^2}
\end{aligned}
$$

with boundary conditions at the walls

$$
\begin{aligned}
u_f(y = D) &= 0 \qquad \text{(A.31)}\\
u_p(y = -L) &= 0 \qquad \text{(A.32)}
\end{aligned}
$$

and along the interface

$$u_f = u_p \tag{A.33}$$

$$\frac{\partial u_f}{\partial y} = \frac{1}{\beta}\frac{\partial u_p}{\partial y} + \frac{\zeta}{\sqrt{Da}}u_p. \tag{A.34}$$

The solution to the above BVP for velocity in the fluid, u_f is

$$u_f = \frac{G\ Re}{2}(y-D)(y+\delta) \quad \text{where,} \tag{A.35}$$

$$\delta = \frac{2Da^2 + \beta^{3/2}D\sqrt{Da}}{D\ Da + \beta^{3/2}D\zeta + \beta^{3/2}\sqrt{Da}} \tag{A.36}$$

and the solution for the velocity in the porous medium u_p is

$$u_p = A\ \cosh\Big(\sqrt{\frac{Da}{\beta}}(y+L)\Big) + B\ sinh\Big(\sqrt{\frac{Da}{\beta}}(y+L)\Big) - Da\ G\ Re \tag{A.37}$$

$$A = Da\ G\ Re \quad \text{and}$$

$$B = \frac{G\ Re\Big(\beta D\zeta\sqrt{Da} + \beta Da - D^2\beta/2\Big) - G\ Re\ \cosh(L\sqrt{\frac{Da}{\beta}})\Big(\beta Da - D\sqrt{\frac{Da}{\beta}}Da + \beta D\zeta\sqrt{Da}\Big)}{\sinh(L\sqrt{\frac{Da}{\beta}})\Big(\beta + D\sqrt{\frac{Da}{\beta}} + \frac{\beta D\zeta}{\sqrt{Da}}\Big)}.$$

Bibliography

[1] R. Camassa, S. Khatri, R. M. McLaughlin, J. C. Prairie, B. L. White, and S. Yu. Retention and entrainment effects: Experiments and theory for porous spheres settling in sharply stratified fluids. *Physics of Fluids*, 25:081701, 2013.

[2] M. Eckert. *The Dawn of Fluid Dynamics: A Discipline Between Science and Technology.* Wiley, 2006.

[3] J.D. Anderson. *Fundamentals of Aerodynamics.* McGrawHill, 4 edition, 2007.

[4] F. M. White. *viscous Fluid Flow.* McGrawHill, 1974.

[5] D. A. Nield and Bejan. A. *Convection in Porous Media.* 2006.

[6] Mark E. Davis. Ordered porous materials for emerging applications. *Nature*, 417:813–821, 2002.

[7] S. Whitaker. *Flow in porous media I: A theoretical derivation of Darcys law.* 1986.

[8] D. D. Joseph, D. A. Nield, and Papanicolagou G. Nonlinear equation governing flow in a saturated porous medium. *Water Recourses Research*, 18(4):1049–1052, 1982.

[9] Bert Olin, E. T. Degens, S. Kempe, and P. Ketner. *Flow in porous media I: A theoretical derivation of Darcys law.* Wiley, 1979.

[10] E. Y. Dwon, F. Primeau, and J. L. Sarmiento. The impact of remineralization depth on the air-sea carbon balance. *Oceanography*, 2:813–821, 2009.

[11] Durham W. M. and R. Stocker. Thin phytoplankton layers: characteristics, mechanisms, and consequences. *Annu. Rev. Mar. Sci.*, 4:177–207, 2012.

[12] O.M. Cheriton, M.A. McManus, M.T. Stacey, and Steinbuck J.V. Physical and biological controls on the maintenance and dissipation of a thin phytoplankton layer. *Mar. Ecol. Prog. Ser.*, 378:55–69, 2009.

[13] Durham W. M., J. O. Kessler, and R. Stocker. Thin phytoplankton layers: characteristics, mechanisms, and consequences. *Science*, 323:1067–1070, 2009.

[14] Nicole Abaid, David Adalsteinsson, Akua Agyapong, and Richard M. McLaughlin. An internal splash: Levitation of falling spheres in stratified fluids. *Phys. Fluids*, 16(5):1567–1580, 2004.

[15] Roberto Camassa, Claudia Falcon, Joyce Lin, Richard M. McLaughlin, and Ricahrd Parker. Prolonged residence times for particles settling through stratified miscible fluids in the stokes regime. *Phys. Fluids*, 21:031702, 2009.

[16] Kolja Kindler, Arzhang Khalili, and Roman Stocker. Diffusion-limited retention of porous particles at density interfaces. *Proc. Natl. Acad. Sci. U.S.A.*, 107(51):22163–22168, 2010.

[17] R. L. Burden and J. D. Faires. *Numerical Analysis*. Brooks/Cole, Cengage Learning, 2011.

[18] R. Eymard, Gallouet T. R., and R. Herbin. *The finite volume method Handbook of Numerical Analysis*, volume VII. 2000.

[19] C.W. Hirt and B.D. Nichols. Volume of fluid (vof) method for the dynamics of free boundaries. *Journal of Computational Physics*, 39(1):201225, 1981.

[20] Hubert Chanson. *The Hydraulics of Open Channel Flow: An Introduction*. 2004.

[21] M. Cheraghi, S Jomaa, G. C. Sander, and D. A. Barry. Hysteretic sediment fuxes in rainfall-driven soil erosion: Particle size effects. *Water Resour. Res.*, 52:813–821, 2016.

[22] H. A. Einstein and R. B. Banks. Fluid resistance of composite roughness. *Eos Trans. AGU*, 31(04):603–610, 1950.

[23] Marcelo Garcia and Gary Parker. Experiments on the entrainment of sediment into suspension by a dense bottom current. *Journal of Geophysical Research*, 98:4793, 1993.

[24] P. K. Kundu, I. M. Cohen, and Dowling D. R. *Fluid Mechanics*. 5th edition, 2010.

[25] D. A. Nield. Modeling fluid flow in saturated porous media and at interfaces. *Transport phenomena in porous media II*, pages 1–16, 2002.

[26] Hua Tan and Krishna M. Pillai. Finite element implementation of stress-jump and stress-continuity conditions at porous-medium, clear-fluid interface. *Computers and Fluids*, 38(6):1118–1131, 2009.

[27] T. Stocker. *Introduction to Climate Modelling*. 2011.

[28] G. G. Stokes. *Trans. Cambridge Philos. Soc.*, 9(8), 1851.

[29] H. Faxen. *Ark. Mat. Astron. Fys.*, 17(1), 1923.

[30] G. I. Kelbaliyev. Drag coefficients of variously shaped solid particles, drops, and bubbles. *Theoretical Foundations of Chemical Engineering*, 45(3):248–266, 2011.

[31] J. Hadamard. *C. R. Acad. Sci.*, 152:1735–1738, 1911.

[32] Michael C. Sostarecz and Andrew Belmonte. Motion and shape of a viscoelastic drop falling through a viscous fluid. *J. Fluid Mech*, 497:235–252, 2003.

[33] H. A. Stone and L. G. Leal. The effects of surfactants on drop deformation and breakup. *J. Fluid Mech*, 220:161–186, 1990.

[34] A. N. Srdic-Mitrovic, N. A. Mohamed, and H. J. S. Fernando. Gravitational settling of particles through density interfaces. *J. Fluid Mech.*, 381:175–198, 1999.

[35] K. Y. Yick, C. R. Torres, T. Peacock, and R. Stocker. Enhanced drag of a sphere settling in a stratified fluid at small reynolds numbers. *J. Fluid Mech.*, 632:49–68, 2009.

[36] Roberto Camassa, Claudia Falcon, Joyce Lin, and Richard M. McLaughlin. A first-principle predictive theory for a sphere falling through sharply stratified fluid at low reynolds number. *J. Fluid Mech.*, 664:436–465, 2010.

[37] A. M. Ardekani and R. Stocker. Stratlets: Low reynolds number point-force solutions in a stratified fluid. *Phys. Rev. Lett.*, 105:084502, 2010.

[38] M. Bayareh, A. Doostmohammadi, S. Dabiri, and A. M. Ardekani. On the rising motion of a drop in stratified fluids. *Physics of Fluids*, 25:103302, 2013.

[39] D. Martin and F. Blanchette. Simulations of surfactant-laden drops rising in a density-stratified medium. *Phys. Rev. Fluids*, 2(2):023602, 2017.

[40] F. Blanchette and A. M. Shapiro. Drops settling in sharp stratification with and without marangoni effects. *Physics of Fluids*, 24:042104, 2012.

[41] J. C. Prairie, K. Ziervogel, R. Camassa, R. M. McLaughlin, B. L. White, C. Dewald, and C. Arnosti. Delayed settling of marine snow at sharp density transitions driven by fluid entrainment and diffusion-limited retention. *Mar. Ecol. Prog. Ser.*, 487:185–200, 2013.

[42] J. C. Prairie, K. Ziervogel, R. Camassa, R. M. McLaughlin, B. L. White, C. Dewald, and C. Arnosti. Delayed settling of marine snow: Effects of density gradient and particle properties and implications for carbon cycling. *Marine Chemistry*, 175:28–38, 2015.

[43] J. C. Prairie and B. L. White. A model for thin layer formation by delayed particle settling at sharp density gradients. *Elsevier*, 133(1):37–46, 2017.

[44] Charles B Miller. Biological oceanograp. 2004.

[45] D. C. Smith, M. Simon, A. L. Alldredge, and F. Azam. Intense hydrolytic enzyme activity on marine aggregates and implications for rapid particle dissolution. *Nature*, 359:139–142, 1992.

[46] Hans-Peter Grossart, Kam W. Tang, Thomas Kirboe, and Helle Ploug. Comparison of cell-specific activity between free-living and attached bacteria using isolates and natural assemblages. *FEMS Microbiol. Lett.*, 266(2):194–200, 2007.

[47] K. Ziervogel and C. Arnosti. Polysaccharide hydrolysis in aggregates and free enzyme activity in aggregate-free seawater from the north-eastern gulf of mexico. *Environ. Microbiol.*, 10(2):289–99, 2008.

[48] A. L. Alldredge and M. W. Silver. Characteristics, dynamics and significance of marine snow. *Elsevier*, 20:41–82, 1988.

[49] A. B. Burd and G. A. Jackson. Particle aggregation. *Annu. Rev. Marine Sci.*, 1:65–90, 2009.

[50] A. L. Alldredge, T. J. Cowles, S. MacIntyre, J. E. B. Rines, P. L. Donaghay, C. F. Greenlaw, D. V. Holliday, M. M. Dekshenieks, J. M. Sullivan, and J. R. V. Zaneveld. Occurrence and mechanics of formation of a dramatic thin layer of marine snow in a shallow pacific fjord. *Mar. Ecol. Prog. Ser.*, 233:1–12, 2002.

[51] S. MacIntyre, A.L. Alldredge, and C. C. Gotschalk. Accumulation of marine snow at density discontinuities in the water column. *Limnol. Oceanogr.*, 40:449–468, 1995.

[52] P. Agnot, C. Bruneau, and P. Farbie. A penalization method to take into account obstacles in incompressible viscous flows. *Numer. Math.*, 81:497–520, 1999.

[53] H. Darcy. Les fontaines publiques de la ville de dijon. *Dalmont*, 1856.

[54] D.L. Brown, R. Cortez, and M.L. Minion. Accurate projection methods for the incompressible Navier-Stokes equations. *J. Comp. Phys.*, 168:464–499, 2001.

[55] STÉPHANE Popinet and STÉPHANE Zaleski. A front-tracking algorithm for accurate representation of surface tension. *International Journal for Numerical Methods in Fluids*, 30(6):775–793, 1999.

[56] Bruno Lafaurie, Carlo Nardone, Ruben Scardovelli, Stéphane Zaleski, and Gianluigi Zanetti. Modelling Merging and Fragmentation in Multiphase Flows with Surfer, 1994.

[57] François Blanchette and Terry P. Bigioni. Partial coalescence of drops at liquid interfaces. *Nature Physics*, 2(4):254–257, 2006.

[58] Jacob H. Masliyah and M. Polikar. Terminal velocity of porous spheres. *Physics of Fluids*, 58(3):299–302, 1980.

[59] S. Bhattacharyyaa, S. Dhinakarana, and A. Khalili. Fluid motion around and through a porous cylinder. *Physics of Fluids*, 61(13):4451–4461, 2006.

[60] M. Panah, F. Blanchette, and S. Khatri. Supplemental video 1, Parameters used are Re = 4, Pe = 1746, $\xi = 1.8$, $\gamma = 11.6$, and Da = 5×10^{-4}., 2017.

[61] M. Panah, F. Blanchette, and S. Khatri. Supplemental video 2, Parameters used are Re = 4, Pe = 109, $\xi = 1.8$, $\gamma = 11.6$, and Da = 5×10^{-4}., 2017.

[62] M. Panah, F. Blanchette, and S. Khatri. Supplemental video 3, Parameters used are Re = 4, Pe = 6984, $\xi = 1.8$, $\gamma = 11.6$, and Da = 5×10^{-4}., 2017.

[63] P Blondeaux and G Vittori. Vorticity Dynamics In An Oscillatory Flow Over A Rippled Bed. *Journal of Fluid Mechanics*, 226:257–289, 1991.

[64] John E. Simpson. Gravity currents in the environment and the laboratory, 1997.

[65] Hyoung G. Choi and Daniel D. Joseph. Fluidization by lift of 300 circular particles in plane Poiseuille flow by direct numerical simulation. *Journal of Fluid Mechanics*, 438:101–128, 2001.

[66] Margot G. Gerritsen and Louis J. Durlofsky. Modeling Fluid Flow in Oil Reservoirs. *Annual Review of Fluid Mechanics*, 37(1):211–238, 2005.

[67] Ivan Martin, David Wendt, and Michael Heberer. The role of bioreactors in tissue engineering, 2004.

[68] Goldhaber S. Colman R., Marder V., Clowes A., George J. *Hemostasis and thrombosis: basic principles and clinical practice*. Lippincott Williams & Wilkins, 2006.

[69] James J. Hathcock. Flow effects on coagulation and thrombosis, 2006.

[70] N Korin, M Kanapathipillai, B D Matthews, M Crescente, A Brill, T Mammoto, K Ghosh, S Jurek, S A Bencherif, D Bhatta, A U Coskun, C L Feldman, D D Wagner, and D E Ingber. Shear-activated nanotherapeutics for drug targeting to obstructed blood vessels. *Science*, 337(6095):738–742, 2012.

[71] René P. Schwarzenbach, Thomas Egli, Thomas B. Hofstetter, Urs von Gunten, and Bernhard Wehrli. Global Water Pollution and Human Health. *Annual Review of Environment and Resources*, 35(1):109–136, 2010.

[72] Rony Wallach and Rina Shabtai. Modelling surface runoff contamination by soil chemicals under transient water infiltration. *Journal of Hydrology*, 132(1-4):263–281, 1992.

[73] Gordon S. Beavers and Daniel D. Joseph. Boundary conditions at a naturally permeable wall. *Journal of Fluid Mechanics*, 30(01):197, 1967.

[74] Graham Neale and Walter Nader. Practical significance of brinkman's extension of darcy's law: Coupled parallel flows within a channel and a bounding porous medium. *The Candadian Journal of Chemical Engineering*, 52(4):475–478, 1974.

[75] A. G. Salinger, R. Aris, and J. J. Derby. Finite element formulations for large-scale, coupled flows in adjacent porous and open fluid domains. *International Journal for Numerical Methods in Fluids*, 18(12):1185–1209, 1994.

[76] D. K. Gartling, C. E. Hickox, and R. C. Givler. Simulation of Coupled Viscous and Porous Flow Problems. *International Journal of Computational Fluid Dynamics*, 7(1-2):23–48, 1996.

[77] V. a. F. Costa, L. a. Oliveira, B. R. Baliga, and a. C. M. Sousa. Simulation of Coupled Flows in Adjacent Porous and Open Domains Using Acontrol-Volume Finite-Element Method. *Numerical Heat Transfer, Part A: Applications*, 45(7):675–697, 2004.

[78] K. Vafai and S. J. Kim. Fluid mechanics of the interface region between a porous medium and a fluid layer-an exact solution. *International Journal of Heat and Fluid Flow*, 11(3):254–256, 1990.

[79] J.Alberto Ochoa-Tapia and Stephen Whitaker. Momentum transfer at the boundary between a porous medium and a homogeneous fluid I . Theoretical development. *International Journal of Heat and Mass Transfer*, 38(14):2635–2646, 1995.

[80] V. A. F. Costa, L. A. Oliveira, and B. R. Baliga. Implementation of the Stress Jump Condition in a Control-Volume Finite-Element Method for the Simulation of Laminar Coupled Flows in Adjacent Open and Porous Domains. *Numerical Heat Transfer, Part B: Fundamentals*, 53(5):383–411, 2008.

[81] Wook Ryol Hwang and Suresh G. Advani. Numerical simulations of Stokes-Brinkman equations for permeability prediction of dual scale fibrous porous media. *Physics of Fluids*, 22(11), 2010.

[82] Renato A. Silva & Marcelo J. S. de Lemos. Numerical analysis of the stress jump interface conditions for laminar flow over a porous layer. *Numerical Heat Transfer, Part A: Applications*, 43(6):603–617, 2003.

[83] TswenChyuan Jue. Numerical analysis of vortex shedding behind a porous square cylinder. *International Journal of Numerical Methods for Heat & Fluid Flow*, 14(5):649–663, 2004.

[84] Mouaouia Firdaouss Jean-François Mercier, Catherine Weisman and Patrick Le Quéré. Heat Transfer Associated to Natural Convection Flow in a Partly Porous Cavity. *Journal of Heat Transfer*, 124(1):130–143, 2001.

[85] Y Zeng, H. T. Low, P Yu, and T. S. Lee. A numerical method for flows in porous and homogenous fluid domains coupled at the interface by stress jump. *International Journal for Numerical Methods in Fluids*, 53:1755–1775, 2007.

[86] B. Goyeau, D. Lhuillier, D. Gobin, and M. G. Velarde. Momentum transport at a fluid-porous interface. *International Journal of Heat and Mass Transfer*, 46(21):4071–4081, 2003.

[87] G. Lauriat S. Turki. Examination of two numerical procedures for natural convection in composite enclosures. *Heat Transfer Conf. ASME-HTD*, 130:107–113, 1990.

[88] Reza Masoodi, Hua Tan, and Krishna M. Pillai. Darcy's law-based numerical simulation for modeling 3D liquid absorption into porous wicks. *AIChE Journal*, 57(5):1132–1143, 2011.

[89] Charles S Peskin. The immersed boundary method. *Acta Numerica*, 11:479–517, 2003.

[90] N. A. Patankar, T. Ko, H. G. Choi, and D. D. Joseph. A correlation for the lift-off of many particles in plane Poiseuille flows of Newtonian fluids. *Journal of Fluid Mechanics*, 445:55–76, 2001.

[91] Laura M. McDowellBoyer, James R. Hunt, and Nicholas Sitar. Particle transport through porous media. *Water Resources Research*, 22(13):1901–1921, 1986.

[92] Yousef Saad. Parallel iterative methods for sparse linear systems. *Studies in Computational Mathematics*, 8(C):423–440, 2001.

[93] H. A. van der Vorst. Bi-CGSTAB: A Fast and Smoothly Converging Variant of Bi-CG for the Solution of Nonsymmetric Linear Systems. *SIAM Journal on Scientific and Statistical Computing*, 13(2):631–644, 1992.

[94] J. Happel and H. Brenner. *Low Reynolds number hydrodynamics*. 1983.

[95] S. Bhattacharyya, S. Dhinakaran, and A. Khalili. Fluid motion around and through a porous cylinder. *Chemical Engineering Science*, 61(13):4451–4461, 2006.

[96] Y Saad. *Iterative Methods for Sparse Linear Systems*. 2003.

[97] Y. Saad and M. H. Schultz. Gmres: A generalized minimal residual algorithm for solving nonsymmetric linear systems. *J. Sci. Stat. Comput.*, 7:856–869, 1986.

[98] Leo C. van Rijn. Sediment Transport, Part I: Bed Load Transport. *Journal of Hydraulic Engineering*, 110(10):1431–1456, 1984.

[99] F. Blanchette, M. Strauss, E. Meiburg, B. Kneller, and M. E. Glinsky. High-resolution numerical simulations of resuspending gravity currents: Conditions for self-sustainment. *Journal of Geophysical Research: Oceans*, 110(12):1–15, 2005.

[100] A. R. Gupte H. Rumpf. The influence of porosity and grain size distribution on the permeability equation of porous flow. *Chemie Ing. Techn. (Weinheim)*, 43(6):367–375, 1975.

[101] W. Brian Dade and Peter F. Friend. Grain Size, Sediment Transport Regime, and Channel Slope in Alluvial Rivers. *The Journal of Geology*, 106(6):661–676, 1998.

[102] William E. Dietrich. Settling velocity of natural particles. *Water Resources Research*, 18(6):1615–1626, 1982.

[103] K. Udo and A. Mano. Application of rouse's sediment concentration profile to aeolian transport: Is the suspension system for sand transport in air the same as that in water? *J. Coastal. Res.*, SI 64:2079–2083, 2011.

[104] E. Guazzelli and J. Hinch. Fluctuations and instability in sedimentation. *Annual Review of Fluid Mechanics*, 43:97–116, 2011.

[105] A. Doostmohammadi and A. M. Ardekani. Suspension of solid particles in a density stratified fluid. *PHYSICS OF FLUIDS*, 27:97–116, 2015.

[106] J. W. M. Bush, B. A. Thurber, and F. Blanchette. Particle clouds in homogeneous and stratified environments. *JOURNAL OF FLUID MECHANICS*, 489:29–54, 2003.

[107] A. C. H. Lai, R. Q. Wang, A. W. K. Law, and E. E. Adams.

[108] R. A. Antonia and R. E. Luxton. The response of a turbulent boundary layer to a step change in surface roughness Part 1. Smooth to rough. *Journal of Fluid Mechanics*, 48(04):721–761, 1971.